

Quantum noise in nonlinear nanoscale systems out of equilibrium

Dissertation
zur Erlangung des Doktorgrades
des Fachbereichs Physik
der Universität Hamburg

vorgelegt von
M.Sc. Vicente Ancelmo Leyton Ortega
aus Cali, Colombia

Dezember 2012

Gutachter der Dissertation:	Prof. Dr. M. Thorwart Prof. Dr. A. Lichtenstein
Gutachter der Disputation:	Prof. Dr. M. Thorwart Prof. Dr. M. Potthoff
Datum der Disputation:	20.12.2012
Vorsitzender des Prüfungsausschusses:	PD Dr. A. Chudnovskiy
Vorsitzender des Promotionsausschusses:	Prof. Dr. P. Hauschildt
Leiterin des Fachbereichs Physik:	Prof. Dr. D. Pfannkuche
Dekan der MIN-Fakultt:	Prof. Dr. H. Graener

Contents

1	Introduction	2
2	Dissipation and noise in driven quantum systems	6
2.1	Dissipation in quantum physics	7
2.1.1	The classical Langevin equation	7
2.1.2	The quantum model for loss mechanisms	8
2.1.3	The influence functional and the Born-Markov master equation	12
2.1.3.1	Quantum master equation	14
2.1.4	Master equation in the Lindblad form for harmonically driven systems	15
2.1.4.1	Floquet formalism	16
2.1.4.2	Master equation projected onto Floquet modes	17
2.1.4.3	Rotating wave approximation	18
2.1.4.4	Transient and steady state	19
2.2	Quantum noise	20
2.2.1	Noise in nonequilibrium states	21
2.2.2	The regression theorem in a non-stationary state	22
3	Noise properties of the quantum Duffing oscillator	24
3.1	Coherent dynamics	27
3.1.1	Induced multiphoton Rabi oscillations in the Duffing oscillator	27
3.2	Stationary dissipative dynamics in the deep quantum regime	30
3.2.1	The stationary distribution	30
3.2.2	The nonlinear response of the oscillator	32
3.3	Photon noise in the deep quantum regime	33
3.3.1	Noise spectrum in the underdamped regime	34
3.3.2	Photon antibunching	36

3.3.3	Lineshape of the noise spectrum close to a multiphoton resonance . . .	37
3.3.4	Photon noise at zero frequency	38
3.3.5	Noise spectrum towards the semiclassical regime	40
3.3.6	Dependence of the noise spectrum on damping and temperature . . .	43
3.4	Conclusions	45
4	Qubit state detection using the quantum Duffing oscillator	47
4.1	Persistent current qubit	49
4.2	Driven SQUID as a nonlinear quantum detector	50
4.2.1	Qubit-detector interaction	50
4.2.2	SQUID modelled as a Duffing oscillator	51
4.3	Coherent dynamics and rotating-wave approximation	52
4.4	Detection in the few photon regime	53
4.5	Dissipative dynamics	53
4.5.1	Detector response for weak coupling to the qubit	54
4.6	Backaction in the qubit	56
4.7	Efficiency of the measurement	59
4.8	Conclusions	60
5	Nonequilibrium quantum transport in nanoscale systems	62
5.1	Single-electron devices	63
5.2	Electron gases in zero and one dimension	63
5.3	Hamiltonian model	64
5.4	Real-time transport theory	67
5.4.1	Calculation of the self energy Σ to first order in Γ	69
5.4.2	Extension to the harmonically driven case	70
5.4.3	Current	73
5.5	Driven transport through a single level quantum dot	75
6	Signatures of nonlinearity in driven nanomechanical quantum transport	78
6.1	Hamiltonian model	80
6.1.1	Magneto-elastic coupling	82
6.1.2	Polaron coupling	83
6.2	Current driving the mechanical motion	86
6.2.1	Nonlinear signatures in the current characteristics	88
6.3	Conclusions	89
7	Summary	91

A	Second-order coherence function	93
B	Density matrix of the steady state around resonance	95
C	Semiclassical approximation in the Duffing oscillator dynamics	97
D	Lowest-order expansion in self energies	100
	D.1 Explicit calculation of the rates	102
	Bibliography	103
	Acknowledgements	113

Chapter 1

Introduction

The development of modern quantum mechanics started with the pioneering work on optical spectroscopy of atoms. The pursuit of an explanation for a spectrum composed of discrete lines inspired Bohr to formulate a theory in terms of discrete energy levels of individual atoms. The typical setup for optical spectroscopy comprises the light beams, one shining on an ensemble of identical atoms and another one which probes the spectrum absorbed by the ensemble. The incident light can be absorbed only if its frequency matches the difference of energy between two levels of a single atom. Thus, the position of the absorption lines generated by the whole ensemble was predicted based the properties of an individual atom.[1] In other words, an experiment on the macroscopic scale allowed to indirectly deduce important properties –in this case the energy spectrum– of a quantum system on a microscopic scale not directly accessible in the experiments.

However, addressing an ensemble of identical quantum systems instead of a single quantum system yields certain limitations. For instance, an atom in an excited electronic state will decay to a less excited electronic level (a process named quantum jump). The quantum jump is accompanied by the emission of a photon which can be detected by a photon detector.[2] When the light beam shines on a macroscopic number of atoms, random photon absorption induces excitation of many atoms. The subsequent quantum jumps are also random processes. However, the overall signal, i.e., the emitted light from a macroscopic number of random transitions, is very smooth without any signature of quantum jump processes. Thus, in order to observe quantum jumps and other interesting quantum effects, one should be able to address individual atoms. Alternatively one can design experiments which probe a single macroscopic quantum variable, i. e., a single quantum coherent degree of freedom of a many-body system.

One of the greatest achievements of the last decades has been the access to single atomic systems or a single macroscopic quantum variable, starting in the 1970s with traps for single

neutral atoms[3] and ions.[4] Additionally, in present days, fascinating progress has been made downsizing artificially made condensed-matter devices like nano-electromechanical systems[5–8] and quantum electrodynamics circuits[9] among others macroscopic devices, which start revealing quantum mechanical properties. On the other hand, the observation of quantum processes is not limited to the isolation and confinement of single atomic systems. Various quantum phenomena, such as macroscopic quantum tunneling and resonant tunneling have been observed in capacitance Josephson-junction circuits, where the relevant degrees of freedom studied were the phase difference of the superconducting order parameter across a junction or the flux in a superconducting quantum interference device (SQUID) ring geometry,[9] one of the most interesting application of these devices implementing quantum bits.[9, 10]

Accessing single quantum systems allows to address very fundamental issues like quantum measurement processes and entangled states.[11] Moreover, there are several important applications ranging from sensitive detectors[12] to quantum information processing.[11] In particular, one can describe the measurement process as a “*wave function collapse*”, i.e., as a non-unitary projection which reduces the quantum state of the system to one of the possible eigenstates of the observed quantity with state-dependent probabilities. However, in reality any measurement is performed by a device, suitably coupled to the measured quantum system via a macroscopic readout variable. Its presence, in general, disturbs any possible quantum manipulations performed on the system.[9] Therefore the dissipative processes which accompany the measurement should be switched on only when needed. Sometimes, it is more convenient to amplify the state of the quantum system before its detection, in order to control the induced measurement noise. In that scheme, the measured quantum system is coupled with the amplifier by conducting channels (channels of exchange of information). Depending on the dynamics of the amplifier the noise induced into the measured system can be optimized.

Driving the amplifier out of its equilibrium state, e.g., by applying an external harmonic modulation, allows to optimize the measurement process,[13] since the energy scale is detuned by the external modulation and so are its noise properties. This yields very rich physics, where the time reversal symmetry is broken and the detailed balance principle is not valid.[14] In other words, an elementary process in the driven system is in general not equilibrated by its reverse process. Thereby, it is possible to tune the asymmetry in frequency of the noise in the quantum amplifier.[15] This asymmetry, a feature in quantum systems due to the uncertainty principle, measures the ability of the amplifier to absorb or emit energy from or into the measured system.[13, 15, 16]

Usually, the quantum system is coupled parametrically to the amplifier, thus one can infer on the state of the quantum system through a classical measurement of the parameters of

the amplifier. In general, nonlinear oscillators are naturally used as basic elements for quantum state amplifications. Examples of those are the Josephson bifurcation amplifier [17–22] and the cavity bifurcation amplifier [17, 23]. In addition, the amplifier can operate simultaneously at high frequencies and at low temperatures, entering the regime where $\hbar\omega > k_B T$, with ω being the proper frequency of the oscillator and T its temperature. As such, quantum zero-point fluctuations will play a more dominant role in determining their behaviour than the more familiar thermal fluctuations. Taking into account the relation between quantum noise and quantum measurement one is forced to think about the noise properties of driven nonlinear resonators, and their behaviour as quantum amplifiers in the deep quantum regime.

Given the above, we will focus in the first part of this Thesis on the noise properties of modulated nonlinear resonators in the deep quantum regime. As the simplest example, we consider a monostable anharmonic oscillator which has a quartic nonlinearity (the well known Duffing oscillator). The second scope of this Thesis is to consider such a device as a quantum amplifier of the state of a qubit. In this setup, we introduce a combination of both strategies in measurement theory, bifurcation and dispersion, and propose a nonlinear detector scheme.

Another important issue in fundamental physics related to quantum measurement processes are quantum jumps being observed in single atomic systems or a single macroscopic quantum variable. One of the techniques to reveal this quantum behaviour so far address the linear response in form of the amplitude of the transverse vibrations in a nanobeam doubly clamped to conducting leads. The goal is to excite only a few energy quanta in a resonator held at low temperature. To measure the response, the ultimate goal of the experiments is to increase the resolution of the position measurement to the quantum limit [24–27]. As the response of a damped linear quantum oscillator has the same simple Lorentzian shape as its classical counterpart [28] a unique identification of the “quantumness” of a nanoresonator in the linear regime can sometimes be difficult.

Since transport setups in experimental physics have the advantage that the current-voltage characteristics are rather easily accessible, it is an interesting question to search for nonlinear molecular features there. Therefore as the final scope of this Thesis, we address to the problem of detecting quantum effects, such as quantum jumps, through current-voltage characteristics. To do so, we consider the doubly clamped nanobeam in its nonlinear regime. With an ac bias voltage applied to the leads, the current mimics the harmonic driving in the nonlinear deflection of the nanobeam.

Outlook

In order to study the quantum and thermal noise properties of driven quantum nonlinear resonators, we introduce in Chapter 2 the theory of quantum dissipation based on the system-bath-model with special regard to nonequilibrium states. The regime of weak system-bath coupling and weak external modulation are investigated. Invoking the Born-Markov and the rotating wave approximations, the dissipative dynamics of the driven system is governed by the Lindblad master equation. In the second part of this chapter, using the formal solution of the master equation we show how to compute correlation functions by applying the regression theorem.

We study the power spectrum of the photon number fluctuations in the quantum Duffing oscillator in Chapter 3, starting with a review on the coherent dynamics of the quantum Duffing oscillator, and concluding with the analysis of different characteristics of the photon noise, including the second order of coherence function.

In Chapter 4, a measurement scheme is proposed. We introduce an experimental implementation based on a flux qubit inductively coupled to a driven SQUID. Introducing the equivalence of the driven SQUID to the Duffing oscillator, and the qubit-SQUID coupling term, an analysis based on the optimal point of work is presented, guaranteeing the validity of the approximations. Different characteristics of the amplification process are calculated and discussed, such as the discrimination power of the detector, the back-action on the dynamics of the quantum two level system, and the efficiency of the measurement.

For the final scope of the Thesis, we introduce in Chapter 5 the theory of nonequilibrium quantum transport in nanoscale systems. Introducing zero- and one-dimensional electron gases, we present a general Hamiltonian model involving time-dependent bias voltages applied to the conducting leads. We present a general quantum transport theory based on a real-time diagrammatic approach. Invoking the high-frequency approximation, a master equation is presented with time-independent transition rates (self-energies). The extension to the harmonically driven case is presented with the definition of the Feynman rules for the self-energies. As an example, the special case of a quantum dot with one single-particle state is presented at the end of the Chapter.

In Chapter 6, we study nonlinear signatures of the deflections of a nanobeam in the current characteristics. We introduce the induced electron-phonon coupling by the application of an electric and a magnetic field. For the sake of simplicity, we consider only the influence of the magnetic field. In the regime of the rotating-wave approximation, the amplitude of the alternating current and the amplitude of the nonlinear response of the deflections in the nanobeam are calculated and discussed.

We summarize in Chapter 7 the main results.

Chapter 2

Dissipation and noise in driven quantum systems

One of the most challenging questions faced by the founding fathers of quantum mechanics concerns the emergence of a macroscopic classical reality from a microscopic quantum world. A closely related problem is a self-consistent description of a quantum measurement which does not rely on a classical characterization of the measurement apparatus, see also Chapter 4. A milestone route of a full understanding of these phenomena is the modern theory of dissipative dynamics in open quantum systems. In this framework, dissipation and decoherence are a natural consequence of the coupling of the quantum system of interest to a noisy environment which consists of an ensemble of many quantum degrees of freedom.

In the first section, we give a brief introduction with special regard to systems out of equilibrium. In addition, in the second section, we introduce the regression theorem to calculate the induced fluctuations in the system by its contact with the environment. As a first step, we shall describe the phenomenological model for damping introduced in classical mechanics and its description in the quantum regime. Using the Floquet formalism we present the master equation for a periodically driven state. In the regime of a weak modulation amplitude, we show how the Floquet master equation reduces to the standard Lindblad master equation. Finally, using the formal solution of the master equation we show how to compute the induced fluctuations in the system by applying the regression theorem.

2.1 Dissipation in quantum physics

2.1.1 The classical Langevin equation

In a classical framework, one may often describe dissipation by assuming a homogeneous environment surrounding the system of interest (central system). The homogeneity implies that the dynamics does not depend on the relative position of the system in the environment. Therefore, only a velocity proportional term (viscous force) is introduced in its equation of motion to model damping effects. For instance, in a damped harmonic oscillator – like in Fig. 2.1(a), a spring-mass system in a viscous medium – the equation of motion for its position x including the aforementioned dissipative term characterized by the constant γ , is given by

$$\ddot{x} + \gamma\dot{x} + \omega_0^2 x = 0 , \quad (2.1)$$

where ω_0 is the proper frequency of the oscillator (linear resonator).

In his experiments with pollen grains in water,[29] the botanist Robert Brown observed that a viscous force is not sufficient to model the dissipative dynamics of the pollen grains. In fact, a pollen jiggles about its position. The jiggling motion (called Brownian motion) was later attributed to random collisions of the pollen grains with smaller particles (which constitute the noisy environment).[30, 31] The Brownian motion can be described by including a fluctuating force $\xi(t)$ on the right-hand-side of Eq. (2.1). Thus, one arrives at the so-called Langevin equation which not only describes the damped average motion but also the fluctuations around it.[31] In many cases of practical interest, the random force can be assumed to satisfy the two conditions, that i) the process $\xi(t)$ is a Gaussian process and is therefore fully characterized by the mean and the variance, and ii) its correlation time is infinitely short (δ -correlated), namely

$$\langle \xi(t) \rangle = 0, \quad \langle \xi(t)\xi(t') \rangle \equiv 2\pi C_\xi \delta(t - t'), \quad (2.2)$$

where C_ξ is a constant. The above delta correlated function describes a memoryless environment.

Sometimes, the environment is a source of noise with a finite memory time. Then, the dynamics must be described by a generalized Langevin equation with a time-dependent damping kernel, $\gamma \rightarrow \gamma(t)$

$$\ddot{x} + \int_{-\infty}^t dt' \gamma(t-t') \dot{x}(t') + \omega_0^2 x = \xi(t) . \quad (2.3)$$

The lower limit in the integral describes the uncoupled system-bath configuration in the infinity distant past.

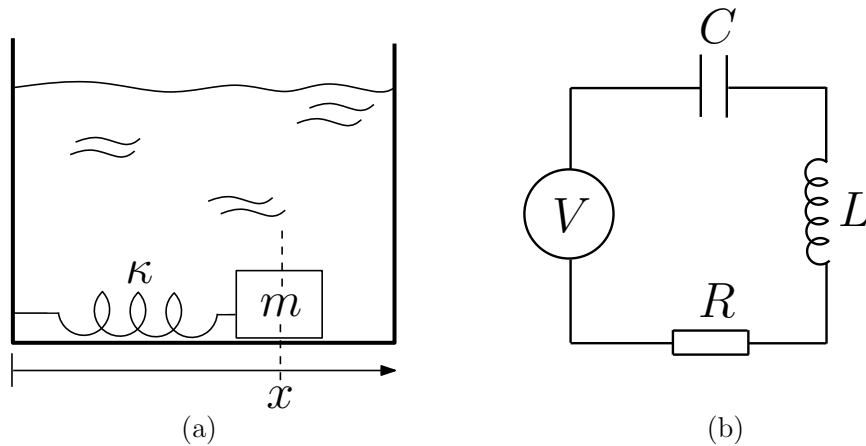


Figure 2.1: (a) Horizontal spring-mass system in a viscous medium. Here the proper frequency is given by $\omega_0 = \sqrt{\kappa/m}$, with m being the mass at the end of the spring, and κ the spring constant. (b) Circuit consisting of a resistor (R), an inductor (L), and a capacitor (C), connected in series – RLC series circuit. Both systems are modelled by the Eq.(2.1).

Since the random and the viscous forces are two different manifestations of the same interaction with the environment (the random collisions with water molecules in the case of the Brownian motion of pollen grains), their intensities are not independent. More specifically, the Fourier-Laplace transform of $\gamma(t)$ is connected with the correlation function $\langle \xi(t)\xi(t') \rangle$ by the classical fluctuation-dissipation theorem[28]

$$m\gamma(\omega) = \frac{1}{k_{\text{B}}T} \int_0^{\infty} d\tau \langle \xi(\tau)\xi(0) \rangle \exp[-i\omega\tau] , \quad (2.4)$$

$$\text{which implies } \langle \xi(\omega)\xi(\omega') \rangle = \frac{k_{\text{B}}T}{\pi} m\gamma(\omega)\delta(\omega + \omega') .$$

A well known example of damped oscillator with such equation describes also a RLC circuit. There, the charge q plays the role of the position, the oscillator eigenfrequency is $\omega_0 = (LC)^{-1}$, and the damping is $\gamma = R/L$ [cf. Fig.2.1(b)]. There, thermal fluctuations in the resistor induce noise into the resonator. Therefore, one should not only consider a resistance but also a noise generator, as the fluctuating force $\xi(t)$ in the mechanical analogue. These thermal fluctuations are connected with damping by Eq. (2.4), and this is known as the Nyquist theorem in resistor circuits.

2.1.2 The quantum model for loss mechanisms

The Hamiltonian for a generic linear quantum oscillator reads as

$$H = \frac{1}{2m}p^2 + \frac{m\omega_0^2}{2}x^2 ,$$

with p and x as the momentum and position operators, respectively. Usually in order to avoid to directly solve the Schrödinger equation in the coordinate representation for the wave function $\phi(x)$ in the energy state E , $(-\hbar^2/2m)\partial_x^2 + (m\omega_0^2/2)x^2\phi(x) = E\phi(x)$, one can introduce the ladder operators a and a^\dagger defined as

$$a = \sqrt{\frac{m\omega_0}{2\hbar}} \left(x + i\frac{p}{m\omega_0} \right), \quad (2.5)$$

$$a^\dagger = \sqrt{\frac{m\omega_0}{2\hbar}} \left(x - i\frac{p}{m\omega_0} \right), \quad (2.6)$$

where their commutator $[a, a^\dagger] = 1$ is fixed by the Heisenberg indetermination principle.

For a conservative system, the Heisenberg equation of motion for the operators, $d\mathcal{O}/dt = (i/\hbar)[H, \mathcal{O}]$ with \mathcal{O} as an operator, are formally equivalent to the Hamilton equation. For the ladder operators we have $a^\dagger(t) = a^\dagger \exp[i\omega_0 t]$ and $a(t) = a \exp[-i\omega_0 t]$.

A naive attempt to incorporate the environmental influence at the quantum level could be to include the damping directly in the Heisenberg equation of motion in the spirit of the correspondence principle. The operators would then have the damped solutions

$$a^\dagger(t) = a^\dagger \exp[i\omega_0 t - \gamma t/2], \quad a(t) = a \exp[-(i\omega_0 t + \gamma t/2)], \quad (2.7)$$

Then, the commutators for equal time would decay according to $[a(t), a^\dagger(t)] = \exp[-\gamma t]$ in violation of the Heisenberg principle.

As it happens in the analogous classical model for damping [cf. Eq. (2.1)], the drawback of this naive approach lies in the fact that it does not incorporate the influence of external fluctuating fields. In the classical case, this is not necessary at very low temperatures when thermal fluctuations vanish according to the classical fluctuation dissipation theorem. On the other hand, in the quantum regime, zero-point fluctuations are present even at the absolute zero. These fluctuations are responsible for preventing the violation of the uncertainty principle. Therefore it is necessary to incorporate a noise generator in the model, which has sufficient output even at absolute zero to preserve the commutation relation $[a(t), a^\dagger(t)] = 1$. Thus, the ladder operators should have the structure $a^\dagger(t) = a_0^\dagger(t) + \delta a^\dagger(t)$ and $a(t) = a_0(t) + \delta a(t)$, where $\delta a(t)$ represents quantum fluctuations operators, which follow the commutation rule $[\delta a(t), \delta a^\dagger(t')] = 1$. There, $\langle a_0(t) \rangle = \langle a(t) \rangle$, and $\langle a_0^\dagger(t) \rangle = \langle a^\dagger(t) \rangle$. For the determination of the dynamics of the quantum fluctuations operators, we shall consider a microscopic model for the environment.

The most successful and rather general approach, is based on the concept of a reservoir or bath consisting in a large collection of systems with many degrees of freedom.[32–37] The simplest model for a bath corresponds to a collection of harmonic oscillators with

Hamiltonian

$$H_B = \sum_k \hbar \omega_k b_k^\dagger b_k, \quad (2.8)$$

where the b_k and b_k^\dagger satisfy the commutation rule $[b_k, b_{k'}^\dagger] = \delta_{kk'}$. Examples range from the quantized modes of the radiation field (photons), to the quantized modes of elastic vibrations in a solid (phonons). Taking into account the foregoing discussion, we consider a bilinear coupling between the bath and the oscillator. In terms of the corresponding ladder operators it reads

$$H_I = \hbar \sum_k c_k (a^\dagger + a)(b_k^\dagger + b_k). \quad (2.9)$$

The Heisenberg equation of motion for the ladder operator of the k -th oscillator in the bath, is given by

$$\dot{b}_k(t) = -i\omega_k b_k(t) + c_k [a^\dagger(t) + a(t)]. \quad (2.10)$$

The second term on the right-hand-side of the above equation corresponds to the forcing term due to the motion of the resonator displacement.

The solution of Eq. (2.10) reads

$$\begin{aligned} b_k(t) = & b_k e^{-i\omega_k t} + c_k \int_0^t dt' e^{-i(\omega_k - \omega_0)(t-t')} [a(t') e^{i\omega_0(t'-t)}] + \\ & c_k \int_0^t dt' e^{-i(\omega_k + \omega_0)(t-t')} [a^\dagger(t') e^{-i\omega_0(t'-t)}]. \end{aligned} \quad (2.11)$$

Noticing that the terms in square brackets are slowly varying functions of t' , and that the last integral on the right hand side involves a fast oscillating terms ($\propto \exp[i(\omega_k + \omega_0)(t - t')]$) in comparison with the first one that involves slow oscillating terms ($\propto \exp[i(\omega_k - \omega_0)(t - t')]$), we can approximate the above solution as

$$b_k(t) \approx b_k e^{-i\omega_k t} + c_k \int_0^t dt' e^{-i(\omega_k - \omega_0)(t-t')} [a(t') e^{i\omega_0(t'-t)}]. \quad (2.12)$$

On the other hand, the equation of motion for the resonator mode reads

$$\begin{aligned} \dot{a}(t) = & -i\omega_0 a(t) + \sum_k c_k [b_k^\dagger(t) + b_k(t)] \\ \approx & -i\omega_0 a(t) + \sum_k c_k b_k(t) e^{-i\omega_k t} + \\ & \sum_k c_k^2 \int_0^t dt' e^{-i(\omega_k - \omega_0)(t-t')} [a(t') e^{i\omega_0(t'-t)}]. \end{aligned} \quad (2.13)$$

The decay rate of the resonator from the single phonon excited state $n = 1$ to the ground state $n = 0$ would be given by the Fermi Golden Rule expression

$$\gamma(\omega_0) = 2\pi \sum_k c_k^2 \delta(\omega_0 - \omega_k). \quad (2.14)$$

From this we get to a useful relation to solve the integral in Eq. (2.13),

$$\int_{-\infty}^{\infty} \frac{d\omega}{2\pi} \gamma(\omega_0 + \omega) e^{-i\omega(t-t')} = \sum_k c_k^2 e^{-i(\omega_k - \omega_0)(t-t')} . \quad (2.15)$$

In the strict Ohmic case, $\gamma(\omega) = \gamma$, and $\sum_k c_k^2 \exp[-i(\omega_k - \omega_0)(t - t')] = \gamma\delta(t - t')$. With this, the Eq. (2.13) becomes

$$\dot{a}(t) \approx -i\omega_0 a(t) - \gamma a(t)/2 - \eta(t) , \quad (2.16)$$

with $\eta(t) = \sum_k c_k \exp[-i\omega_k t] b_k$. Therefore, the fluctuation operator δa reads

$$\delta a(t) = - \int_0^t dt' \eta(t') \exp[-(i\omega_0 + \gamma/2)(t - t')] . \quad (2.17)$$

Now, we can identify the external fluctuating force $\xi(t)$ with $\xi(t) = \eta^\dagger(t) + \eta(t)$. It has a Gaussian statistics

$$\langle \xi(t) \rangle = 0, \quad \langle \xi(t)\xi(0) \rangle = C_{\xi\xi}(t), \quad (2.18)$$

with second moment $C_{\xi\xi}(t)$ given by

$$C_{\xi\xi}(t) = \sum_k c_k^2 [\bar{n}(\hbar\omega_k) e^{i\omega_k t} + [1 + \bar{n}(\hbar\omega_k)] e^{-i\omega_k t}], \quad (2.19)$$

where $\bar{n}(\hbar\omega_k) = \langle b_k^\dagger b_k \rangle = (\exp[\hbar\omega_k \beta] - 1)^{-1}$ is the boson occupation number, with $\beta = 1/k_B T$ as the inverse temperature.

Introducing the spectral density of the interaction with the bath

$$J(\omega) = \frac{\pi}{\hbar} \sum_k c_k^2 \delta(\omega - \omega_k) , \quad (2.20)$$

which is proportional to the frequency for the Ohmic bath ($J(\omega) \propto \omega$), one can rewrite the above correlation function as

$$C_{\xi\xi}(t) = \frac{\hbar}{\pi} \int_0^\infty d\omega J(\omega) [\bar{n}(\hbar\omega) e^{i\omega t} + [1 + \bar{n}(\hbar\omega)] e^{-i\omega t}] . \quad (2.21)$$

With this the power spectrum of the fluctuation force (the Fourier transform of Eq. (2.21)) reads

$$C_{\xi\xi}[\omega] = \hbar \coth[\beta\hbar\omega/2] J(\omega). \quad (2.22)$$

From Eq.(2.14), one notices that the spectral density also determines the damping of the system; in the Ohmic case by $J(\omega) = m\omega\gamma$. Thus Eq. (2.22) is a version of the quantum-mechanical fluctuation-dissipation theorem. We have considered the bath as a collection of harmonic oscillators, and from the discussion foregoing the bath is only of indirect interest, and its properties need only to be specified in very general terms, e.g., by the temperature and the spectral density.[38]

2.1.3 The influence functional and the Born-Markov master equation

The system-bath model presented in the previous section describes dissipation and a source of quantum noise for the central system. The integration of the equations of motion in the Heisenberg picture appears quite simple, but it is limited to the very rare cases where the equations can be solved directly. For a more general scenario, where the direct integration is not possible, a more convenient strategy consists in tracing out the bath degrees of freedom and studying the dynamics of the reduced density operator ρ , $\rho \equiv \text{Tr}_B[W]$, with W being the full density operator and $\text{Tr}_B[\dots]$ the partial trace over the bath variables.

Since the full knowledge of the whole system state at some specific time is incomplete, we should appeal to a statistical description, where the system is completely characterized by the density operator

$$W(t) = \sum_k p_k |\psi_k(t)\rangle \langle \psi_k(t)|, \quad (2.23)$$

where p_k is the probability of the whole system to be in the state $|\psi_k(t)\rangle$. The time evolution of the density operator is governed by the von-Neumann equation

$$\frac{d}{dt}W(t) = \frac{i}{\hbar}[H(t), W(t)], \quad (2.24)$$

where $H(t) = H_0(t) + H_{\text{SB}} + H_B$, wherein $H_0(t)$ is the Hamiltonian of the central system, H_{SB} the bilinear bath-system interaction, and H_B the bath Hamiltonian. The evolution operator of the system state $\mathcal{U}(t, t_0)$, defined by $|\psi_k(t)\rangle = \mathcal{U}(t, t_0)|\psi_k(t_0)\rangle$, follows the same equation, i.e., $\partial_t \mathcal{U}(t) = i[H(t), \mathcal{U}(t)]/\hbar$.

We have to perform now the trace over the degrees of freedom of the bath in order to study the dynamics of the system. To this end, the path-integral formulation of quantum mechanics has proved to be more convenient than the operator notation.[39] We start with the integration of the von Neumann equation (2.24),

$$W(t) = \mathcal{U}(t, t_0) W(t_0) \mathcal{U}^{-1}(t, t_0), \quad (2.25)$$

where $\mathcal{U}(t, t_0) = \mathcal{T} \exp[-i \int_{t_0}^t ds H(s)/\hbar]$ is the time evolution operator, with \mathcal{T} being the time-ordering operator. In the position representation, the solution Eq. (2.25) reads

$$\begin{aligned} W(X_f, X'_f; t) &\equiv \langle X_f | W(t) | X'_f \rangle \\ &= \int dX_0 dX'_0 \mathcal{U}(X_f, t; X_0, t_0) W(X_0, X'_0, t_0) \mathcal{U}^*(X'_f, t; X'_0, t_0), \end{aligned} \quad (2.26)$$

where we have used the shorthand notation $X = \{x, \bar{x}_1, \bar{x}_2, \dots, \bar{x}_N\}$ for the resonator coordinates x and for the bath oscillator coordinates $\bar{x}_1, \bar{x}_2, \dots, \bar{x}_N$. Here we have considered N

a finite and large number of subsystems in the bath. Furthermore, hereafter the indefinite integral over coordinates variables denotes implicitly the integration over all the space, i.e. $\int_{-\infty}^{+\infty}$.

In Eq. (2.26) the evolution operator (propagator) in the path-integral formulation is given by[39]

$$\mathcal{U}(X_f, t; X_0, t_0) = \int_{X(t_0)=X_0}^{X(t)=X_f} \mathcal{D}X(s) \exp [i(S[x] + S_B[X])/\hbar] , \quad (2.27)$$

which represents the sum over all possible paths $X(s)$ in coordinate space from X_0 to X_f of the functional $\exp [i(S[x] + S_B[X])/\hbar]$, where $S[x] = \int_{t_0}^t ds L(\dot{x}, x, s)$ and $S_B[X] = \int_{t_0}^t ds L_B(\dot{X}, X, s)$ are the classical actions calculated from the Lagrangians $L(\dot{x}, x, s)$ and $L_B(\dot{X}, X, s)$, corresponding to the central system and the bath plus system-bath coupling respectively, along the trajectory $X(s)$.

We assume as the initial preparation of the whole system, at $t = t_0$, that the bath is not correlated with the system and it is canonically distributed with respect to the free bath Hamiltonian, i.e., the initial preparation of the density operator W reads as

$$W(t_0) = \rho(t_0) \otimes \rho_B , \text{ with } \rho_B = \frac{\exp[-\beta H_B]}{\text{Tr}_B [\exp[-\beta H_B]]} . \quad (2.28)$$

Plugging this initial preparation into Eq. (2.26) and tracing out the bath variables by integrating over all the bath coordinates $\bar{x}_1, \bar{x}_2, \dots, \bar{x}_N$, we obtain the reduced density operator

$$\begin{aligned} \rho(x_f, x'_f; t) &= \int d\bar{x}_1 d\bar{x}_2 \dots d\bar{x}_N \langle X_f | W(t) | X'_f \rangle \\ &= \int dx_0 dx'_0 \mathcal{G}_{\text{eff}}(x_f, x'_f, t; x_0, x'_0, t_0) \rho(x_0, x'_0; t_0) , \end{aligned} \quad (2.29)$$

where,

$$\begin{aligned} \mathcal{G}_{\text{eff}}(x_f, x'_f, t; x_0, x'_0, t_0) &= \int_{x(t_0)=x_0}^{x(t)=x_f} \mathcal{D}x \int_{x'(t_0)=x'_0}^{x'(t)=x'_f} \mathcal{D}x' \exp [i(S[x] - S[x'])/\hbar] \times \\ &\quad \exp[-\phi_{\text{FV}}[x, x']/\hbar] \end{aligned} \quad (2.30)$$

is the effective propagator for the reduced density operator. In the second line of Eq. (2.29) we have used the completeness property $\int dx |x\rangle \langle x| = \mathbb{I}$ for x_0 and x'_0 , with \mathbb{I} being the identity operator. Furthermore, the last term on the right hand side is the Feynman-Vernon influence functional which represents the influence of the bath. The influence phase

$\phi_{\text{FV}}[x, x']$ is given by[28]

$$\text{Re}\{\phi_{\text{FV}}[x, x']\} = \int_{t_0}^t dt' \int_{t_0}^{t'} dt'' (x(t') - x'(t')) \text{Re}\{C_\xi(t' - t'')\} (x(t'') - x'(t'')) , \quad (2.31)$$

$$\begin{aligned} \text{Im}\{\phi_{\text{FV}}[x, x']\} &= -\frac{m}{2} \int_{t_0}^t dt' \int_{t_0}^{t'} dt'' (x(t') - x'(t')) \gamma(t' - t'') (\dot{x}(t'') + \dot{x}'(t'')) \\ &\quad - \frac{m}{2} \int_{t_0}^t dt' (x(t') - x'(t')) \gamma(t') (x(t_0) + x'(t_0)) . \end{aligned} \quad (2.32)$$

The real part is responsible for the loss of coherence since it provides random pumping of energy back and forth between system and bath. Additionally, the imaginary part brings friction into the system as it provides the damping force $\int_{t_0}^t dt'' \gamma(t - t'') (\dot{x}(t'') + \dot{x}'(t''))$. [28] The last term on the right hand side in the imaginary part gives the initial slip, since it can be added to the stochastic force in the equation of motion for the position $x(t)$, and it is omitted in the following.[28]

2.1.3.1 Quantum master equation

In the weak coupling limit, where the damping constant γ is the smallest frequency scale in the system, $\gamma \ll \{k_{\text{B}}T/\hbar, \omega_0, \omega_{\text{ex}}\}$, we can then expand the influence functional up to first order in its phase, which is proportional to γ [cf. Eqs. (2.31) and (2.22)]. Thus, $\exp[-\phi_{\text{FV}}[x, x']/\hbar] \approx 1 - \phi_{\text{FV}}[x, x']/\hbar$, [40] and the reduced density operator reads

$$\begin{aligned} \rho(x_f, x'_f; t) &= \int dx_0 dx'_0 \mathcal{G}_0(x_f, x'_f, t; x_0, x'_0, t_0) \rho(x_0, x'_0; t_0) \\ &\quad - \frac{1}{\hbar} \int_{t_0}^t dt' \int_{t_0}^{t'} dt'' \int dx_{t'} dx'_{t'} dx_{t''} dx'_{t''} \\ &\quad \times \mathcal{G}_0(x_f, x'_f, t; x_{t'}, x'_{t'}, t') \cdot (x_{t'} - x'_{t'}) \cdot \mathcal{G}_0(x_{t'}, x'_{t'}, t'; x_{t''}, x'_{t''}, t'') \times \\ &\quad \left[\text{Re}\{C_\xi(t' - t'')\} \cdot (x_{t''} - x'_{t''}) - i \frac{m}{2} \gamma(t' - t'') \cdot (\dot{x}_{t''} - \dot{x}'_{t''}) \right] \rho(x_{t''}, x'_{t''}, t'') , \end{aligned} \quad (2.33)$$

where $\mathcal{G}_0(x_f, x'_f, t; x_0, x'_0, t_0)$ is the free propagator for the central system, given by

$$\mathcal{G}_0(x_f, x'_f, t; x_0, x'_0, t_0) = \mathcal{U}_0(x_f, t; x_0, t_0) \mathcal{U}_0^*(x'_f, t; x'_0, t_0) , \quad (2.34)$$

with

$$\mathcal{U}_0(x_f, t; x_0, t_0) = \int_{x(t_0)=x_0}^{x(t)=x_f} \mathcal{D}x \exp [iS[x]/\hbar] .$$

Above we have assumed that the path integration commutes with the integrals over t' and t'' . Up to zeroth order in γ , we express $\rho(t'')$ in terms of $\rho(t)$ as follows

$$\rho(x_{t''}, x'_{t''}, t'') = \int dx dx' \mathcal{U}_0(x_{t''}, t''; x, t) \mathcal{U}_0^*(x'_{t''}, t''; x', t) \rho(x, x', t). \quad (2.35)$$

Inserting this into Eq.(2.33), and differentiating with respect to t , one can obtain the master equation

$$\begin{aligned} \dot{\rho}(x_f, x'_f, t) &= -i[H_S(x_f, t) - H_S(x'_f, t)]\rho(x_f, x'_f, t) - \frac{1}{\hbar} \int_{t_0}^t d\tau \int dx_{t''} dx'_{t''} dx dx' \times \\ &\quad \mathcal{G}_0(x_f, x'_f, t; x_{t''}, x'_{t''}, t - \tau) \cdot (x_f - x'_f) \cdot \mathcal{G}_0(x_{t''}, x'_{t''}, t - \tau; x, x', t) \times \\ &\quad \left[\text{Re}\{C_\xi(\tau)\} \cdot (x_{t''} - x'_{t''}) - i\frac{m}{2}\gamma(\tau) \cdot (\dot{x}_{t''} - \dot{x}'_{t''}) \right] \rho(x, x', t). \end{aligned} \quad (2.36)$$

Here, we have substituted the integration variable t'' by $\tau = t - t''$. The above master equation describes the evolution of the system state independently on its past (Markovian characteristics), since $\dot{\rho}(t)$ depends only on $\rho(t)$. The master equation (2.36) can be written in a more convenient form as

$$\dot{\rho}(t) = \frac{1}{i\hbar} [H_S(t), \rho(t)] + \mathcal{L}(t)\rho(t), \quad (2.37)$$

where the first term on the right hand side represents the coherent evolution, and the second one the influence of the bath. The latter is given by

$$\mathcal{L}(t)\rho(t) = -\frac{1}{\hbar} [x, (Q(t) + iP(t)/2)\rho(t) - \rho(t)(Q(t) - iP(t)/2)], \quad (2.38)$$

with the correlations functions

$$P(t) = \int_0^\infty d\tau \gamma(\tau) \mathcal{U}_0^*(t - \tau, t) p \mathcal{U}_0(t - \tau, t) \quad \text{and} \quad (2.39)$$

$$Q(t) = \int_0^\infty d\tau \text{Re}\{C_\xi(\tau)\} \mathcal{U}_0^*(t - \tau, t) x \mathcal{U}_0(t - \tau, t). \quad (2.40)$$

Furthermore, we have assumed that the integration kernel $\text{Re}\{C_\xi(t)\}$ and $\gamma(t)$ practically vanish after a finite time $\tau_B = \hbar/k_B T$ and then the upper integration limit in Eqs. (2.39) and (2.40) are extended to infinity, therefore one can implicit consider the elapsed time t from the preparation to be much larger than τ_B .

2.1.4 Master equation in the Lindblad form for harmonically driven systems

So far, we have introduced a method for the study of the dynamics of a system weakly coupled to a dissipative environment in the spirit of the Caidera-Leggett model.[37] Now,

we shall focus on a specific case of time-periodic driven systems, where the evolution of the system is split into a transient and a steady state dynamics. In the former, the system is in an unstable state. From there, the system eventually reaches a balance between pumping and dissipation turning the system into an steady state.

2.1.4.1 Floquet formalism

Differential equations involving operators, like Eq. (2.37), must be projected onto a determined set of states for their solution. The choice of this set of states determines, in some cases, the difficulty of the problem. In a stationary system, we might use the eigenstates of the system Hamiltonian directly, but for harmonically driven systems we can take the advantage of the induced periodicity and use Floquet modes. The Floquet modes are the time-periodic analogy of the Bloch vectors in solid state physics. In the following we introduce the Floquet formalism in quantum systems.

In harmonically driven systems, according with the Floquet theorem, the solution of the Schrödinger equation $|\Psi(t)\rangle$, $(H_S(t) - i\hbar\partial_t)|\Psi(t)\rangle = 0$, can be determined by the ansatz $|\Psi_k(t)\rangle = \exp[-i\varepsilon_k t/\hbar]|\phi_k(t)\rangle$ [see Ref. 41 for a complete review on the Floquet formalism]. Where $|\phi(t)\rangle$ is periodic in time, i.e., it is a Floquet mode obeying: $|\phi(t)\rangle = |\phi(t + 2\pi/\omega_{\text{ex}})\rangle$. Here ε_k is a real parameter, being unique up to multiples of $\hbar\omega_{\text{ex}}$. It is termed the Floquet characteristic exponent or the quasienergy.[42–44] Replacing the aforementioned ansatz into the Schrödinger equation, one obtains the eigenvalue equation for the quasienergy ε_k . With the Hermitian operator $H_{FL} = H_S(t) - i\hbar\partial_t$, so-called Floquet Hamiltonian, one finds that

$$H_{FL}|\phi_k(t)\rangle = \varepsilon_k|\phi_k(t)\rangle. \quad (2.41)$$

The Floquet modes $|\phi_{k'}(t)\rangle = \exp[in\omega_{\text{ex}}t]|\phi_k(t)\rangle \equiv |\phi_{nk}(t)\rangle$, with n being an integer number, yields the identical solution describing the same physical situation, but with a shifted quasienergy $\varepsilon_k \rightarrow \varepsilon_{k'} = \varepsilon_k + n\hbar\omega_{\text{ex}}$. Therefore, the index k corresponds to the whole family of solutions indexed by $k' = (k, n)$, $n \in \mathbb{Z}$. The eigenvalues $\{\varepsilon_k\}$ hence can be mapped into a first Brillouin zone obeying $-\hbar\omega_{\text{ex}} < \varepsilon < \hbar\omega_{\text{ex}}$.

For the Floquet Hermitian operator it is convenient to introduce the composite Hilbert space $\mathbf{R} \otimes \mathbf{T}$ made up of the original Hilbert space \mathbf{R} and space \mathbf{T} of functions which are periodic in time with period $2\pi/\omega_{\text{ex}}$. [45] The temporal part of this new Hilbert space is spanned by the orthonormal set of Fourier vectors $\langle n|t \equiv \exp[-in\omega_{\text{ex}}t]$, $n \in \mathbb{Z}$, and the inner product in \mathbf{T} reads as

$$(m, n) = \frac{\omega_{\text{ex}}}{2\pi} \int_0^{2\pi/\omega_{\text{ex}}} dt \exp[-i(n - m)\omega_{\text{ex}}t] = \delta_{n,m}. \quad (2.42)$$

Thus, the eigenvectors of H_{FL} obey the orthogonality condition in the composite Hilbert space $\mathbf{R} \otimes \mathbf{T}$, i.e. $\langle\langle \phi_{k'}(t)|\phi_{l'}(t)\rangle\rangle = \delta_{k'l'} = \delta_{kl}\delta_{nm}$, and form a complete set in $\mathbf{R} \otimes \mathbf{T}$, i.e.

$\sum_{n\alpha} |\phi_{nk}(t)\rangle\langle\phi_{nk}(t)| = \mathbb{I}_{\mathbf{R}}$ ($\mathbb{I}_{\mathbf{R}}$ is the unitary matrix in the original Hilbert space \mathbf{R}). The Floquet modes of the same Brillouin zone form a complete set in \mathbf{R} , i.e. $\sum_k |\phi_k(t)\rangle\langle\phi_k(t)| = \mathbb{I}_{\mathbf{R}}$.

2.1.4.2 Master equation projected onto Floquet modes

Here, we shall combine the Born-Markov master equation with the Floquet formalism.[46] We start projecting the reduced density operator onto a selected set of Floquet modes, such that $\rho_{kl}(t) = \langle\phi_k(t)|\rho(t)|\phi_l(t)\rangle$, and we describe the evolution of the state by its time derivative

$$\begin{aligned}\dot{\rho}_{kl}(t) &= \langle\phi_k(t)|\frac{1}{i\hbar}[H_S(t), \rho(t)] + \mathcal{L}(t)\rho(t)|\phi_l(t)\rangle + \langle\dot{\phi}_k(t)|\rho(t)|\phi_l(t)\rangle + \langle\phi_k(t)|\rho(t)|\dot{\phi}_l(t)\rangle \\ &= \frac{1}{i\hbar}(\varepsilon_k - \varepsilon_l)\rho_{kl}(t) + \sum_r \langle\phi_k(t)|\mathcal{L}(t)|\phi_r(t)\rangle\rho_{rl}(t).\end{aligned}\quad (2.43)$$

For the calculation of the matrix elements of the dissipative part of the master equation $\langle\phi_k(t)|\mathcal{L}(t)|\phi_r(t)\rangle$, we need to consider the Fourier expansion of the Floquet modes $|\phi_k(t)\rangle = \sum_{n\in\mathbb{Z}} \exp[-in\omega_{\text{ext}}t]|\phi_k^n\rangle$. Thus, the projection of an arbitrary operator \mathcal{O} onto the selected set of Floquet modes, i.e. the matrix elements $\mathcal{O}_{kl}(t) = \langle\phi_k(t)|\mathcal{O}|\phi_l(t)\rangle$ may be written as

$$\mathcal{O}_{kl}(t) = \sum_{n\in\mathbb{Z}} e^{-in\omega_{\text{ext}}t} \mathcal{O}_{kl}^n, \quad \text{with} \quad \mathcal{O}_{kl}^n = \sum_{m\in\mathbb{Z}} \langle\phi_k^m|\mathcal{O}|\phi_l^{m+n}\rangle. \quad (2.44)$$

With this, we can calculate the projection of the correlations Eqs. (2.39) and (2.40). Thus, the matrix elements $P_{kl}(t) = \langle\phi_k(t)|P(t)|\phi_l(t)\rangle$ and $Q_{kl}(t) = \langle\phi_k(t)|Q(t)|\phi_l(t)\rangle$ are given by

$$\begin{aligned}P_{kl}(t) &= \int_0^\infty d\tau \gamma(\tau) \langle\phi_k(t)|\mathcal{U}_0^*(t-\tau, t) p \mathcal{U}_0(t-\tau, t)|\phi_l(t)\rangle \text{ and} \\ &= \int_0^\infty d\tau \gamma(\tau) \exp[-i(\varepsilon_k - \varepsilon_l)\tau/\hbar] \langle\phi_k(t-\tau)|p|\phi_l(t-\tau)\rangle \\ &= \frac{m}{i\hbar}(\varepsilon_k - \varepsilon_l - id/dt) \int_0^\infty d\tau \gamma(\tau) \exp[-i(\varepsilon_k - \varepsilon_l)\tau/\hbar] x_{kl}(t-\tau)\end{aligned}\quad (2.45)$$

$$\begin{aligned}Q_{kl}(t) &= \int_0^\infty d\tau \text{Re}\{C_\xi(\tau)\} \langle\phi_k(t)|\mathcal{U}_0^*(t-\tau, t) x \mathcal{U}_0(t-\tau, t)|\phi_l(t)\rangle \\ &= \int_0^\infty d\tau \text{Re}\{C_\xi(\tau)\} \exp[-i(\varepsilon_k - \varepsilon_l)\tau/\hbar] x_{kl}(t-\tau),\end{aligned}\quad (2.46)$$

where $x_{kl}(t-\tau) = \sum_{n\in\mathbb{Z}} \exp[-in\omega_{\text{ext}}t]x_{kl}^n$. Furthermore, above we have used $\mathcal{U}_0(t-\tau, t) = \sum_k \exp[i\varepsilon_k\tau/\hbar]|\phi_k(t-\tau)\rangle\langle\phi_k(t)|$, and $p/m = -i[H_{FL}, x]/\hbar$. With this, we can determine the matrix elements for $Q(t) \pm iP(t)/2$ [cf. Eq. (2.38)],

$$(Q(t) \pm iP(t)/2)_{kl} = \sum_{n\in\mathbb{Z}} e^{-in\omega_{\text{ext}}t} N_{kl, \mp n} x_{kl}^n, \quad (2.47)$$

where $N_{kl,n}$ are defined as

$$N_{kl,n} = N(\varepsilon_k - \varepsilon_l + n\hbar\omega_{\text{ex}}), \text{ with } N(\varepsilon) = J(|\varepsilon|/\hbar)[\bar{n}(|\varepsilon|) + \Theta(-\varepsilon)]/\hbar, \quad (2.48)$$

in terms of the spectral density $J(\varepsilon/\hbar)$ ($= m\gamma\varepsilon/\hbar$ in the strict Ohmic case), the bosonic thermal occupation number $\bar{n}(\varepsilon) = (\exp[\varepsilon\beta] - 1)^{-1}$, and the Heaviside function $\Theta(x)$.

We have calculated the matrix elements of the dissipative part of the master equation, $\langle \phi_k(t) | \mathcal{L}(t) | \phi_r(t) \rangle$, in terms of Fourier modes x_{kl}^n (which depend on the central system), and bath parameters as temperature T and spectral density $J(\omega)$. Then, the master equation reads[46–48]

$$\begin{aligned} \dot{\rho}_{kl}(t) = & \frac{1}{i\hbar}(\varepsilon_k - \varepsilon_l)\rho_{kl}(t) \sum_{k'l',nn'} \exp[i(n+n')\omega_{\text{ex}}t] \cdot \{ (N_{kk',n} + N_{ll',-n'})x_{kk'}^n \rho_{k'l'}(t) x_{ll',n'} \\ & - N_{l'k',n'} x_{kl'}^n x_{l'k'}^{n'} \rho_{k'l}(t) - N_{k'l',-n'} \rho_{kl}(t) x_{l'k'}^{n'} x_{kl'}^n \} \end{aligned} \quad (2.49)$$

2.1.4.3 Rotating wave approximation

The coefficients of the dissipative part are periodic in time, with frequency $(n+n')\omega_{\text{ex}}$. In the weak coupling regime characterized by $\gamma \ll \omega_0$, and an external driving close to resonance to the central system ($|\omega_0 - \omega_{\text{ex}}| \ll \omega_0$), the dissipative effects are relevant only on a time scale much larger than the period of the driving, due to $\tau_B > 2\pi/\omega_{\text{ex}}$. [46] Therefore one can neglect fast oscillating terms in Eq. (2.49) by averaging over one period of the driving, yielding the following master equation with time-independent dissipative transition rates

$$\dot{\rho}_{kl}(t) = \frac{1}{i\hbar}(\varepsilon_k - \varepsilon_l)\rho_{kl}(t) + \sum_{k'l'} \mathcal{L}_{kl,k'l'} \rho_{k'l'}(t), \quad (2.50)$$

with

$$\begin{aligned} \mathcal{L}_{kl,k'l'} = & \sum_{n \in \mathbb{Z}} [(N_{kk',-n} + N_{ll',-n})x_{kk'}^n x_{ll'}^{-n} \\ & - \delta_{kk'} \sum_{k''} N_{k''l',-n} x_{l'k''}^{-n} x_{k''l}^n \\ & - \delta_{ll'} \sum_{l''} N_{l''k',-n} x_{kl''}^{-n} x_{l''k'}^n]. \end{aligned} \quad (2.51)$$

This approximation was introduced by Ref. 46 under the name of the *moderate rotating wave approximation*. Further approximations can be applied when we consider the regime of weak driving strength. There, we can approximate the Floquet modes by rotated states $|\varphi_k\rangle$, $|\phi_k(t)\rangle \approx R^\dagger(t)|\varphi_k\rangle$, wherein $R(t) = \exp[ia^\dagger a \omega_{\text{ex}} t]$. The rotated states $|\varphi_k\rangle$ are eigenstates of the Hamiltonian in the full rotating wave approximation, where only propagating terms

are considered. We shall apply this approximation in the case of the Duffing oscillator in the next chapter. Using this approximation we can calculate the Fourier modes x_{kl}^n . Since the position operator in the rotated frame has two Fourier modes,

$$x(t) = x_{ZPF}(ae^{-i\omega_{\text{ex}}t} + a^\dagger e^{i\omega_{\text{ex}}t})/\sqrt{2},$$

it is clear that $x_{kl}^1/x_{ZPF} = a_{kl}/\sqrt{2} \equiv \langle \varphi_k | a | \varphi_l \rangle / \sqrt{2}$, $x_{kl}^{-1}/x_{ZPF} = a^* r_{kl}/\sqrt{2} \equiv \langle \varphi_k | a^\dagger | \varphi_l \rangle / \sqrt{2}$, and $x_{kl}^n = 0$ for the remaining values of the integer n . This approximation restricts the sum on the Fourier modes in Eq. (2.51) to $n = \pm 1$. On the other hand, for the Brillouin zone chosen for the set $\{|\phi_k\rangle\}$ the quasienergies follow $|\varepsilon_k - \varepsilon_l| \ll \hbar\omega_{\text{ex}}$, and therefore the dependence of the Planck numbers $N_{kl,n}$ on Floquet modes can be neglected. Thus, $N_{kl,1} \approx J(\omega_{\text{ex}})\bar{n}(\hbar\omega_{\text{ex}})$ and $N_{kl,-1} \approx J(\omega_{\text{ex}})(\bar{n}(\hbar\omega_{\text{ex}}) + 1)$. This means that for $n = 1$ the transition rates (2.51) describe an absorption process of one quantum (photon/phonon) from the bath, whereas $n = -1$ describe an emission process of one quantum into the bath. In the operator notation the dissipative transition rates then turn out as

$$\mathcal{L}\rho(t) = \gamma [\bar{n}(\hbar\omega_{\text{ex}}) + 1]\mathcal{D}[a]\rho(t) + \gamma \bar{n}(\hbar\omega_{\text{ex}})\mathcal{D}[a^\dagger]\rho(t) \quad (2.52)$$

with $\mathcal{D}[\mathcal{O}]$ being the Lindblad superoperator defined as

$$\mathcal{D}[\mathcal{O}]\rho(t) = ([\mathcal{O}\rho(t), \mathcal{O}^\dagger] + [\mathcal{O}, \rho(t)\mathcal{O}^\dagger])/2, \quad (2.53)$$

where \mathcal{O} is an arbitrary operator of the central system. In Eq. (2.52) we have used the definition of the spectral density for the strict Ohmic case, $J(\omega) = m\gamma\omega$.

In the following we shall use this simplified version of the transition rates to solve the master equation. This form has the advantage of conserving the positivity of the density operator. Additionally, it allows a fully analytical treatment to take into account the influence of the thermal bath on the system.

2.1.4.4 Transient and steady state

In the operator notation the master equation Eq.(2.50) is given by $\dot{\rho}(t) = \mathcal{M}\rho(t) = [\tilde{H}, \rho(t)]/\hbar + \mathcal{L}\rho(t)$, therein \tilde{H} is the Hamiltonian in the full rotating wave approximation. The solution is given by

$$\rho(t) = \exp[\mathcal{M} \cdot (t - t_0)]\rho(t = t_0). \quad (2.54)$$

In principle the superoperator \mathcal{M} projected onto the set of rotated states $\{|\varphi_k\rangle\}$ is complex and nonsymmetric, meaning it is in principle nondiagonalizable. However, there is a way to solve the master equation using the right and left eigenoperators of \mathcal{M} , denote as ρ^n and ρ_n respectively, defined as[49]

$$\mathcal{M}\rho^n = (\Gamma_n + i\Omega_n)\rho^n, \quad \rho_n\mathcal{M} = (\Gamma_n + i\Omega_n)\rho_n, \quad n \in \mathbb{N}. \quad (2.55)$$

The real part of the eigenvalues are always negative numbers, $\Gamma_n < 0$, describing the time scale of relaxation and decoherent processes. On the other hand, the imaginary part Ω_n determines the timescale of coherent processes. The eigenoperators ρ_k and ρ^l constitute a set of biorthogonal operators, i.e. $\text{Tr}[\rho_k^\dagger \rho^l] = \delta_{kl}$. Therefore, we can expand the initial state $\rho(t_0)$ in terms of right eigenoperators, $\rho(t_0) = \sum_{k \in \mathbb{N}} \text{Tr}[\rho_k^\dagger \rho(t_0)] \rho^k$, and hence write the solution (2.54) as

$$\rho(t) = \sum_{k \in \mathbb{N}} \text{Tr}[\rho_k^\dagger \rho(t_0)] \rho^k \exp[(\Gamma_k + i\Omega_k) \cdot (t - t_0)] + \rho^\infty. \quad (2.56)$$

Thus, the transient and the steady dynamics of the system can be determined solving (2.55). The last term on the right hand side corresponds to the eigenoperator with eigenvalue zero, which describes the dynamics of the system at long times. The eigenoperator ρ^∞ is not orthogonal to its counterpart, the left eigenoperator ρ_∞ , and therefore it is given explicitly in Eq. (2.56). To prove this, consider the conservation of the probability, that establish $\sum_l \rho_{ll}(t) = 1$. Thus, the sum $\sum_l \dot{\rho}_{ll}(t) = \sum_{k'l'} [\sum_l \mathcal{M}_{ll,k'l'}] \rho_{k'l'}(t) = 0$, meaning $\sum_l \mathcal{M}_{ll,k'l'} = 0$. Therefore, the superoperator \mathcal{M} has one left eigenoperator with eigenvalue zero, which is the unitary operator $\rho_{\infty,kl} = \delta_{kl}$. In addition, all of the right eigenoperators in Eq. (2.56) decay apart from the steady state ρ^∞ . Therefore $\text{Tr}[\rho^\infty] = 1$, since the trace of the density operator must be unitary any time. With this one can expect that for any right eigenoperator $\text{Tr}[\rho^k] = 0$ for $k \neq \infty$. Using again the conservation of probability, $\sum_l \mathcal{M}_{ll,k'l'} = 0$, we can calculate the trace of ρ^k for $k \neq \infty$, as

$$(\Gamma_k + i\Omega_k) \sum_u \rho_{uu}^k = \sum_{k'l'} \left[\sum_l \mathcal{M}_{ll,k'l'} \right] \rho_{k'l'}^k = 0. \quad (2.57)$$

This implies that either $k = \infty$ or $\sum_u \rho_{uu}^k = 0$.

2.2 Quantum noise

In the previous section we described the effects of the environment fluctuations in the system dynamics by mean of the master equation formulation. Now we shall describe the fluctuations in the system due to its interaction with a dissipative environment. We start with a discussion of some characteristics of noise in driven quantum systems, and its relation with correlation functions. With the regression theorem and the formalism employed in the previous section for the solution of the master equation, we present a method to compute correlation functions and power spectra of system operators.

2.2.1 Noise in nonequilibrium states

Classical noise arises from fluctuations in the motion of particles and in the number of particles within a given volume. Thermal noise and shot noise are two examples. In the quantum regime, noise arises from the uncertainty concerning the position and momentum of quantum mechanical objects. For example, consider the position noise of the linear resonator considered in the previous section. The position auto-correlation function is given by

$$\begin{aligned} C_{xx}(t) = \langle x(t)x(0) \rangle &= x_{ZPF}^2 (\langle a^\dagger(0)a(0) \rangle e^{i\omega_0 t} + \langle a(0)a^\dagger(0) \rangle e^{-i\omega_0 t}) / 2 \\ &= x_{ZPF}^2 (\bar{n}(\hbar\omega_0) e^{i\omega_0 t} + [\bar{n}(\hbar\omega_0) + 1] e^{-i\omega_0 t}) / 2, \end{aligned} \quad (2.58)$$

where we have considered the description of the correlation function in terms of the ladder operator introduced in the last section, where $x(t) = x_{ZPF}(a^\dagger(t) + a(t))/\sqrt{2}$, and $\langle a(0)a(0) \rangle = \langle a^\dagger(0)a^\dagger(0) \rangle = 0$. The above auto-correlation function has a complex nature, due to the commutation rule $[a, a^\dagger] = 1$, which is a consequence of the uncertainty principle between position and momentum, $[x, p] = i\hbar/2$. Furthermore, it reflects the fact that the position operator x does not commute with itself at different times.

The intensity of the noise is characterized by the spectral density or power spectrum, and it is directly related with the auto-correlation function through the Fourier transform. Therefore the power spectrum of the position operator x reads as[13]

$$\begin{aligned} S_{xx}(\omega) &= \int_{-\infty}^{+\infty} dt e^{i\omega t} \langle x(t)x(0) \rangle \\ &= \pi x_{ZPF}^2 (\bar{n}(\hbar\omega_0) \delta(\omega + \omega_0) + [\bar{n}(\hbar\omega_0) + 1] \delta(\omega - \omega_0)), \end{aligned} \quad (2.59)$$

where the two Dirac δ -functions are localized in the negative and positive frequency region of the spectrum. The first Dirac δ -function describes emission and the second one absorption processes. They have different weights for low temperatures as a consequence of the non-commutativity of the position operator with itself at different times. In the high-temperature limit, the weights in Eq.(2.59) become equal and a symmetric power spectrum results.

In driven quantum systems, since time translation symmetry is broken, the power spectrum is determined by the Fourier transform of the time averaged auto-correlation function. The average is taken over the characteristic time of the system. In addition, when the driving is periodic in time, the energy scale of the system is modified and the coherent dynamics can be described in terms of the quasi-energy spectrum. The same holds for noise properties. For instance, in a driven cavity which is modelled by a driven harmonic oscillator, the quasienergy spectrum describes states of a particle in a harmonic potential for a positive

detuning, or concave harmonic potential for a negative detuning. In the former, at very low temperatures, the noise has only positive frequencies, that is, the system is only able to absorb energy. For the latter case, the noise has only negative frequencies and the system is only able to emit energy. For temperatures, where excited states are also occupied, both positive and negative frequencies will appear in the spectrum. Thus, when the cavity interacts with another quantum system by means of the photon number (parametric coupling), the cavity can either amplify the information on the other system for a positive detuning, or de-amplify it for a negative detuning. The equidistant structure of quasi-energy levels in the driven cavity defines a structural noise at a single frequency only, which corresponds to the proper frequency of the cavity detuned by the external modulation.[15]

2.2.2 The regression theorem in a non-stationary state

For stationary systems the power spectrum is just the Fourier transform of the correlation function [cf. Eqs. (2.58) and (2.59)], due to their time translational invariance property. [13] However, in driven systems this property is missing, and the system noise varies in time.[50, 51] By the quantum correspondence principle the above correlation function can be defined for operators, with a non-symmetric behaviour of the power spectrum appearing due to the noncommuting algebra for the operators. To compute this correlation function, and higher correlation function as well, Lax [51] has proposed a method which has been called *quantum regression theorem*. In the following, we shall briefly derive the Lax formula, which describe the cross correlation function of arbitrary operators, $C_{AB}(t, \tau) = \langle A(t + \tau)B(t) \rangle$, as a mean value. We start with the cross correlation function of operators A and B in the Heisenberg picture

$$C_{AB}(t, \tau) = \text{Tr}_{\text{S} \oplus \text{B}} [W(0)A(t + \tau)B(t)], \quad (2.60)$$

where $\text{Tr}_{\text{S} \oplus \text{B}}[\dots]$ denotes the trace over the degrees of freedom of the whole system, system plus bath. One can reorganize the time evolution in the trace using its cyclic property, yielding

$$C_{AB}(t, \tau) = \text{Tr}_{\text{S} \oplus \text{B}} [{}_B W(t + \tau)A(0)], \quad (2.61)$$

where ${}_B W(t + \tau) = \mathcal{U}(t + \tau, t)[B(0)W(t)]\mathcal{U}^\dagger(t + \tau, t)$. There, the correlation between A and B has the structure of a mean value with ${}_B W(t)$ in the role of an effective density operator. This artificial density operator follows the same dynamics as W , but without its probabilistic interpretation, i.e. $\text{Tr}_{\text{S} \oplus \text{B}}[{}_B W] \neq 1$. Hence, it follows the von-Neumann equation

$$\frac{d}{d\tau} {}_B W(t + \tau) = \frac{i}{\hbar} [H(t + \tau), {}_B W(t + \tau)], \quad (2.62)$$

with the separable initial state ${}_B W(t) = B(0)W(t) \sim (B(0)\rho(t)) \otimes \rho_B$, because in the regime of weak coupling to the bath $W(t)$ should only show deviations of the order of the interaction term, H_{SB} , from an uncorrelated state.

If we are to eliminate explicit reference to the environment in (2.61) we need to evaluate the environment trace over ${}_B W(t + \tau)$ to obtain the reduced operator ${}_B \rho(\tau + t)$, where ${}_B \rho(t) = B(0)\rho(t)$. Thus, following the same procedure as in Sec. 2.1.3, the virtual reduced density operator after time τ is given by

$${}_B \rho(t + \tau) = \sum_{k \in \mathbb{N}} \text{Tr}[\rho_k^\dagger B(0)\rho(t)] \rho^k \exp[(\Gamma_k + i\Omega_k)\tau]. \quad (2.63)$$

Considering an initial time in the steady state regime, i.e., $\rho(t) \rightarrow \rho^\infty$, the correlation function reads

$$C_{AB}(\tau) = \sum_{k \in \mathbb{N}} \text{Tr}[\rho_k^\dagger B(0)\rho^\infty] \text{Tr}[A(0)\rho^k] \exp[(\Gamma_k + i\Omega_k)\tau], \quad (2.64)$$

and therefore

$$S_{AB}(\omega) = 2 \sum_k \frac{(\text{Tr}[\rho_k^\dagger B(0)\rho^\infty] \text{Tr}[A(0)\rho^k]) \Gamma_k}{(\omega - \Omega_k)^2 + \Gamma_k^2}. \quad (2.65)$$

The sum extends over those eigenoperators ρ^k which belong to non-zero eigenvalues. Thereby, we have not included the elastic peak $\langle A \rangle \langle B \rangle \delta(\omega)$ which trivially comes from the stationary state ρ^∞ .

Noise properties of the quantum Duffing oscillator

In recent years, considerable interest has developed in driven nonlinear quantum resonators due to the tremendous progress in fabricating and thus controlling individual macroscopic quantum systems operating on the nanoscale. This includes superconducting Josephson junctions [17, 52–54] in different variants and also nanomechanical devices which have successfully been realized in the deep quantum regime only recently. [55–57] In addition, quantum transport devices on the basis of molecular junctions have been realized where the interplay of charge transport and vibrational properties of the molecular bridge has been studied.[58, 59] An important aspect common to all these approaches lies in the fact that the nonlinear response and the noise properties of *single* macroscopic quantum systems can be addressed instead of measuring an ensemble of resonators where additional averaging is intrinsically involved.

Coupling a driven quantum mechanical oscillator to environmental fluctuations allows the resonator dynamics to reach a stationary state. In the stationary state, energy is coherently absorbed from the pump and leaks into the environment via random dissipative transitions, which inevitably induce noise in the resonator. This occurs even at zero temperature where only environmental zero-point quantum fluctuations (quantum noise) exist. The quantum noise properties of a nonlinear oscillator determine many fundamental nonequilibrium phenomena such as quantum heating [60–62] and quantum activation.[63]

In general, nonlinear oscillators are naturally used as basic elements for quantum state detection or amplification. Examples of those are the Josephson bifurcation amplifier [17–22] and the cavity bifurcation amplifier.[17, 23] In this context, the noise properties of the resonator, which is used as detector or amplifier, determine the backaction of the measurement or amplification on the system itself.[9, 13, 64] Clearly, it is desirable to keep the

backaction as weak as possible, while on the other hand, a significant coupling of the amplification or measurement device to the system is useful in order to achieve a sufficiently strong detection or amplification efficiency. A fundamental lower limit for the disturbance introduced by the noisy detector into the qubit to be detected, however, will be set by the quantum noise acting in the detector. Hence, in order to design useful concepts for quantum state detection based on nonlinear resonators in the deep quantum regime, their quantum noise properties have to be addressed.

The Josephson bifurcation amplifier [17–22] takes advantage of the dynamically induced bistability due to the intrinsic nonlinearity of the resonator. The eigenstates of the qubit whose state has to be measured are mapped onto the coexisting stable states of forced vibrations of the resonator, which have different amplitudes and phase relations relative to the phase set by the external drive. Hence, they allow for a large discrimination power. Up to present, these amplifying devices mostly operate in the semiclassical regime where many quanta in the resonator are excited. This implies that pure quantum fluctuations are typically small on average. Nevertheless, some experiments have been realized at low temperature where the relevant fluctuations are quantum mechanical in nature.[17, 22] The regime of weak fluctuations has been the subject of intense theoretical investigation.[60–62, 64–69] It has been shown,[60–62] that a stationary distribution over the quasienergy states of the driven oscillator at zero temperature can be reached which has the form of an effective Boltzman distribution with an associated nonzero effective temperature even when the statistical temperature is set to zero. Since only the zero-point fluctuations of the vacuum are responsible for this stationary distribution, this has been denoted as *quantum heating*.[62] This stationary state is reached via activation-type transitions between discrete quasienergy states of forced vibrations which are induced by zero-temperature quantum noise [60–62] and are therefore called *quantum activation* transitions.[63]

Signatures of the onset of quantum fluctuations can be seen in the relative intensities of the lines of the resonator noise spectrum [62, 65–68] and in the appearance of a fine structure in the spectral lines of resonators with comparatively large nonlinearities and large quality factors.[62, 67] Most importantly, it has been shown that the spectral fine structure of the noise power spectrum of a parametrically modulated oscillator yields detailed information on the population of the quasienergy states of the resonator in its stationary state.[62, 67] Since the noise power spectrum is in principle experimentally accessible, one can directly deduce the stationary nonequilibrium occupation distribution from this measurement signal. No other means is so far available to achieve this. Below, we also find a spectral fine structure in the noise power spectrum of the quantum Duffing oscillator which possesses a similar topology as the parametric oscillator.

In this chapter, we investigate the quantum noise properties of modulated nonlinear

oscillators in the deep quantum regime. As the simplest example, we consider a monostable anharmonic oscillator which has a quartic nonlinearity (quantum Duffing oscillator). Such a device can be parametrically coupled to a qubit [69] and thus, its photon noise characteristics is of relevance when used as a parametric detector. Below, we analyse the power spectrum of the photon number fluctuations in the quantum Duffing oscillator. In the underdamped regime, we identify Lorentzian peaks in the power spectrum of the photon number noise which are associated to the multiphoton transitions in the quantum Duffing oscillator. Their intensities are determined by the stationary occupation probabilities of the quasienergy states. The latter is directly connected to the effective quantum temperature which can be identified in the stationary state and which is intimately connected to the quantum squeezing of the quasienergy states. Hence, measuring the power spectrum of the photon number fluctuations provides a direct and elegant way to determine the stationary occupation probabilities of the quasienergy states and thus the effective quantum temperature.

A weakly nonlinear Duffing oscillator has a remarkable symmetry: its energy levels E_n with $n \leq N$ are pairwise resonant for the same driving frequency ω_{ex} , $E_{N-n} - E_n = (N - 2n)\hbar\omega_{\text{ex}}$. An example of the energy spectrum for the case $N = 3$ is sketched in Fig. 3.1(a). After preparing the oscillator in its n -th excited state $n \leq N$, it displays periodic quantum oscillations between the n -th and the $N - n$ -th excited states. During these oscillations, $|N - 2n|$ photons are being exchanged between the oscillator and the modulation field. The oscillations of the photon number \hat{n} are usually referred to as multiphoton Rabi oscillations. Their characteristic frequency, the Rabi frequency $\Omega_{n,N}$, depends on the intensity of the driving field and on the number of photons exchanged. The Rabi frequency $\Omega_{0,N}$ for the N -photon oscillations is the smallest Rabi frequency. The multiphoton Rabi oscillations with $N - n$ photons involved are underdamped if their Rabi frequency $\Omega_{n,N}$ exceeds the dissipative rate of photon leaking into the environment. The latter is the oscillator relaxation rate γ . For $\gamma \ll \Omega_{0,N}$ all the Rabi oscillations are in general underdamped. The periodically driven resonator reaches its stationary state on the time-scale γ^{-1} .

In the stationary state, quantum noise induces – even at zero temperature – fluctuations in the photon number \hat{n} . The dynamics of these fluctuations is characterized by multiphoton oscillations which manifest themselves as peaks in the noise spectrum $S(\omega)$ of \hat{n} , located at plus/minus the Rabi frequencies $\Omega_{n,N}$. In the underdamped regime, the dissipative dynamics of the driven oscillator is most appropriately described in terms of random transitions between the oscillator quasienergy states. When the driving is resonant, the pairs of oscillator Fock states with n - and $N - n$ -photons are resonantly superposed. The corresponding oscillator quasienergy states are a symmetric and an antisymmetric superposition of the two Fock states. Their splitting in quasienergy is given by the Rabi frequency $\Omega_{n,N}$. The

corresponding peak in the noise spectrum at $(-)\Omega_{n,N}$ is due to random transitions from the state with (highest) lowest to that with the (lowest) highest quasienergy of the doublet. The peak intensity is proportional to the stationary occupation probability of the initial quasienergy state. Therefore, the noise spectrum offers a convenient way to directly probe the stationary nonthermal distribution over all the quasienergy states. Moreover, for weak driving and exactly zero detuning from the multiphoton resonance, the noise spectrum of the \hat{n} -photon transition is symmetric, i.e., $S(\omega) = S(-\omega)$ and two inelastic peaks are signatures of an oscillatory decay of the fluctuations towards the stationary state. States belonging to a multiphoton doublet then have the same stationary occupation probabilities. For a weakly detuned modulation or a stronger driving, the spectrum becomes asymmetric. Besides, an additional quasielastic peak appears at zero frequency which represents incoherent relaxation of the fluctuations towards the stationary state. These features have some analogy in the spectral correlation function of a (static) quantum mechanical two-level system weakly coupled to a dissipative harmonic bath.[28] There, the spin correlation function is a sum of three Lorentzian peaks. The two inelastic peaks are symmetrically located at finite frequencies and their width determines the inverse of the dephasing time. In addition, the quasielastic peak at zero frequency represents incoherent relaxation with the inverse relaxation time given by its width. In the driven system, the appearance of a quasielastic peak depends on the intriguing interplay between the nonlinearity, the driving strength and the dissipation strength. The contents of this Chapter have been published in Ref. 70.

3.1 Coherent dynamics

3.1.1 Induced multiphoton Rabi oscillations in the Duffing oscillator

We consider a periodically modulated Duffing oscillator with mass m , eigenfrequency ω_0 and a quartic (Kerr) nonlinearity characterized by the strength α , described by the Hamiltonian

$$H(t) = \frac{1}{2m}p^2 + \frac{1}{2}m\omega_0^2x^2 + \frac{1}{4}\alpha x^4 + Fx \cos(\omega_{\text{ex}}t). \quad (3.1)$$

The modulation amplitude F is assumed to be sufficiently small that it induces only weakly nonlinear vibrations. This is guaranteed by the condition $\alpha A^2 \ll m\omega_0^2$, with $A(F)$ being the typical amplitude of the nonlinear vibrations. The modulation frequency ω_{ex} is chosen to be close to the oscillator eigenfrequency ω_0 such that the detuning $\delta\omega$ is small, i.e.,

$$\delta\omega \ll \omega_0, \quad \delta\omega \equiv \omega_0 - \omega_{\text{ex}}. \quad (3.2)$$

The theory presented here applies to hard as well as to soft nonlinearities $\alpha \lesssim 0$, but for concreteness we will focus on the case of a hard nonlinearity, $\alpha > 0$.

The quantum dynamics of the weakly detuned and weakly nonlinear driven oscillator is most conveniently described in terms of the oscillator ladder operators a and a^\dagger , in a rotating frame determined by the unitary transformation

$$R(t) = \exp[-i\omega_{\text{ex}} a^\dagger a t]. \quad (3.3)$$

In the rotating frame, the typical time scale of the resonator dynamics is given by $\delta\omega^{-1}$, so that terms oscillating with frequencies $\pm 2\omega_{\text{ex}}$ and $\pm 4\omega_{\text{ex}}$ average out and can be neglected in the transformed Hamiltonian $R(t) H(t) R^\dagger(t) - i\hbar R(t) \dot{R}^\dagger(t)$. Thereby, we obtain the RWA Hamiltonian

$$\tilde{H} = \delta\omega \hat{n} + \nu \hat{n}(\hat{n} + 1)/2 + f(a^\dagger + a)/2, \quad (3.4)$$

where $\hat{n} \equiv a^\dagger a$ is the photon number operator, ν and f are the frequencies associated with the Kerr nonlinearity and the external field amplitude at the quantum scale $x_{\text{ZPF}} = \sqrt{\hbar/m\omega_0}$, i.e., $\nu = 3\alpha x_{\text{ZPF}}^4/4\hbar$ and $f = Fx_{\text{ZPF}}/\sqrt{2\hbar}$. In order to keep the notation compact we have set $\hbar = 1$ in Eq. (3.4) and in the remainder of the paper. The oscillator quasienergies ε_n and quasienergy states $|\psi_n\rangle$ are the eigenvalues and eigenvectors of the rotating wave Hamiltonian, $\tilde{H}|\psi_n\rangle = \varepsilon_n|\psi_n\rangle$.

A key property in the dynamics of the Duffing oscillator is its nonlinearity, which generates multiphoton transitions at frequencies ω_{ex} close to the fundamental frequency ω_0 . In order to see this, one can consider the undriven nonlinear oscillator, switching off adiabatically the external modulation. There the Floquet states $|\psi_n\rangle$ become oscillator Fock states $|n\rangle$, yielding the following quasienergy spectrum

$$\varepsilon_n = \delta\omega n + \nu n(n + 1)/2, \text{ for } f \rightarrow 0. \quad (3.5)$$

Thus, in the undriven scenario the quasienergies depend linearly on external frequency so that at some frequency values different quasienergy levels ε_n intercept, such as ε_n and ε_{N-n} for $N > n$, when the detuning follows

$$\delta\omega = \nu(N + 1)/2 \equiv \delta\omega_N. \quad (3.6)$$

This resonance condition sets the amount of the external frequency to be a factor of the difference of energy levels of the nonlinear oscillator in the static frame $E_{N-n} - E_n$ [cf. Fig. 3.1a],

$$E_{N-n} - E_n \approx (N - 2n)\omega_{\text{ex}}. \quad (3.7)$$

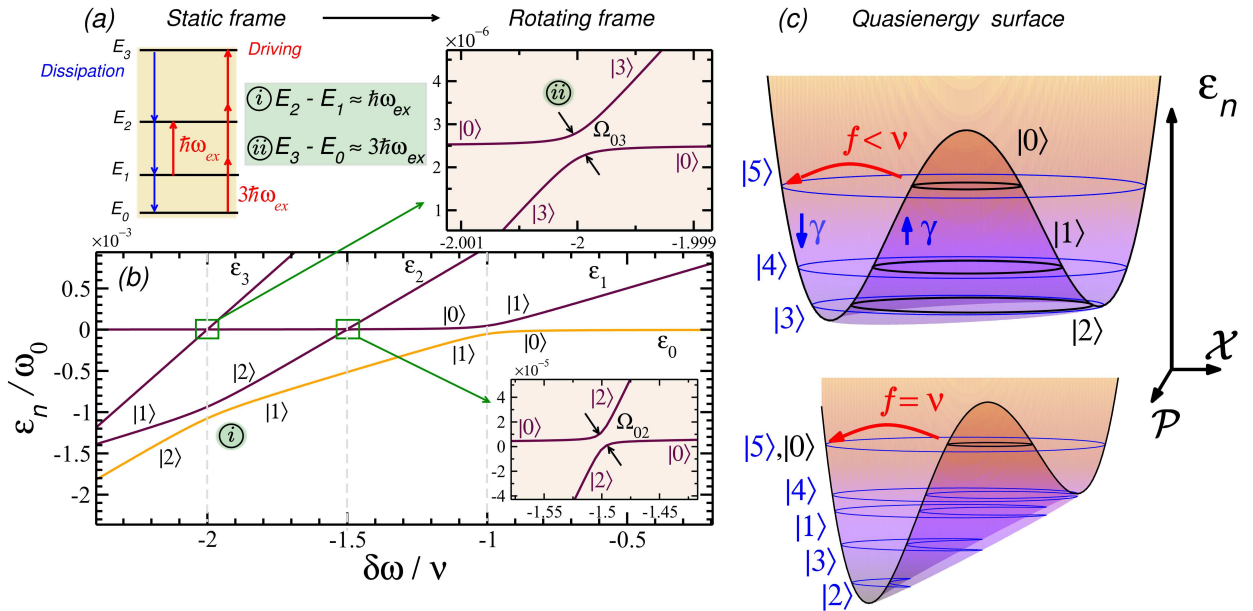


Figure 3.1: Multiphoton Rabi transitions around the $N = 3$ -photon resonance $\delta\omega = \delta\omega_3$. In panel (a) we depict a sketch of the driving-induced resonant 3-photon transitions (red arrows) in the nonlinear oscillator. Likewise, the blue arrows indicate the noise-induced relaxation process. In panel (b), we show the underlying quasienergy spectrum as a function of the external frequency together with two zooms to the avoided crossings for the 2- and 3-photon Rabi transitions for $\nu = 10^{-3}\omega_0$ and $f = \nu/10$. In panel (c), we schematically indicate of the coherent multiphoton Rabi transitions (red arrow) and the dissipative transitions (blue arrows) on the quasienergy surface which results from a semiclassical approach, see text. The upper figure shows the less tilted case when $f = \nu/10$, while for the lower figure $f = \nu$. We emphasize that relaxational transitions at zero temperature typically occur in both directions, i.e., downwards *and* upwards along the quasienergy surface, which is in striking contrast to dissipative transitions in *static* potential surfaces, where only “downward relaxation” is possible. An escape due to “upward relaxation” is known as quantum activation [63].

For a finite driving ($f \neq 0$), the driving term [cf. Eq.(3.4)] mixes the degenerate levels, $|n\rangle$ and $|N - n\rangle$. According to the von-Neumann-Wigner theorem (level repulsion), these quasienergy levels will no longer cross. In other words, the degeneracy is lifted and avoided quasienergy level crossing form, which is a signature of discrete multiple multiphoton transitions [cf. Fig. 3.1b]. There, up to leading order in the driving, the Floquet states $|\psi_n\rangle$ for $n \leq N \neq N/2$ are a resonant admixture of the pair $|n\rangle$ and $|N - n\rangle$,

$$|\psi_n\rangle \approx (|n\rangle \pm |N - n\rangle) / \sqrt{2}. \quad (3.8)$$

We choose the signs $-$ and $+$ for $n < N/2$ and $N/2 < n \leq N$, respectively. The states $|\psi_n\rangle$ which are not involved in a multiphoton transition ($n > N$ and $n = N/2$ for N even) can be approximated as the corresponding Fock state $|\psi_n\rangle \approx |n\rangle$. Therefore, if the system

is prepared initially in the state $|n\rangle$ ($n < N$) in the presence of a driving field at resonance with the N th multiphoton transition ($\delta\omega = \delta\omega_N$), it switches continuously between the pair of states $|n\rangle$ and $|N-n\rangle$. The time scale of these virtual processes is set by the splitting in the corresponding avoided quasienergy level crossing, $|\varepsilon_n - \varepsilon_{N-n}|$, which is different from zero for finite driving. This energy splitting, as well called the Rabi frequency, of the multiphoton oscillations is given by

$$\Omega_{n,N-n} = |\varepsilon_n - \varepsilon_{N-n}| = f (f/\nu)^{N-2n-1} \frac{(N-n)!^{1/2}}{n!^{1/2}(N-2n-1)!^2}. \quad (3.9)$$

The resonant condition in Eq. (3.6) is not renormalized by a finite driving (within the RWA) but for a comparatively larger driving $f \sim \nu \ll \omega_0$, the multiphoton transitions have to be reinterpreted as tunneling transitions between semiclassical states.

As we shall detail in Section 3.3, the multiphoton Rabi oscillations induce peaks in the spectral densities of oscillator observables only when the Rabi frequency $\Omega_{0,N}$ for the multiphoton transition from the zero-photon ground state is larger than the noise-induced level broadening of the relevant quasienergy levels ε_0 and ε_N . In the next section, we will pave the way for the calculation of the noise spectrum in this regime, by formulating the master equation for a weakly nonlinear oscillator and by evaluating the stationary occupation populations of the quasienergy states.

3.2 Stationary dissipative dynamics in the deep quantum regime

In the presence of a weak bilinear coupling to the fluctuations of a bosonic bath, the assumptions of small detuning and weak nonlinearity that under the RWA naturally lead to a Liouville-von Neuman master equation in the Lindblad form, discussed in Section 2.1.4, for the density matrix ρ of the weakly damped oscillator in the rotating frame.[47, 48]

3.2.1 The stationary distribution

For long times, the density matrix in the rotating frame ρ relaxes to a stationary state ρ^∞ , satisfying

$$\mathcal{M}\rho^\infty = 0. \quad (3.10)$$

When the oscillator decay rate γ is larger than the driving, $\gamma \gg f$, the width of the resonant quasienergy levels ε_n induced by the bath fluctuations are larger than the corresponding Rabi frequency $\Omega_{n,N-n}$ of the multiphoton transitions. Then, the multiphoton

resonances are smeared out and the coherent effects associated with multiphoton oscillations are strongly suppressed. Hence, dissipation sets a lower limit for the driving strength, $f \gg \gamma$. On the other hand, for comparatively larger driving $f \sim \nu$ quantum fluctuations become small and the oscillator is latched to a classical attractor for a time much longer than the typical time scale of relaxation, γ^{-1} . In this regime, the (quasi)stationary distribution over the quasienergy states is of Boltzman type. Here, we restrict our analysis to the deep quantum regime where the driving is larger than the damping but smaller than the nonlinearity, $\gamma \ll f \ll \nu$. Thereby we have implicitly assumed a comparatively large nonlinearity $\nu \gg \gamma$.

Underdamped regime:

We start our discussion assuming that all Rabi oscillations are underdamped. Put differently, we assume that the smallest Rabi frequency $\Omega_{0,N}$ is larger than the relevant level width. We refer to this regime as the fully underdamped regime. In the fully underdamped regime, the off-diagonal matrix elements of the density matrix ρ^∞ projected onto the quasienergy basis $|\psi_l\rangle$ are negligible and we can set them to zero (secular approximation), i.e.,

$$\rho_{lk}^\infty \equiv \langle \psi_l | \rho^\infty | \psi_k \rangle = 0 \quad \text{for} \quad l \neq k . \quad (3.11)$$

Then, a balance equation for the stationary occupation probabilities ρ_{ll}^∞ follows from Eqs. (2.52) and (3.10) according to

$$\gamma_l \rho_{ll}^\infty - \sum_{l \neq k} W_{l,k} \rho_{kk}^\infty = 0. \quad (3.12)$$

Here, $W_{l,k}$ is the transition rate from state $|\psi_l\rangle$ to state $|\psi_k\rangle$ given by

$$W_{k,l} \equiv \gamma \left((1 + \bar{n}) |\langle \psi_k | a | \psi_l \rangle|^2 + \bar{n} |\langle \psi_k | a^\dagger | \psi_l \rangle|^2 \right) , \quad (3.13)$$

and γ_l is the linewidth of quasienergy level ε_l , $\gamma_l \equiv \sum_{k \neq l} W_{kl}$. We can now formulate more precisely the condition for underdamped Rabi oscillations of the narrowest resonance, $\Omega_{0,N} \gg \gamma_0$.

The solution for stationary occupation probabilities up to leading order in the small parameters f/ν and \bar{n} is given in Ref. 47. The pair of multiphoton states $|\psi_n\rangle$ and $|\psi_{N-n}\rangle$ in Eq. (3.8) have equal stationary occupation, $\rho_{nn}^\infty = \rho_{N-n,N-n}^\infty$. The smallest pair of occupation probabilities is $\rho_{00}^\infty = \rho_{NN}^\infty$. The occupation probability grows algebraically as

$$\rho_{n+1,n+1}^\infty = \frac{N-n}{n+1} \rho_{nn}^\infty \quad \text{for} \quad n < N/2 . \quad (3.14)$$

The states $|\psi_l\rangle$ with $l > N$ have vanishing occupation probability, $\rho_{ll}^\infty = 0$. The degeneracy $\rho_{00}^\infty = \rho_{NN}^\infty$ is approximate and is lifted for higher orders in f/ν .

Quasienergy distribution close to a multiphoton resonance:

One can easily generalize the above expressions to the case where the detuning $\delta\omega$ does not exactly match the resonance condition, $\delta\omega \neq \delta\omega_N$. Since the Rabi frequencies for the different pairs of resonance transitions in Eq. (3.9) are exponentially different, we can choose $|\delta\omega - \delta\omega_N| \ll \Omega_{1,N-1}$, so that all the pairs of Fock states $|n\rangle$ and $|N-n\rangle$ with $1 < n < N/2$ are still resonantly superposed, except for

$$|\psi_0\rangle = \cos\frac{\theta}{2}|0\rangle - \sin\frac{\theta}{2}|N\rangle, \quad \text{and} \quad |\psi_N\rangle = \sin\frac{\theta}{2}|0\rangle + \cos\frac{\theta}{2}|N\rangle, \quad (3.15)$$

with $\theta = \tan^{-1}[\Omega_{0,N}/N(\delta\omega - \delta\omega_N)]$. The corresponding solution for the stationary density matrix close to resonance is [cf. App. B]

$$\begin{aligned} \rho_{NN}^\infty &= \rho_{00}^\infty \tan^4\frac{\theta}{2}, & \rho_{11}^\infty &= \rho_{00}^\infty N \tan^2\frac{\theta}{2}, \\ \rho_{n+1n+1}^\infty &= \frac{N-n}{n+1} \rho_{nn}^\infty & \text{for} & \quad 1 \leq n < N/2. \end{aligned} \quad (3.16)$$

Partially underdamped regime

Next we consider a comparatively large relaxation rate γ , so that the narrowest Rabi resonance is overdamped but the remaining resonances are still underdamped, $\Omega_{0,N} \ll N\gamma \ll \Omega_{1,N-1}$. We refer to this regime as the partially underdamped regime. Then, incoherent multiphoton transitions from the ground state $|0\rangle$ to state $|N\rangle$ with a small rate $\Omega_{0,N}^2/(N\gamma)$ and the subsequent emission of excitations into the bath determines a small but finite occupation of the resonant states ρ_{nn}^∞ , $n \geq 1$. Formally, the stationary distribution ρ^∞ can be obtained by setting all the off-diagonal elements of ρ_{ik}^∞ to zero except for ρ_{N0}^∞ and ρ_{0N}^∞ and solving Eq. (3.10). Thereby, we find

$$\begin{aligned} \langle 0|\rho^\infty|0\rangle &\approx 1, & \langle N|\rho^\infty|N\rangle &\approx \Omega_{0,N}^2/(N^2\gamma^2) \\ \rho_{11}^\infty &= \Omega_{0,N}^2/(N\gamma^2) & \text{for} & \quad \Omega_{0,N}^2/(N\gamma^2) \gg \exp[-\omega_0/(k_B T)] \\ \rho_{n+1n+1}^\infty &= \frac{N-n}{n+1} \rho_{nn}^\infty & \text{for} & \quad 1 \leq n < N/2. \end{aligned} \quad (3.17)$$

The crossover between this solution and the fully underdamped solution Eq. (3.14) is given in 47. Both distributions are determined by quantum fluctuations and are very different from the Boltzman-type distribution for a driven resonator latched to a classical attractor.

3.2.2 The nonlinear response of the oscillator

In the stationary limit $t \gg \gamma^{-1}$, the oscillator state is described by the time-independent density matrix ρ_∞ and the oscillator dynamics is embedded in the time-dependent frame

of reference $R(t)$ [cf. Eq. (3.3)]. The mean value of an observable O is

$$\langle O(t) \rangle_\infty \equiv \lim_{t \rightarrow \infty} \langle O(t) \rangle = \text{Tr} \langle \rho^\infty R^\dagger(t) O R(t) \rangle. \quad (3.18)$$

In the RWA, the stationary vibrations $\langle x(t) \rangle_\infty$ are sinusoidal,

$$\langle x(t) \rangle_\infty = \sqrt{2} x_{\text{ZPF}} \cos(\omega_{\text{ex}} t + \varphi) |\langle a \rangle_\infty|, \quad \langle a \rangle_\infty = \sum_{lk} \rho_{lk}^\infty \langle \psi_l | a | \psi_k \rangle. \quad (3.19)$$

It has been shown that the nonlinear response of the oscillator as a function of the driving ω_{ex} shows resonances and antiresonances in the deep quantum regime.[47, 48, 71] The response is proportional to the transmitted amplitude in a heterodyne measurement scheme and it has already been measured for a weakly nonlinear oscillator.[72] Here, we would only like to remark that this kind of measurement, or any measurement which probes the stationary mean values as opposed to correlation functions does not allow to address the different degenerate resonances separately, and to access the stationary distribution ρ_{ll}^∞ directly. In the next section, we will show that this can be achieved by measuring the power spectrum of the photon number noise.

3.3 Photon noise in the deep quantum regime

In this section, we are specifically interested in the noise spectrum $S(\omega)$ of the autocorrelator of the photon number \hat{n} , $\langle \hat{n}(t + \delta t) \hat{n}(t) \rangle_\infty$. From Eq. (2.61), we find

$$\langle \hat{n}(t + \delta t) \hat{n}(t) \rangle_\infty = \text{Tr} [\hat{n} \exp[\mathcal{M} \delta t] \hat{n} \rho^\infty]. \quad (3.20)$$

Here, \mathcal{M} is the Liouville superoperator, defined in Eq. (2.54). Since this correlator does not depend on the initial time t as a consequence of the RWA, we can define the noise spectrum in terms of a single average over quantum fluctuations according to

$$S(\omega) = 2 \text{Re} \int_0^\infty dt e^{i\omega t} \langle \hat{n}(t) \hat{n}(0) \rangle_\infty. \quad (3.21)$$

It is useful to separate the contributions to $S(\omega)$ into those coming from the expectation value of \hat{n} , and those from its fluctuations, i.e.,

$$\begin{aligned} S(\omega) &= \langle \hat{n} \rangle_\infty^2 \delta(\omega) + \delta S(\omega), \\ \delta S(\omega) &\equiv 2 \text{Re} \int_0^\infty dt e^{i\omega t} \langle \delta \hat{n}(t) \delta \hat{n}(0) \rangle_\infty. \end{aligned} \quad (3.22)$$

Here, $\delta \hat{n}$ is the operator for the photon number fluctuations, i.e., $\delta n = \hat{n} - \langle \hat{n} \rangle_\infty$.

Our path to compute the noise spectrum consists in three steps: i) We express the virtual preparation $\hat{n}\rho^\infty$ in terms of right eigenvectors of the superoperator \mathcal{M} . ii) We plug the resulting decomposition into Eq. (3.20). Then, each term decays exponentially with a different exponent which is given by the corresponding eigenvalue of \mathcal{M} . iii) We compute the Fourier integral in Eq. (3.21), which thereby yields a sum over (overlapping) Lorentzian peaks.

3.3.1 Noise spectrum in the underdamped regime

When all the multiphoton Rabi oscillations are underdamped, $\Omega_{0,N} \gg \Gamma_N$, the coherences $|\psi_{N-n}\rangle\langle\psi_n|$ and $|\psi_n\rangle\langle\psi_{N-n}|$ are approximate eigenvectors of the Liouvillian \mathcal{M} . Then,

$$\begin{aligned}\mathcal{M}|\psi_n\rangle\langle\psi_{N-n}| &= -(\Gamma_n - i\Omega_{n,N-n})|\psi_n\rangle\langle\psi_{N-n}| \quad \text{for } n < N/2, \\ \mathcal{M}|\psi_{N-n}\rangle\langle\psi_n| &= -(\Gamma_n + i\Omega_{n,N-n})|\psi_{N-n}\rangle\langle\psi_n| \quad \text{for } n < N/2,\end{aligned}\quad (3.23)$$

with the level widths being given as $\Gamma_n = \gamma_n = \gamma(\bar{n} + 1/2)N + \gamma\bar{n}$ for $n < (N-1)/2$. For N odd, $\Gamma_{(N-1)/2} = \gamma(1 + 2\bar{n})(5N+1)/8 + \gamma\bar{n}$. Up to leading order in f/ν , the decomposition of the virtual preparation $\hat{n}\rho^\infty$ in terms of right eigenvectors of \mathcal{M} has the simple expression

$$\hat{n}\rho^\infty \approx (N/2)\rho^\infty - \sum_{n < N/2} (N/2 - n)\rho_{nn}^\infty (|\psi_n\rangle\langle\psi_{N-n}| + |\psi_{N-n}\rangle\langle\psi_n|). \quad (3.24)$$

Clearly, each term of the above decomposition yields a Lorentzian peak in the noise spectrum $S(\omega)$. The first term yields the contribution to $S(\omega)$ from the expectation value of \hat{n} , $(N/2)^2\delta(\omega)$. The remaining terms yield inelastic peaks associated to random transitions between quasienergy states belonging to the same multiphoton doublet. Since the populations ρ_{nn}^∞ and $\rho_{N-n,N-n}^\infty$ are approximately equal, peaks at opposite frequency have approximately equal intensity. By putting together Eqs. (3.20), (3.21), (3.23), and (3.24), we find $S(\omega) = (N/2)^2\delta(\omega) + \delta S(\omega)$ with

$$\delta S(\omega) \approx \sum_{n < N/2} S_n(\omega) + S_{N-n}(\omega), \quad (3.25)$$

$$S_n(\omega) = S_{N-n}(-\omega) = \frac{2\Gamma_n\rho_{nn}^\infty(N/2 - n)^2}{(\omega - \Omega_{n,N-n})^2 + \Gamma_n^2}. \quad (3.26)$$

Hence, the Lorentzian peaks are centred at the multiphoton Rabi frequencies $\Omega_{n,N-n}$ and have a resonance width of Γ_n . The factor $(N - 2n)^2/4$ is the leading order expression for the squared matrix element $|\langle\psi_n|\hat{n}|\psi_{N-n}\rangle|^2$. Remarkably, the line intensities depend only weakly on the driving f and on the temperature through the stationary distribution ρ_{nn}^∞ . Up to leading order, the driving f enters only in the splitting of the lines through the Rabi

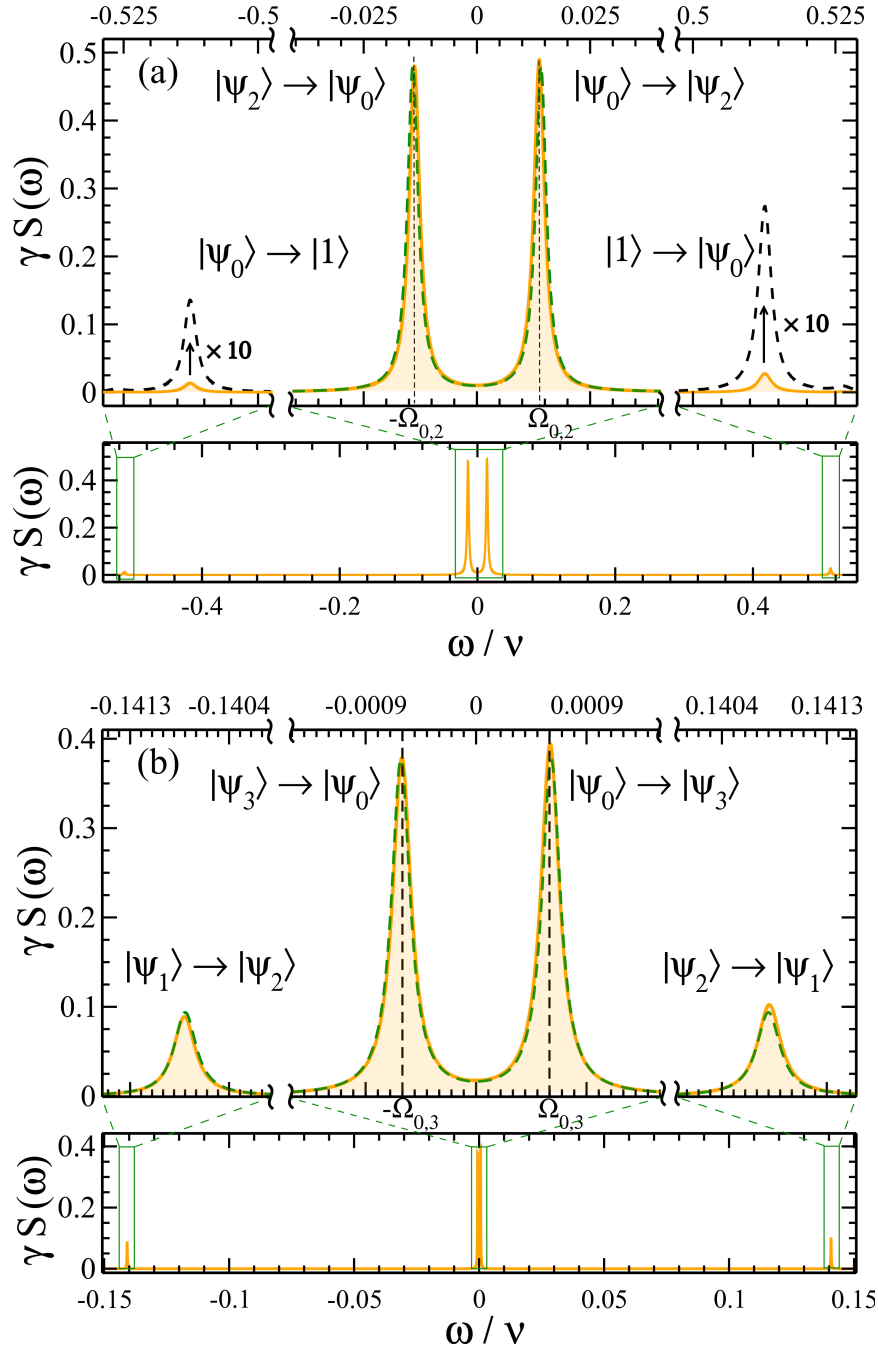


Figure 3.2: Photon noise spectrum at the $N = 2$ - and the $N = 3$ -photon resonance are shown in panel (a) and (b) respectively for $\nu = 10^{-3}\omega_0$, $f = \nu/10$, $\gamma = \Omega_{0,2}/10$ in (a) and $\gamma = \Omega_{0,3}/10$ in (b). Shown are the approximate results obtained with Eq. (3.25) (dashed green lines), and the results from a full numerical solution of the general expression for the spectrum derived in 2.2 (orange solid lines). The gray lines in panel (a) mark a zoom to the subleading off-resonant transitions.

frequencies. Notice that Eq. (3.25) is valid only in the vicinity of a multiphoton peak since terms of order γ are not taken into account. In order to evaluate the tails of the peaks more precisely, one has to take into account the contribution stemming from all eigenvectors of \mathcal{M} .

In the top and bottom panels of Fig. 3.2, we show the noise spectrum $S(\omega)$ for the cases $N = 2$ and $N = 3$, respectively. The noise spectrum for $N = 2$ shows a pair of symmetric peaks which correspond to the transitions $|\psi_0\rangle \leftrightarrow |\psi_2\rangle$. Likewise, the noise spectrum for $N = 3$ displays two pairs of symmetric peaks corresponding to the transitions $|\psi_0\rangle \leftrightarrow |\psi_3\rangle$ and $|\psi_1\rangle \leftrightarrow |\psi_2\rangle$. The green dashed lines mark the results from our approximate analytical formula in Eq. (3.25) while the yellow solid lines show the data obtained by numerically evaluating the expression in Eq. (2.65). An excellent agreement is found.

In Fig. 3.2(a), additional smaller side peaks of the order of f/ν are also visible, see the black-dashed lines representing a ten-fold zoom. They are not associated to any resonant transition between multiphoton states and are thus not captured by the leading order expression given in Eq. (3.25). The particular subleading peaks in Fig. 3.2(a) belong to the transitions $|\psi_0\rangle \leftrightarrow |1\rangle$.

These features have a direct analogy in the spectral correlation function of a static quantum mechanical two-level system which is weakly coupled to a dissipative harmonic bath.[28] For a general biased two-state system with anticrossing energy levels, the pair correlation function is a sum of three Lorentzian peaks. The two inelastic peaks are symmetrically located at finite frequencies and their width determines the inverse of the dephasing time. For a biased static two-level system away from resonance, an additional quasielastic peak at zero frequency appears which represents incoherent relaxation with the inverse relaxation time given by its width. Since we consider here the case strictly at resonance (in the RWA), no zero-frequency peak is present.

3.3.2 Photon antibunching

In general, the photon emission characteristics of a quantum mechanical resonator can show peculiar nonclassical features. For instance, counterintuitive correlation phenomena such as photon antibunching can occur, where the photon number correlation function for short delay times is smaller than the one for classical, uncorrelated photons. This implies that the probability for photons to arrive in pairs is suppressed.[2] Our approach provides a natural framework to investigate a possible non-Poissonian statistics of the multiphoton events in the nonlinear resonator. Therefore, we consider the normalized photon number correlation

function or second-order coherence function defined as[2]

$$g^{(2)}(\tau) = \frac{\langle a^\dagger(t)a^\dagger(t+\tau)a(t+\tau)a(t) \rangle_\infty}{\langle a^\dagger(t)a(t) \rangle_\infty \langle a^\dagger(t+\tau)a(t+\tau) \rangle_\infty}. \quad (3.27)$$

For long delay times τ , the counts of two photons with a delay time τ are statistically independent events, $g^{(2)}(\tau \rightarrow \infty) = 1$. For vanishing delay times, we have

$$g^{(2)}(\tau \rightarrow 0) = 1 + \frac{\langle \hat{n}^2 \rangle_\infty - \langle \hat{n} \rangle_\infty^2 - \langle \hat{n} \rangle_\infty}{\langle n \rangle_\infty^2}. \quad (3.28)$$

Photon antibunching corresponds to the case $g^{(2)}(\tau = 0) < 1$ [cf. App. A]. For the fully underdamped case, we find the expression

$$g^{(2)}(\tau = 0) = \frac{2N(N-1) + 4 \sum_1^{N-1} n(n-N)\rho_{nn}}{N^2} = 1 - \frac{1}{N}, \quad (3.29)$$

which represents the known result of the second-order correlation function of the electromagnetic field [2]. Hence, the oscillator displays photon antibunching close to a multiphoton transition. The second-order coherence of the stationary state of the quantum Duffing oscillator at the N -th multiphoton resonance has the same value as the second order coherence for an oscillator prepared in the single Fock state $|N\rangle$, in spite of its fluctuations over the quasienergy states.

3.3.3 Lineshape of the noise spectrum close to a multiphoton resonance

In presence of a small detuning from the multiphoton resonance, $\delta\omega - \delta\omega_N \sim \Omega_{0,N}$, the states $|\psi_0\rangle$ and $|\psi_N\rangle$ are no longer a resonant superposition of the Fock states $|0\rangle$ and $|N\rangle$. Hence, the corresponding stationary occupation probabilities ρ_{00} and ρ_{NN} , given in Eq. (3.16), become significantly different. In turn, the pair of peaks $S_0(\omega)$ and $S_N(\omega)$, which are associated to the transitions $|\psi_0\rangle \leftrightarrow |\psi_N\rangle$, become asymmetric such that $S_0(\omega) \neq S_N(-\omega)$. This behavior is shown in shown in Fig. 3.4(a) for the case around the 3-photon resonance. The peak lineshapes can readily been evaluated and we find

$$S_0(\omega) = \frac{2\Gamma_0\rho_{00}^\infty N^2 (\sin\theta \cos\theta)^2}{(\omega - \varepsilon_N + \varepsilon_0)^2 + \Gamma_0^2}, \quad S_N(\omega) = \frac{2\Gamma_N\rho_{NN}^\infty N^2 (\sin\theta \cos\theta)^2}{(\omega - \varepsilon_0 + \varepsilon_N)^2 + \Gamma_N^2}. \quad (3.30)$$

Their distance increases with the quasienergy splitting, $\varepsilon_N - \varepsilon_0 = \text{sgn}(\delta\omega - \delta\omega_N)(\Omega_{0,N}^2 + N^2|\delta\omega - \delta\omega_N|^2)^{1/2}$, whereas the peak width does not change close to the multiphoton resonance, $\delta\omega - \delta\omega_N \sim \Omega_{0,N}$. The asymmetry is determined by the stationary occupation probabilities ρ_{00}^∞ and ρ_{NN}^∞ . From Eq. (3.16), we find

$$\frac{S(\omega)}{S(-\omega)} = \frac{\rho_{00}^\infty}{\rho_{NN}^\infty} = \cot^4 \frac{\theta}{2} = \left[\frac{\Omega_{0,N}}{|\varepsilon_N - \varepsilon_0| - N(\delta\omega - \delta\omega_N)} \right]^4. \quad (3.31)$$

This expression is valid for ω close to the center of the largest peak, $\omega \sim \varepsilon_N - \varepsilon_0$, and $|\delta\omega - \delta\omega_N|$ not too large such that $S(\pm\omega) \gg \gamma$.

In addition to the peaks at finite frequencies (which induce decaying coherent multi-photon Rabi oscillations), also a zero frequency peak appears. This quasielastic peak is associated to incoherent relaxational decay of the multiphoton Rabi oscillations and is also known for the noise correlation function of a static biased quantum two level system [28].

In Fig. 3.3(b), we show the logarithm of the asymmetry ratio given in Eq. (3.31). The asymmetry shows a clear maximum at approximately $\varepsilon_3 - \varepsilon_0$.

To further illustrate the asymmetry in the peak heights, we show in Fig. 3.3(c) the peak maxima associated to the transitions $|\psi_0\rangle \rightarrow |\psi_3\rangle$ and $|\psi_3\rangle \rightarrow |\psi_0\rangle$. At the 3-photon resonance (black dashed vertical line), both peaks are equal in height (symmetric noise spectrum). Away from the resonance, the low (high) frequency branch acquires more spectral weight for negative (positive) detuning.

3.3.4 Photon noise at zero frequency

Fluctuations of an oscillator (quasi)energy induce a broad (with width $\propto \gamma$) zero frequency peak in the noise spectrum of an observable whose mean value depends on the (quasi)energy [73]. For weak driving $f \ll \nu$ and at a resonance $|\delta\omega - \delta\omega_N| \ll \Omega_{0,N}$, the quasienergy states of the Duffing oscillator have large fluctuations as several quasienergy states have comparable occupation probabilities even at $T = 0$. However, the mean value of \hat{n} becomes independent from the quasienergy, $\langle \psi_n | \hat{n} | \psi_n \rangle \approx N/2$ for $n \leq N$. As a consequence, the contribution to the noise spectrum of \hat{n} coming from fluctuations $\delta S(\omega)$ does not have a peak at zero frequency since $\delta S(0) \propto \gamma$. Close to resonance, when $|\delta\omega - \delta\omega_N| \sim \Omega_{0,N}$, two dynamical effects compete: on one hand, the quasienergy fluctuations quickly decrease for increasing detuning, i.e., moving away from resonance as the occupation probability of the state $|\psi_0\rangle$ approaches one. On the other hand, the mean value of \hat{n} becomes strongly dependent on the quasienergy. As a result of this competition, the intensity of the zero frequency noise plotted as a function of $\delta\omega$ has two maxima at the two opposite sides of the resonant value $\delta\omega_N$. In Fig. 3.4, we show the zero frequency noise for the special case $N = 2$. The yellow solid line represents the intensity at zero frequency computed numerically, while the green dashed line is the leading order contribution (in f/ν)

$$\delta S(\omega = 0) \approx \sin^2(2\theta)/4\gamma \quad (3.32)$$

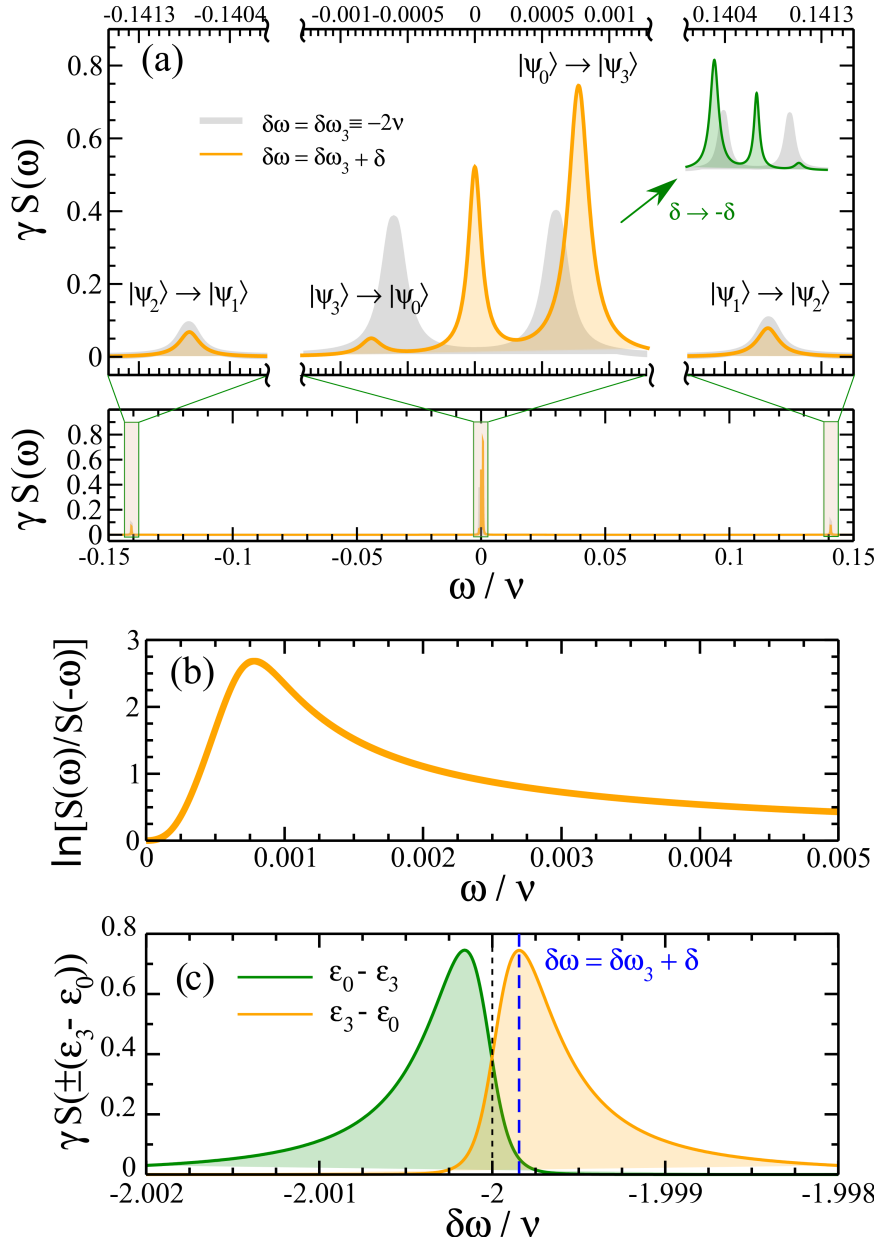


Figure 3.3: (a) Asymmetric structure of the photon noise spectrum at frequency $\delta\omega = \delta\omega_3 + \delta$, i.e., out of resonance for a detuning $\delta = 1.6 \times 10^{-4}\nu$ for the same parameters used in Fig. 3.2(b) (orange solid line). In addition, we show in the background the symmetric photon noise at the resonant frequency $\delta\omega_3$ (grey shadowed area). Moreover, we depict the inverted case $\delta \rightarrow -\delta$, which shows a symmetric behavior under the reflection $\omega \rightarrow -\omega$ (green solid line). (b) Noise asymmetry via the logarithm of Eq. (3.31) for the same parameters as in (a). (c) Height of the photon noise peak for the transition $|\psi_0\rangle \rightarrow |\psi_3\rangle$ (orange solid line), and $|\psi_3\rangle \rightarrow |\psi_0\rangle$ (green solid line) as a function of the external frequency. The peak maximum is located at $\delta\omega_3 \pm \delta$.

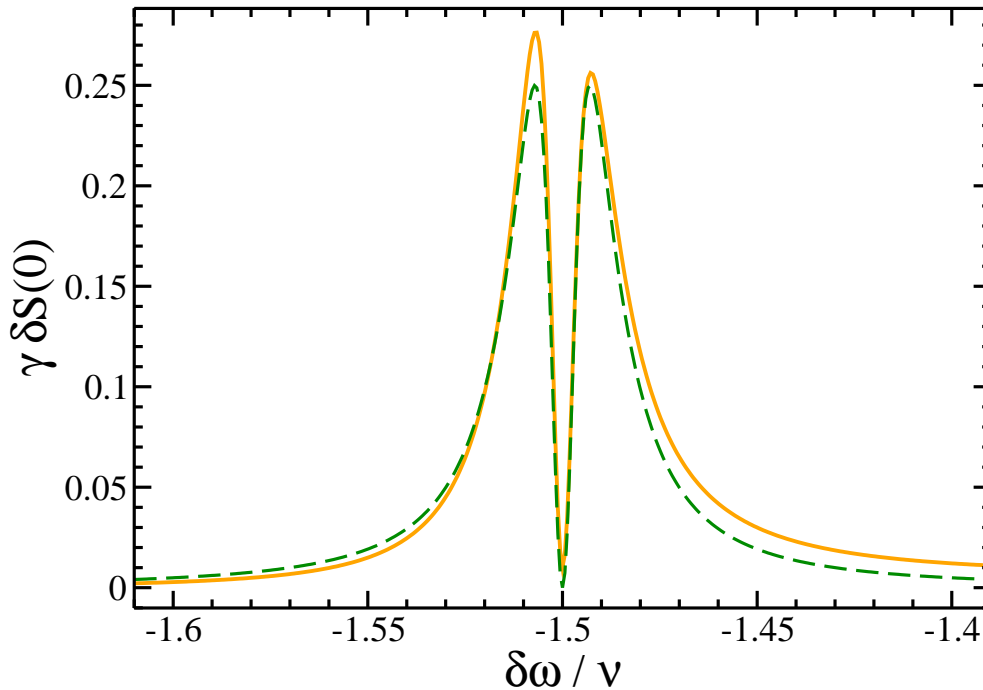


Figure 3.4: Photon noise at zero probe frequency as a function of the external frequency for the parameter set used in Fig. 3.2(a) evaluated around the second multiphoton resonance, $\delta\omega \sim -3\nu/2$. Shown is the comparison of the approach Eq. (3.32) as a green dashed line with the numerical simulation as an orange solid line.

3.3.5 Noise spectrum towards the semiclassical regime

Next, we investigate the noise spectrum for larger driving strengths, $f \lesssim \nu$. In order to illustrate how the noise spectrum changes for increasing driving, we show the intensities of the brightest peaks as a function of the driving strength for the $N = 5$ -photon resonance in Fig. 3.5(a). In Fig. 3.5(b), we also show the quasienergy spectrum, and the noise spectrum for a comparatively large value of the driving amplitude $f = \nu$ is shown in Fig. 3.5(c). A peak in the noise spectrum at frequency $\omega = \varepsilon_l - \varepsilon_k$ is associated to a single transition $|\psi_k\rangle \rightarrow |\psi_l\rangle$ and is given by

$$S(\omega) = \sum_{lk} \frac{2\rho_{ll}^\infty |\langle \psi_l | a^\dagger a | \psi_k \rangle|^2 (\gamma(a_l - a_k)^2 + \Gamma_l + \Gamma_k)}{(\omega + \varepsilon_l - \varepsilon_k)^2 + (\gamma(a_l - a_k)^2 + \Gamma_l + \Gamma_k)^2}. \quad (3.33)$$

Hence, the relative intensities of a pair of peaks at opposite frequencies is still related to the occupation probability of the corresponding initial states via $S(\varepsilon_l - \varepsilon_k)/S(\varepsilon_k - \varepsilon_l) = \rho_{kk}/\rho_{ll}$. For weak driving, we have three pairs of approximately symmetric peaks as described by Eq. (3.25). Each peak corresponds to a transition between two states belonging to a multiphoton doublet of quasidegenerate states: $|\psi_0\rangle \leftrightarrow |\psi_5\rangle$, $|\psi_1\rangle \leftrightarrow |\psi_4\rangle$, and $|\psi_2\rangle \leftrightarrow |\psi_3\rangle$. For increasing driving, the spectrum becomes increasingly asymmetric. For moderate values

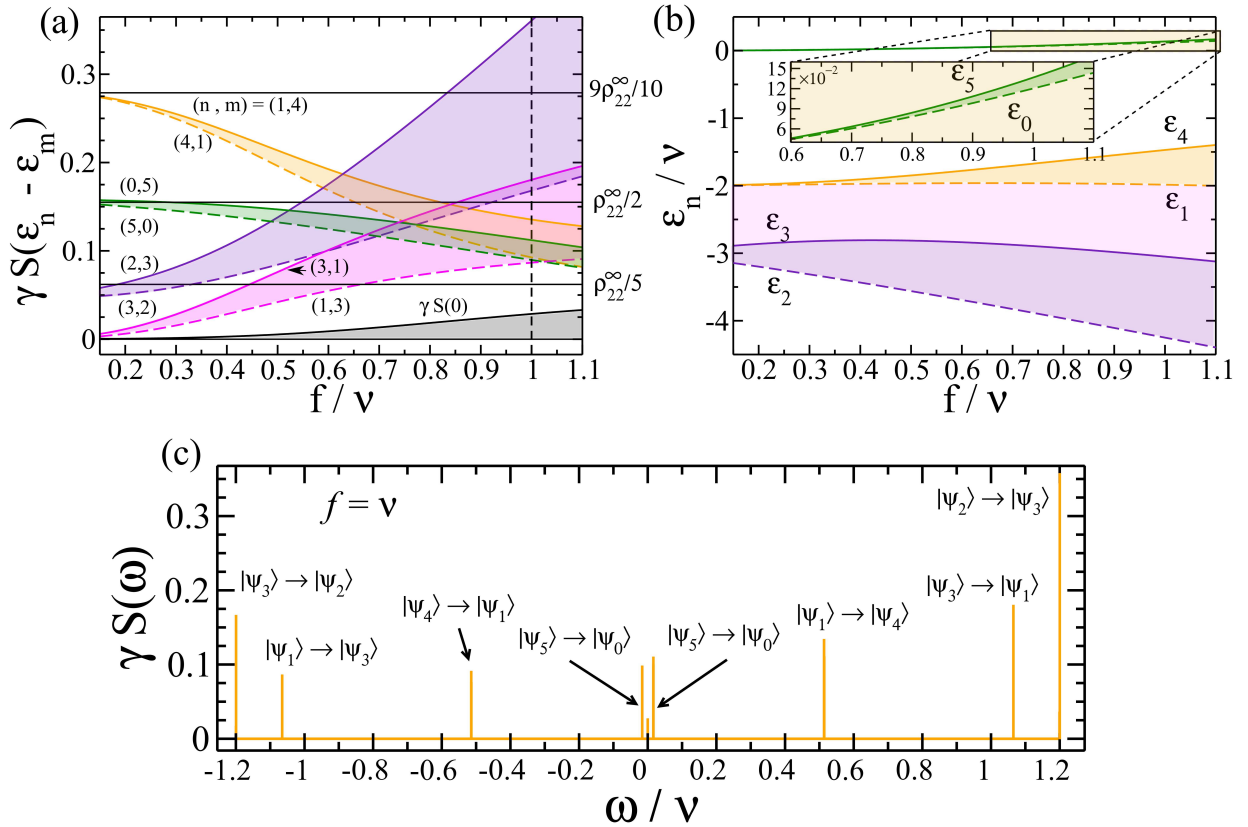


Figure 3.5: (a) Height of the photon noise peaks corresponding to the transitions within the pair $|\psi_n\rangle \leftrightarrow |\psi_m\rangle$ as a function of the driving strength f . Each pair is marked by a solid and a dashed line in the same color. In addition, we depict the rise of the zero frequency peak (black solid line) as the driving strength increases. The black horizontal lines indicate the expected values of the noise level evaluated up to leading order in f/ν by using Eq. (3.25). The parameters are $\nu = 10^{-3}\omega_0$, $\delta\omega = \delta\omega_5$. In panel (b), we show for the same parameters the quasienergy spectrum as a function of the driving strength f . In panel (c), the photon noise spectrum as a function of the probe frequency ω is shown for a large driving strength $f = \nu$.

of the driving, the noise spectrum undergoes two major qualitative changes: i) the peak at zero frequency becomes clearly visible; ii) a pair of peaks corresponding to the transitions $|\psi_1\rangle \leftrightarrow |\psi_3\rangle$ acquires a significant intensity. For $f = \nu$, the peak associated with the transition $|\psi_3\rangle \rightarrow |\psi_1\rangle$ is even the second brightest peak.

These qualitative changes can be explained in terms of a semiclassical description valid beyond the weak driving limit. The RWA Hamiltonian in Eq. (3.4) can be rewritten in terms of rotating quadratures, and interpreted as a quasienergy surface in phase space [74, 75]. It has the shape of a tilted Mexican hat and is sketched in Fig. 3.1(c) for two values of f . The larger f is, the stronger is the induced tilt. The local maximum and the minimum of the quasienergy surface are the classical attractors. In the static frame, they describe stationary

oscillations with a small and a large amplitude, respectively. In the vicinity of the attractors the vibration amplitude and the slow part of the oscillation phase display slow vibrations with frequency $\propto \delta\omega$. In absence of resonant transitions, each quasienergy state can be associated to a quantized quasiclassical orbit which lies on the internal surface around the local maximum, on the external surface, or along the quasienergy well around the minimum. For very weak driving, $f \ll \nu/\sqrt{2(N+1)}$, the quantum mechanical Fock states $|n\rangle$ with $n < N/2$ are associated to quasiclassical trajectories on the internal surface around the local maximum, whereas the Fock states with photon number n larger than $N/2$ are associated to semiclassical orbits on the external surface. Within this representation, the multiphoton transitions can then be reinterpreted as tunneling transitions between the internal and the external parts of the surface [74, 75]. For comparatively larger driving, the zero-point quasienergy associated to the slow vibrations around the minimum ($\propto \delta\omega$) becomes smaller than the dynamical barrier height. Then, quasienergy states appear which are localized in the quasienergy well. In turn, the noise spectrum becomes qualitatively different from the one for weak driving. The small quantum fluctuations around the minimum of the quasienergy surface can be described in terms of an effective auxiliary oscillator with ladder operators b and b^\dagger and are given by [cf. App. C]

$$a = a_h + b \cosh r_h^* - b^\dagger \sinh r_h^*. \quad (3.34)$$

Here, a_h is the amplitude of the stationary oscillations rescaled by $\sqrt{2}x_{\text{ZPF}}$ [67, 68]. They can be mimicked by a local effective quantum temperature $T_e = (2k_B \ln \coth r_h^*)^{-1}$ which depends on the squeezing factor r_h^* [60, 61, 67, 68]. For $f = \nu$, the states $|\psi_2\rangle$, $|\psi_3\rangle$, and $|\psi_1\rangle$ can be identified with the groundstate and first two excited states of the auxiliary oscillator (but in the remainder of this discussion we keep the same labels for the states as in the weak driving limit). The level spacing $\varepsilon_3 - \varepsilon_2$ is of the order of the frequency of the slow classical oscillations of the amplitude and slow part of the phase.

Such oscillations appear in the noise spectral density of a classical oscillator as a pair of peaks. In a nonlinear quantum oscillator whose quasienergy levels are not equidistant and their distance exceeds the damping strength, the classical peaks have a “quantum” fine structure [62]. In the present case of the Duffing oscillator, the classical noise peak is splitted into two peaks associated to the nearest neighbor transitions between the ground state and the first excited state, and the first and the second excited state, $|\psi_2\rangle \leftrightarrow |\psi_3\rangle$ and $|\psi_3\rangle \leftrightarrow |\psi_1\rangle$, respectively. Their peak height is proportional to the square of the rescaled vibration amplitude a_h and to the occupation of the initial state ρ_{nn}^∞ . The latter, in particular, is governed by the quantum temperature T_e . For the ratio of the peak heights, we find [62]

$$\frac{S(\varepsilon_3 - \varepsilon_2)}{S(\varepsilon_2 - \varepsilon_1)} \approx \frac{\rho_{22}^\infty}{\rho_{33}^\infty} \approx \coth^2 r_h^* \approx \frac{\rho_{33}^\infty}{\rho_{11}^\infty} \approx \frac{S(\varepsilon_1 - \varepsilon_3)}{S(\varepsilon_3 - \varepsilon_1)}. \quad (3.35)$$

Next nearest neighbor transitions can also yield peaks in the noise spectra of a Duffing oscillator [68]. In the present case, the transitions $|\psi_2\rangle \leftrightarrow |\psi_1\rangle$ yield a pair of dimmer peaks, however, located at frequencies outside the frequency range shown in Fig. 3.5.

In the weak damping, weak driving regime discussed so far, the quasienergy well around the minimum is still very shallow, and the oscillator can escape from the small amplitude attractor via tunneling. Therefore, the oscillator is not latched to any of the attractors and the noise spectral density has also peaks which are associated to intrawell transitions. In particular, the pair of peaks with the smallest splitting describes coherent tunneling oscillations between the internal and the external part of the quasienergy surface (coherent dynamical tunneling or multiphoton Rabi oscillations).

Before closing this section, we mention that for the stronger driving $f = \nu$, also a zero frequency peak appears in the noise spectrum, see Fig. 3.5(c), although the frequency detuning has been fixed to the 5-photon resonance $\delta\omega = \delta\omega_5$. However, as discussed above, this resonance condition is only valid for small $f \ll \nu$, which is obviously not fulfilled. So the larger driving induces an effective small detuning away from the exact avoided quasienergy level crossing and generates an effective bias. Then, a relaxation pole appears in the relevant self energy [28] which corresponds to a quasielastic relaxation peak at zero frequency.

3.3.6 Dependence of the noise spectrum on damping and temperature

So far, we have analyzed the case of zero temperature and small damping, $\bar{n} \ll 1$ and $\gamma \ll \Omega_{0,N}$. In this section, we briefly address how the noise spectrum is modified for larger damping and finite temperature by presenting numerical results of the spectrum in a broad parameter range.

In Fig. 3.6(a), we show $S(\omega)$ for different values of the damping for the 3-photon resonance where $\delta\omega = \delta\omega_3$. As expected, the peaks in the noise spectrum get broader for increasing damping. Outside the fully underdamped regime, the two peaks of the pair associated with the transitions $|\psi_0\rangle \leftrightarrow |\psi_3\rangle$ start to overlap and eventually merge into a single peak at zero frequency. Thereby, the zero frequency noise is no longer suppressed $S(\omega \approx 0) \propto \gamma^{-1}$, since incoherent relaxation prevails over coherent decay for large damping. The peaks associated with the underdamped transitions $|\psi_1\rangle \leftrightarrow |\psi_2\rangle$ are still described by Eq. (3.25), even when the spectrum has a peak at zero frequency. The decrease in the peak

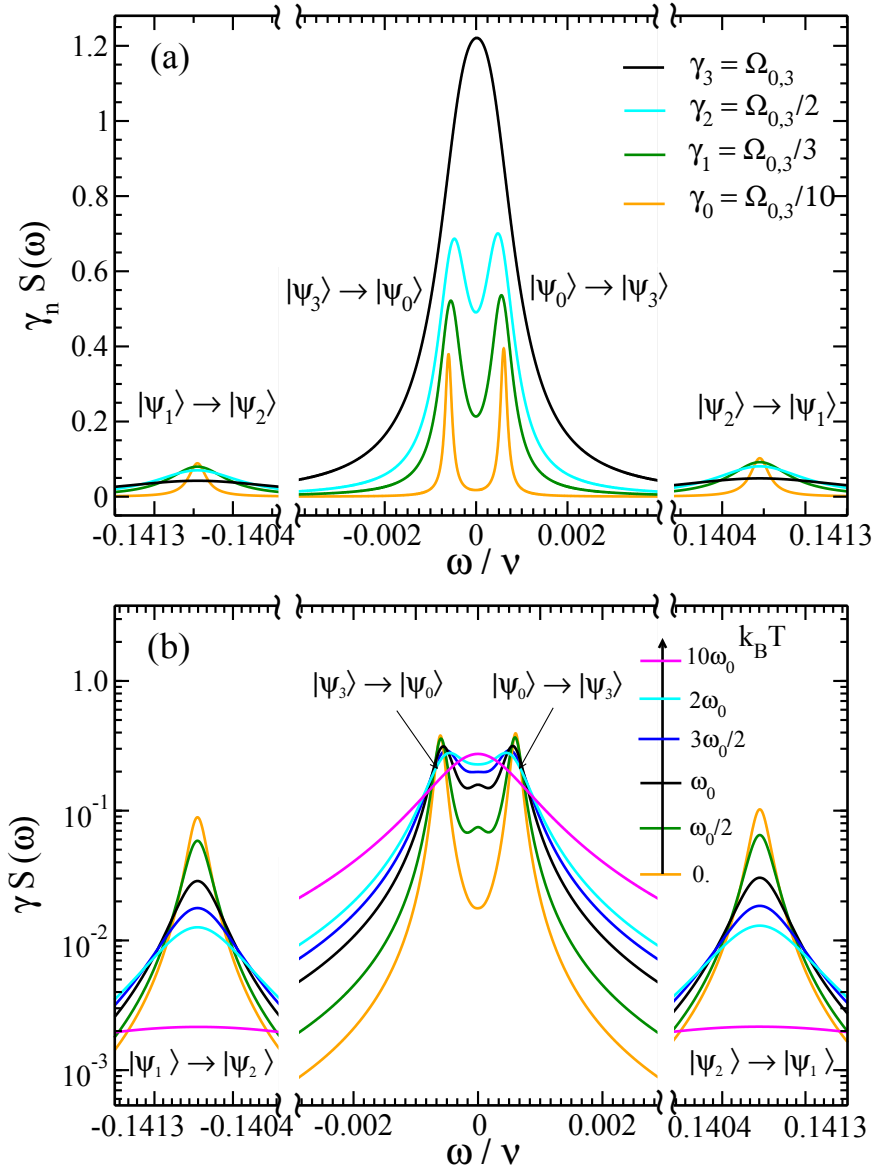


Figure 3.6: Photon noise at the 3-photon resonance, $\delta\omega = \delta\omega_3$, as a function of the probe frequency. In panel (a), we show the behavior when going from the coherent to the incoherent regime by increasing the damping constant from $\gamma_0 \ll \Omega_{0,3}$ to $\gamma_3 = \Omega_{0,3}$ (at $T = 0$). In panel (b), we fix the damping constant to $\gamma = \Omega_{0,3}/10$ and show the noise temperatures increasing from zero ($T = 0$) up to finite temperatures ($T \gg \omega_0$). The remaining parameters are $\nu = 10^{-3}\omega_0$ and $f = \nu/10$.

intensities reflects the decrease of the populations ρ_{11}^∞ and ρ_{22}^∞ in the partially underdamped regime.

The dependence of the noise spectrum on temperature is shown in Fig. 3.6(b) and behaves qualitatively similarly. For small temperatures $\bar{n} \ll 1$, the spectrum is described by Eq. (3.25). The temperature dependence enters in the line widths of the quasienergy levels as well as in the stationary distribution ρ_{nn}^∞ . For larger temperatures, the two low-frequency peaks merge into a single peak at zero frequency and the side peaks becomes increasing broader as expected.

3.4 Conclusions

In recent years, the rich phenomenology of driven and damped nonlinear quantum oscillators has been impressively consolidated, including their nonlinear response behavior in form of resonant and antiresonant amplification, quantum coherent multiphoton Rabi oscillations, quantum activation and quantum heating. Gradually, the nontrivial effects visible in noise correlation functions have also moved to the focus of interest. Those become relevant whenever a nonlinear quantum oscillator is used as a central element in an amplifier or quantum measurement device. In this Chapter, we have analyzed the noise properties of the quantum Duffing oscillator in the regime when only few quanta are excited. Then, the nonlinear response shows pronounced multiphoton peaks which are associated to resonant multiphoton Rabi oscillations. The noise properties of these multiphoton transitions show a rich phenomenology. To obtain the noise spectrum by analytical means, we invoke the Lax formula for the autocorrelation function of the photon number at different times and calculate its Fourier transform. Exactly at a multiphoton resonance, the noise spectrum consists of a collection of pairs of related resonances which are located at opposite frequencies and which are equal in height. Each pair is associated to a multiphoton doublet. In spite of large fluctuations over the oscillator quasienergy, no quasielastic peak occurs at zero frequency. This is a consequence of a special symmetry of the quantum Duffing oscillator: all quasienergy states which are associated to a multiphoton doublet have the same mean value of the photon number \hat{n} .

Slightly away from a multiphoton resonance, the noise spectrum becomes asymmetric and the two resonances are no longer equal in height. In addition, as the mean values of \hat{n} become different for quasienergy states with comparable occupations, the quasielastic peak emerges. Since the quasienergy fluctuations are suppressed away from a multiphoton resonance, the intensity of the quasielastic peak as a function of the detuning displays a maximum at the two opposite sides of the resonant value $\delta\omega_N$.

Our approach also allows us to evaluate the transition to the semiclassical regime by

increasing the photon number by a larger driving amplitude. Then, a quasiclassical quasipotential landscape in phase space is a convenient tool to understand the stationary nonequilibrium dynamics. This view directly leads to quantum mechanical squeezed states which exist close to the local minimum of the quasienergy landscape. A harmonic expansion allows us to characterize the quantum fluctuations via an effective quantum temperature. At larger (real) temperature and damping strengths, all these quantum coherent features are washed out.

Although the time-resolved detection of noise properties of quantum observables of driven resonators requires considerably more experimental effort, we are confident that future experiments will soon elucidate the importance of quantum noise in these nonequilibrium systems.

Qubit state detection using the quantum Duffing oscillator

The efficient and reliable detection of the quantum mechanical state of a nanoscale system is a key component of all present designs of quantum circuits.[13] One nondestructive readout scheme currently in use for the important class of superconducting flux qubits is based on a heterodyne detection of the dynamic response of a dc superconducting quantum interference device (dc-SQUID) detector which is inductively coupled to the qubit.[76, 77] Thereby, the dc-SQUID is operated in its linear regime as a shunted variable inductor in a resonant circuit. In this set-up, its resonance frequency depends on the magnetic flux generated by the qubit being in the ground or excited state. Hence, measuring the impedance of the resonant circuit as a function of an externally applied bias current yields two characteristic Lorentzian resonances at two different resonance frequencies, which depend on the two qubit states. This detection scheme, hence, allows us to infer the state of the qubit from the resonant response of the detector in the nanocircuit. In order that a reliable discrimination of the two qubit states becomes possible in this continuous type of readout design, the probability distributions for the readout values have to be only weakly overlapping. Due to thermal and quantum fluctuations, the readout naturally is a random process,[77] and the noise properties of the nanocircuit around the detector resonances determine the discrimination power of the set-up.

An alternative readout scheme is the Josephson bifurcation amplifier.[17, 18] It is based on a classical driven nonlinear resonator and exploits the classical bifurcation point of the dynamically induced bistability with a small- and a large-oscillation state.[78] The response (or output) of the nonlinear resonator around the bifurcation point is very sensitive to small changes in the circuit parameters. This is an ideal prerequisite for a sensitive detector. Depending on the state of the qubit to be sensed, the resonator bifurcation point

is shifted to a different frequency, allowing for large discrimination powers between the large- and small-oscillation detector state of up to 98%.^[79] Nevertheless, since the detector is a classical macroscopic device, it introduces considerable dephasing and relaxation to the qubit state, yielding a reduced contrast of the qubit Rabi oscillations of less than 90%.^[79] This implies that the thermal noise properties of the nonlinear detector (together with semiclassical corrections due to quantum fluctuations) around the classical bifurcation point determine the discrimination power between the two states close to the classical bifurcation point.^[63, 74, 80, 81] Hence, it would be desirable to combine the advantage of a large discrimination power of a nonlinear detector with the reduced noise sensitivity of a nanocircuit operated close to the quantum regime.

An experimental realization of a driven nonlinear resonator in its few-photon quantum regime is in principle possible with present set-ups and technology. In a recent experiment,^[82] a nanoscale superconducting microwave resonator has been driven to its nonlinear regime by fast frequency-chirped voltage pulses. At low enough temperature, the regime of quantum noise has been reached. In this experiment, the applied driving strength has been rather large, which corresponds to a large photon number transferred to the resonator. No particular few-photon resonances have been revealed and the nonlinear response is similar to previous schemes on classical bifurcation detectors using a time-dependent driving frequency.^[83] However, the route to the few-photon regime seems to be clear.

In this chapter, we introduce a combination of both strategies, *bifurcation* and *dispersive* readout, and propose a nonlinear detector scheme in the form of a nonlinear resonator with an amplitude modulated drive in its few-photon deep quantum regime. In particular, in this regime, we shall exploit sharp multiphoton resonances in the nonlinear resonator, ^[47, 48, 71] which are induced by the external driving field close to the fundamental resonator frequency [cf. Chapter 3]. They can be used for the detection of the states of the qubit and offer the advantage of being rather sharp and externally tunable by varying the parameters of the external drive. The concept is an extension of the case of a linear resonator, where the fundamental resonance frequency is shifted depending on the qubit state. However, the multiphoton resonances in the nonlinear detector close to the detector's fundamental frequency show very small line widths. The width of the N -photon resonance is determined by the corresponding N -photon Rabi frequency, which decreases with increasing photon number. The sharp resonance lines, in turn, offer the advantage that only a few measurement cycles are necessary to ensure a large discrimination power. To understand the back action of the nonlinear multiphoton detector on the qubit state, we determine the relaxation rate of the qubit due to the coupling to the driven dissipative nonlinear oscillator around a multiphoton resonance. Notably, the back action of the

resonator on the qubit is sufficiently weak, yielding to a good qubit-state measurement fidelity. Furthermore, we show that the discrimination power of the set-up is rather large and beyond 98% for our choice of realistic parameters of a flux qubit circuit. In fact, it gives rise to an enhanced measurement fidelity as compared to the linear parametric oscillator. Furthermore, we show that the nonlinear multiphoton detector does not have a worse measurement efficiency as compared to the linear detector scheme. We determine the measurement efficiency of the set-up via the ratio of the time it takes to collect enough information on the qubit state (measurement time) and the relaxation time. It turns out that the measurement efficiency does not considerably decrease as compared to the linear case. Hence, the detection scheme indeed has the advantage of an overall reduced back action in combination with an enhanced discrimination power, together with a sufficiently large measurement efficiency. The contents of this Chapter have been published in Ref. 69.

4.1 Persistent current qubit

We consider the experimental set-up used in Ref. 84 for the qubit, consisting of a superconducting loop interrupted by three Josephson junctions, two of which have equal Josephson energies, while the coupling energy of the third is smaller, in order to yield a double-well potential configuration. In this low-inductance circuit, the flux through the loop remains close to the externally applied value Φ_{qb} . When the latter is close to $(n + 1/2)\Phi_0$, where $n \in \mathbb{Z}$ and Φ_0 is the flux quantum, the device is described by the Hamiltonian in terms of the Pauli matrices $\sigma_{x,z}$ as

$$H_{\text{qb}} = \epsilon \sigma_z / 2 - \Delta \sigma_x / 2, \quad (4.1)$$

with the two eigenstates $|\uparrow\rangle$ and $|\downarrow\rangle$ of σ_z corresponding to the two persistent current states $\pm I_p$. The minimal energy level splitting Δ and the current I_p are determined by the charging and Josephson energies of the Josephson junctions. The asymmetry is given by $\epsilon = 2I_p(\Phi_{\text{qb}} - \Phi_0/2)$. In the energy eigenbasis, the Hamiltonian follows as

$$H_{\text{qb}} = \omega_{\text{qb}} \tau_z / 2, \quad (4.2)$$

where $\omega_{\text{qb}} = \sqrt{\epsilon^2 + \Delta^2}$ is the proper frequency of the qubit, and $\tau_z = \sigma_z \cos \theta - \sigma_x \sin \theta$ the corresponding Pauli matrix with $\tan \theta = \Delta/\epsilon$. The detection of the qubit state essentially involves the measurement of the magnetic flux produced by the persistent current states. To this end, one can use the driven SQUID as a sensitive magnetometer, [76] operating in its nonlinear region. Below, we will restrict to the few-photon deep quantum regime.

4.2 Driven SQUID as a nonlinear quantum detector

We consider the standard setup of a dc-SQUID formed by two Josephson junctions in a superconducting loop, but subject to a time-dependent external bias current.[17] Moreover, we assume a negligible ring inductance L_R of the SQUID (low-inductance approximation). [85] In this configuration, the superconducting phase differences at each junction, χ_1 and χ_2 , play the role of dynamical variables with a constraint given by the flux quantization, i.e., $\chi_1 - \chi_2 = -\Phi_{\text{sq}}/\varphi_0 \equiv -2\pi\varphi_{\text{ex}}$, where Φ_{sq} is the external magnetic flux piercing the superconducting loop and $\varphi_0 = \Phi_0/2\pi$. Note that within the low-inductance approximation, $L_R I_{0c} \ll \varphi_0$ with the critical current I_{0c} of the SQUID. Thus, the system is described by the generalized coordinate $\chi_+ = (\chi_1 + \chi_2)/2$, with the effective Lagrangian [86]

$$L_{\text{sq}}(\chi_+, \dot{\chi}_+, t) = \varphi_0^2 C_0 \dot{\chi}_+^2 + E_J \cos(\pi\varphi_{\text{ex}}) \cos(\chi_+) - \varphi_0 I_b(t) \chi_+, \quad (4.3)$$

where we have assumed a symmetric loop, with $E_J = \varphi_0 I_{0c}$ as the Josephson energy, and C_0 as the capacitance of each junction. Moreover, we include a time-periodic ac current $I_b(t) = I_0 \cos(\omega_{\text{ex}} t)$ with frequency ω_{ex} and amplitude I_0 injected “into” the loop. The above Lagrangian describes an effective superconducting loop (with a negligible ring inductance) with a single Josephson junction [77] with a tunable Josephson energy $E_J \cos(\pi\varphi_{\text{ex}})$, critical current $I_c = 2I_{0c} |\cos \pi\varphi_{\text{ex}}|$, cross-junction phase difference χ_+ , and capacitance $C = 2C_0$. In order to tune the resonance frequency, the SQUID is shunted [17] with a capacitance $C_s \gg C$. Next, we shall establish the optimal working point of the qubit-detector system, where the dissipative influence entering via the detector is minimal.

4.2.1 Qubit-detector interaction

The qubit and the SQUID are coupled by means of their mutual inductance M . [9, 77] Thereby, the SQUID induces the flux MI_{S} in the qubit loop, where I_{S} is the circulating current in the SQUID. The latter can be determined by using current conservation in the loop and the Josephson relations for the two junctions in the SQUID. For the symmetric SQUID, [77] it follows that $I_{\text{S}}(t) = I_{c0} \sin(\pi\varphi_{\text{ex}}) \cos(\chi_+(t))$. Thus, the total magnetic flux in the qubit is affected by its coupling with the SQUID, and it is composed of the external flux and the SQUID-generated contribution, i.e., $\Phi_{\text{qb}} \rightarrow \Phi_{\text{qb}} + MI_{\text{S}}(t)$. This implies that the energy bias of the qubit acquires a contribution that depends on the circulating current in the SQUID, leading to the effective asymmetry $\epsilon_f = \epsilon(\Phi_{\text{qb}}) + \beta(I_{\text{S}}(t))$, where $\beta(I_{\text{S}}(t)) = 2MI_p I_{\text{S}}(t)$.

Therefore, two sources of noise can affect the qubit dynamics, i.e., the fluctuations from the external flux Φ_{qb} and from the bias current $I_b(t)$ in the SQUID, [87] which is related to χ_+ by the Josephson equation $I_b(t) = I_{c0} \sin(\chi_+(t))$. By tuning the bias current

to the critical value I_b^* characterized by $(d\beta/dI_b)_{I_b=I_b^*} = 0$, the influence from current fluctuations in the SQUID can be minimized [87] and the optimal working point is reached. For a nonsymmetric SQUID, the lowest-order contribution is linear in I_b , [86, 87] while in the symmetric case this lowest-order contribution vanishes, which implies that around the optimal working point the phase χ_+ is very small, $\chi_+ \sim 0$. In the following, we consider a setup close to the optimal point, where we can expand the expression for I_\odot up to second order in χ_+ , yielding the interaction term

$$H_{\text{qb-sq}} = \tilde{g}\chi_+^2\sigma_z, \quad (4.4)$$

with the coupling constant $\tilde{g} = 2I_p I_{0c} M \sin(\pi\varphi_{\text{ex}})$.

4.2.2 SQUID modelled as a Duffing oscillator

As we operate the detector in its nonlinear regime, we expand the potential term in Eq. (4.3) around the optimal point up to fourth order in χ_+

$$V(\chi_+) = -E_J \cos(\pi\varphi_{\text{ex}}) \cos(\chi_+) \simeq V_0 + m\omega_0^2\chi_+^2/2 - \tilde{\alpha}\chi_+^4, \quad (4.5)$$

where $m = \varphi_0^2 C_s$ is the effective mass, $\omega_0 = (I_c/\varphi_0 C_s)^{1/2}$ the corresponding frequency, and $\tilde{\alpha} = m\omega_0^2/4$ the strength of the nonlinearity. We switch to a description in terms of creation and annihilation operators a and a^\dagger , defined by $\chi_+ = \chi_0(a + a^\dagger)/\sqrt{2}$ with $\chi_{ZPF} = \sqrt{1/(m\omega_0)}$ being the zero-point fluctuations of the phase χ_+ . Adding the time-dependent driving term yields us to the Hamiltonian of the driven SQUID described by the quantum Duffing oscillator model

$$H_{\text{sq}} = \omega_0 a^\dagger a - \nu(a + a^\dagger)^4/12 + f(a + a^\dagger) \cos(\omega_{\text{ex}}t), \quad (4.6)$$

with nonlinearity and driving strength given by $\nu = 3I_c\varphi_0\chi_{ZPF}^4/4$ and $f = I_0\varphi_0\chi_{ZPF}/\sqrt{2}$, respectively. Similarly, the interaction Hamiltonian in terms of ladder operators reads

$$H_{\text{qb-sq}} = g(a + a^\dagger)^2\sigma_z/2, \quad \text{with } g = \tilde{g}\chi_{ZPF}^2 \quad (4.7)$$

Notice that g and ν depend on the external flux φ_{ex} , i.e., they are tunable in a limited regime with respect to the desired oscillator frequency ω_0 , where the coupling term is considered as a perturbation to the SQUID ($g < \nu$), in order to keep the dynamics of the oscillator to dominate. The dependence of the dimensionless ratios ν/ω_0 and g/ω_0 is shown in Fig. 4.1. We restrict to parameters of the external magnetic flux in the SQUID loop, which generate a weak nonlinearity and a weak qubit-detector coupling strength, $\{\nu, g\} \ll \omega_0$, i.e., for $\varphi_{\text{ex}} \sim 0$. A typical dependence of both parameters for typical experimental parameters

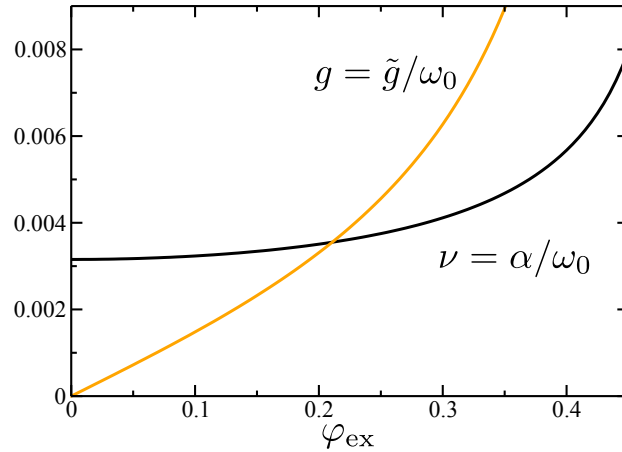


Figure 4.1: Dependence of the dimensionless ratios ν/ω_0 and g/ω_0 on the external flux φ_{ex} in the SQUID. The parameters of the SQUID are chosen as $C_s = 7.65$ pF, $I_{c0} = 200$ nA, $I_p = 300$ nA, and $M = 40$ pH. [77]

is shown in Fig. 4.1. Both cases of $g > \nu$ and $g < \nu$ can be achieved. For our purpose of a qubit-detector setup, the qubit-resonator coupling typically will be required as small enough in order to ensure a minimal back action. On the other hand, the qubit-detector coupling should be large enough so that an efficient detection of the qubit state becomes possible. As is shown in Fig. 4.1 and will be quantitatively discussed in the sequel of this Chapter, this can indeed be achieved for realistic parameters. Moreover, the choice of the parameter regime also justifies us to restrict the influence of the resonator coupling on the effective qubit bias to lowest order in χ_+ only. Eventually, the total system is described by the Hamiltonian $H(t) = H_{\text{qb}} + H_{\text{qb-sq}} + H_{\text{sq}}(t)$.

4.3 Coherent dynamics and rotating-wave approximation

Before we address the dynamics of the detection scheme based on the nonlinear response of the Duffing oscillator to the applied periodic driving in the stationary regime, we discuss the coherent dynamics generated by $H(t)$, which is periodic in time.

Here, we are interested in exploiting few-photon transitions in the detector around the fundamental detector frequency ω_0 . Hence, higher harmonics have a small amplitude and can effectively be neglected. Furthermore, we focus on the regime of weak nonlinearity, weak driving, and weak qubit-detector coupling as characterized by $\{\nu, f, g\} \ll \omega_0$. The proposed mechanism of detection is most conveniently discussed in the simplest case, when the dynamics occurs close to the fundamental oscillator resonance $\omega_{\text{ex}} \sim \omega_0 \sim \omega_{\text{qb}}/2$.

Then, the rotating-wave approximation (RWA) can be invoked in order to obtain a simple interpretation in terms of few-photon transitions. In passing, we note that we have also performed a complete analysis in terms of full Floquet theory, thereby avoiding the RWA. For all cases shown below, both approaches yield coinciding results.

We switch to the rotating reference frame by the transformation $R(t) = \exp\{i(a^\dagger a + \tau_z)\omega_{\text{ex}}t\}$. Then, the RWA eliminates the fast oscillating terms from the transformed Hamiltonian $\mathcal{H} = R(t)H(t)R^\dagger(t) - iR(t)\dot{R}^\dagger(t)$ and the time-independent Schrödinger equation in the rotating frame $\mathcal{H}|\varphi_\alpha\rangle = \varepsilon_\alpha|\varphi_\alpha\rangle$ follows, with the RWA Hamiltonian given by

$$\mathcal{H} = \mathcal{H}_{\text{qb}} + \mathcal{H}_{\text{qb-sq}} + \mathcal{H}_{\text{sq}}, \quad (4.8)$$

with

$$\begin{aligned} \mathcal{H}_{\text{qb}} &= \frac{1}{2}\delta\omega_{\text{qb}}\tau_z, \\ \mathcal{H}_{\text{qb-sq}} &= g \cos \theta a^\dagger a \tau_z + \frac{g}{2} \sin \theta (a^{\dagger 2}\tau^- + a^2\tau^+), \\ \mathcal{H}_{\text{sq}} &= \delta\omega a^\dagger a - \frac{\nu}{2}a^\dagger a a a^\dagger + \frac{f}{2}(a + a^\dagger). \end{aligned}$$

The detuning frequencies follow as $\delta\omega = \omega_0 - \omega_{\text{ex}}$ and $\delta\omega_{\text{qb}} = \omega_{\text{qb}} - 2\omega_{\text{ex}}$, and $\tau^\pm = (\tau_x \pm i\tau_y)/2$. The quasienergies ε_α and the RWA eigenstates $|\varphi_\alpha\rangle$ result from a straightforward numerical diagonalization of \mathcal{H} . In the static frame, an orthogonal (at equal times) set $\{|\tilde{\varphi}_\alpha(t)\rangle\}$ of an approximate solution of the Schrödinger equation follows as

$$|\tilde{\varphi}_\alpha(t)\rangle \simeq e^{-i\varepsilon_\alpha t}|\phi_\alpha(t)\rangle = e^{-i\varepsilon_\alpha t}e^{-i(a^\dagger a + \tau_z)\omega_{\text{ex}}t}|\varphi_\alpha\rangle. \quad (4.9)$$

Here, the quasienergy states $|\phi_\alpha(t)\rangle \equiv e^{-i(a^\dagger a + \tau_z)\omega_{\text{ex}}t}|\varphi_\alpha\rangle$ are time periodic with period $2\pi/\omega_{\text{ex}}$ and form a complete basis that will be used below for the description of the dissipative dynamics. We note that an analytic expression for the multi-photon resonances would follow from a Van-Vleck perturbative approach in a similar manner as for the pure quantum Duffing oscillator.[47, 48] However, the resulting expression will be cumbersome and not further illuminating for the present purpose. We note, furthermore, that the qubit-detector interaction occurs via a parametric coupling $g \cos \theta a^\dagger a \tau_z$, and via a two-photon coupling $g \sin \theta (a^{\dagger 2}\tau^- + a^2\tau^+)/2$.

4.4 Detection in the few photon regime

4.5 Dissipative dynamics

The electronic nanocircuit is embedded in a dissipative environment. In particular, the SQUID is shunted with an Ohmic resistor, which yields dissipative fluctuations $\xi(t)$. [28]

We focus to the case of an underdamped SQUID, where the shunt resistance is large, [9, 17] and use the standard harmonic bath in order to model the fluctuations, which are rooted in current fluctuations and can be encoded in the Ohmic spectral density $J(\omega) = \gamma\omega$. [28] They couple to the resonator's dipole operator, i.e., $H_\xi = \chi_+\xi(t)$. Thus, the time evolution of the reduced density operator $\rho(t)$ is described in terms of the master equation Eq. (2.50). We note that, in the same way, the direct coupling of the qubit to the electromagnetic fluctuations could be included. However, we have checked [60] that for a related set-up of a flux qubit coupled to a harmonic oscillator, such a direct dissipation of the qubit yields only minor quantitative corrections, which should be included in a quantitative description of an experiment, [87] but do not add qualitatively new physics.

In order to measure the dynamic response of the resonator to the external drive at asymptotically long times, a heterodyne detection scheme such as in Ref. 72 can be used, [77] where the coupled qubit-oscillator system approaches the steady state ρ^∞ . In this regime, we compute the nonlinear response of the detector, characterized by the mean value $\langle\chi_+\rangle_\infty(t)$ at asymptotic times (where $\langle\cdots\rangle_\infty = \text{Tr}[(\cdots)\rho^\infty]$). As we restrict the discussion to the regime close to the first harmonic (small detuning), higher harmonics can be neglected and we immediately obtain

$$\langle\chi_+\rangle_\infty(t) = \sum_{kl} \rho_{kl}^\infty (a_{lk}^\dagger \exp[i\omega_{\text{ex}}t] + a_{lk} \exp[-i\omega_{\text{ex}}t]). \quad (4.10)$$

As the system is driven with frequency ω_{ex} , $\langle\chi_+\rangle_\infty(t)$ also oscillates with time. Its amplitude is given by

$$A = \sum_{kl} \rho_{kl} (a_{lk}^\dagger + a_{lk}). \quad (4.11)$$

Correspondingly, we evaluate the population difference $\langle\sigma_z\rangle_\infty(t)$ of the qubit states and obtain

$$\langle\sigma_z\rangle_\infty(t) = \sin\theta \sum_{kl} \varrho_{kl}^\infty (\tau_{lk}^+ \exp[2i\omega_{\text{ex}}t] + \tau_{lk}^- \exp[-2i\omega_{\text{ex}}t]) + \cos\theta \sum_{kl} \rho_{kl}^\infty \tau_{lk}^z, \quad (4.12)$$

where $\tau_{lk}^z = \langle\varphi_l|\tau_z|\varphi_k\rangle$ and $\tau_{lk}^\pm = \langle\varphi_l|\tau^\pm|\varphi_k\rangle$. The population difference oscillates, with a maximal value given by

$$P_\infty = \sum_{kl} \rho_{kl} (\tau_{lk}^z \cos\theta + \tau_{lk}^x \sin\theta). \quad (4.13)$$

4.5.1 Detector response for weak coupling to the qubit

Consider a finite coupling of the detector to the qubit whose state is to be sensed, i.e., $g \neq 0$. The coupling inevitably induces relaxation and decoherence in the qubit, characterized by the relaxation and dephasing rate, Γ and Γ_d , respectively. Typically, the detector couples

only weakly to the system, i.e., $g \ll \omega_{\text{qb}}$. Then, the associated relaxation and dephasing times (T_1 and T_2 , respectively) are still much larger than the corresponding relaxation time scale for the detector given by $1/\gamma$. In passing, we note that the corresponding relaxation time around a *resonant* multiphoton transition (in the underdamped case) has been shown in Refs. 71,48 to be comparable to γ . Moreover, we bias the qubit with a large asymmetry, $\epsilon \gg \Delta$ in order to “gauge” the detector response.

For a rough evaluation of the order of magnitude of the involved time scales, we may neglect the nonlinearity of the detector ($\nu = 0$) for the moment and estimate the effective relaxation rate for the qubit coupled to an Ohmically damped harmonic oscillator.[88] This model can be mapped to a qubit coupled to a structured harmonic environment with an effective (dimensionless) coupling constant $\kappa_{\text{eff}} = 8\gamma g^2/\omega_0^2$. For the realistic parameters used in Fig. 4.1 and $g = 1.2 \times 10^{-3}\omega_0$, we find that $\kappa_{\text{eff}} \simeq 10^{-10}$, giving rise to an estimated relaxation rate [28, 88] $\Gamma_{\text{harm}} \simeq (\pi/2) \sin^2(\theta) \kappa_{\text{eff}} \epsilon \simeq 10^{-13}\omega_0$ (evaluated at low temperature). Hence, this illustrates that we can easily achieve the situation where $\Gamma_{\text{harm}} \ll \gamma$ required for this detection scheme. Then, for a waiting time (after which we start the measurement) much longer than the relaxation time γ^{-1} of the nonlinear oscillator, but still smaller than Γ^{-1} , the oscillator is able to reliably detect the qubit state. In fact, under these conditions, the state of the qubit, apart from the inevitable dephasing, remains unaffected in a time window before it reaches its global stationary state and an effective shift of the oscillator’s eigenfrequency arises due to the parametric coupling term $\sim g \cos \theta n \tau_z$ in Eq. (4.8). Treating the qubit-detector interaction term in Eq. (4.7) perturbatively to lowest order in g , the eigenfrequency shift follows straightforwardly as

$$\omega_0 \rightarrow \omega_0 + g \langle \sigma_z \rangle .$$

Thus, the nonlinear response is shifted by $-g$ ($+g$) if the qubit is prepared in the state $\langle \sigma_z \rangle = -1$ ($\langle \sigma_z \rangle = +1$). This is illustrated in Fig. 4.2, in which we show the nonlinear response of the resonator for the uncoupled (blue dashed line) and the coupled (black solid line) case. For a fixed value of g , the shift between the two cases of the opposite qubit states is given by the frequency gap $\delta\omega_{\text{ex}} \simeq 2g$. Figure 4.3(a) shows the nonlinear response of the detector for the two cases when the qubit is prepared in one of its eigenstates: $|\uparrow\rangle$ (orange solid line) and $|\downarrow\rangle$ (black dashed line).

An important feature of a detection scheme is that it is efficient in discriminating the states to be detected. This can be quantified by the discrimination power of the detector, which can be defined for our case as[76]

$$D(\omega_{\text{ex}}) = |A_{|\uparrow\rangle}(\omega_{\text{ex}}) - A_{|\downarrow\rangle}(\omega_{\text{ex}})| . \quad (4.14)$$

The result for $D(\omega_{\text{ex}})$ is shown in Fig. 4.3 (b). The discrimination power shows a rich structure of local maxima and minima, which indicates that it can be tuned directly by

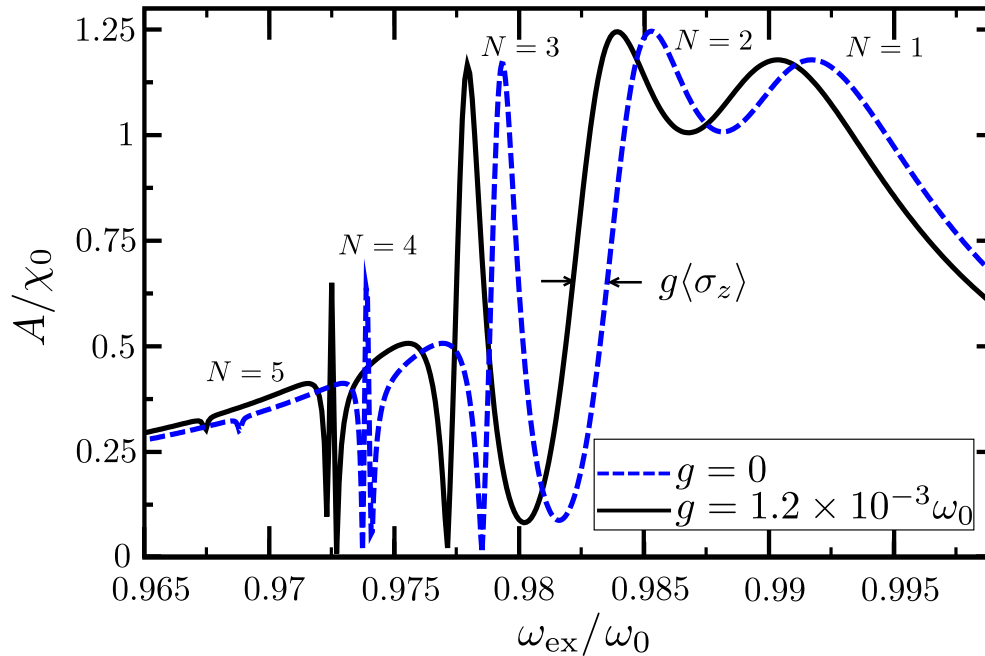


Figure 4.2: Nonlinear response A of the detector as a function of the external driving frequency ω_{ex} in the presence of a finite coupling $g = 0.0012\omega_0$ to the qubit (black solid line). The blue dashed line indicates the response of the isolated detector. The parameters are $\nu = 0.01\omega_0$, $f = 0.006\omega_0$, $T = 0.006\omega_0$, $\gamma = 1.6 \times 10^{-4}\omega_0$, and $\epsilon = 2.2\omega_0$ and $\Delta = 0.05\omega_0$, in correspondence to realistic experimental parameters [77].

tuning the driving frequency. It is moreover important to realize that the discrimination power can be optimized by tuning g . In the optimized case, a local maximum of the multiphoton resonance for one qubit state can be made to coincide with a local minimum of the response for the opposite qubit state yielding to a maximal discrimination power. An example where the discrimination power has been optimized with respect to the three-photon resonance is shown in Fig. 4.3 (b).

4.6 Backaction in the qubit

Another important prerequisite for a useful detection scheme is that the coupling of the qubit to the detector around a multiphoton resonance does not generate a destructive back action on the qubit dynamics. In this section, we show that the back action in this design is surprisingly small for a realistic choice of parameters.

The back action of the detector on the qubit arises in the form of two contributions from the coupling. First, this coupling has a parametric component $\mathcal{H}_1 = g \cos \theta n \tau_z$, which commutes with the Hamiltonian. Thus, in the presence of a coupling of the oscillator to the bath, this term only produces dephasing and no relaxation, as it is, for instance,

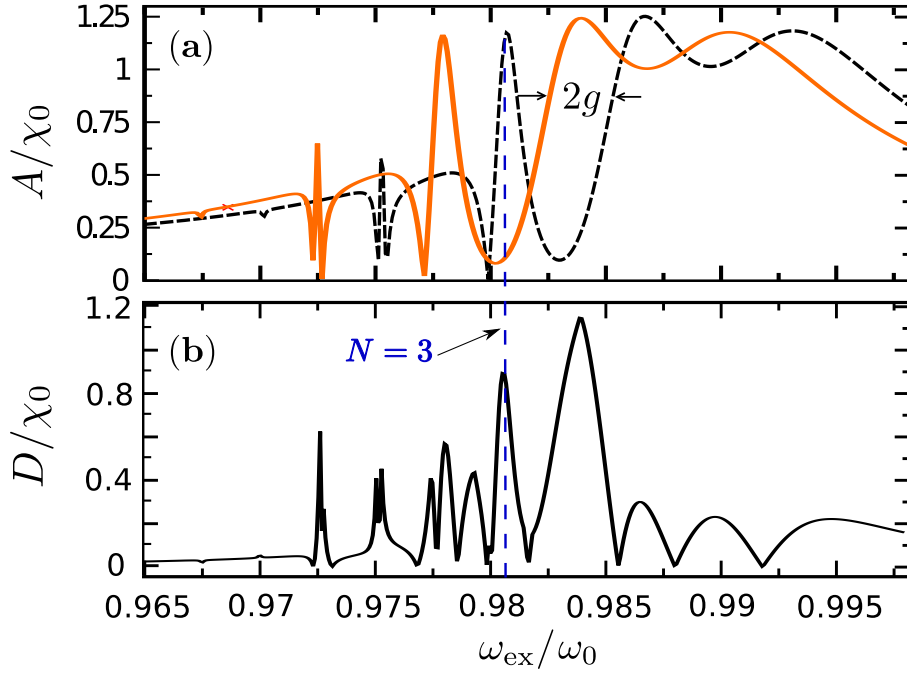


Figure 4.3: (Color online) (a) Nonlinear response A of the detector coupled to the qubit prepared in its ground state $|\downarrow\rangle$ (orange solid line) and in its excited state $|\uparrow\rangle$ (black dashed line) for the same parameters as in Fig. 4.2. The quadratic qubit-detector coupling induces a global frequency shift of the response by $\delta\omega_{\text{ex}} = 2g$. (b) Discrimination power $D(\omega_{\text{ex}})$ of the detector coupled to the qubit for the same parameters as in (a).

required for a quantum non-demolition measurement. This part guarantees an efficient detection of the qubit state. The second component $\mathcal{H}_2 = g \sin \theta (a^\dagger{}^2 \tau^- + a^2 \tau^+)/2$ in the coupling term yields transitions in the qubit when two-photon processes are induced in the detector by the external driving and/or by dissipative transition. Since, at low temperature, dissipation is dominated by photon leaking and the driving is very weak, the decay rate of the qubit from its excited state to its ground state accompanied by the emission of two oscillator photons, largely exceeds the excitation rate from the ground state to the excited state accompanied by the absorption of two photons originally coming from the bath or the driving. On the other hand, when the effective oscillator frequency is close to a multiphoton resonance, photon absorption in the coupled system is enhanced and thus the asymptotic qubit population might be reduced.

Thus, for a large asymmetry $|\epsilon| \gg \Delta$, peaks and dips in the qubit population difference P_∞ are expected when multiphoton transitions in the detector are induced. This is what is shown in Fig. 3.4(a), where P_∞ is shown for several values of f . For an easier orientation, we show in addition the corresponding stationary nonlinear response of the detector in Fig. 3.4(b). For increasing driving, the deviation from the expected value $P_\infty = -1$ becomes

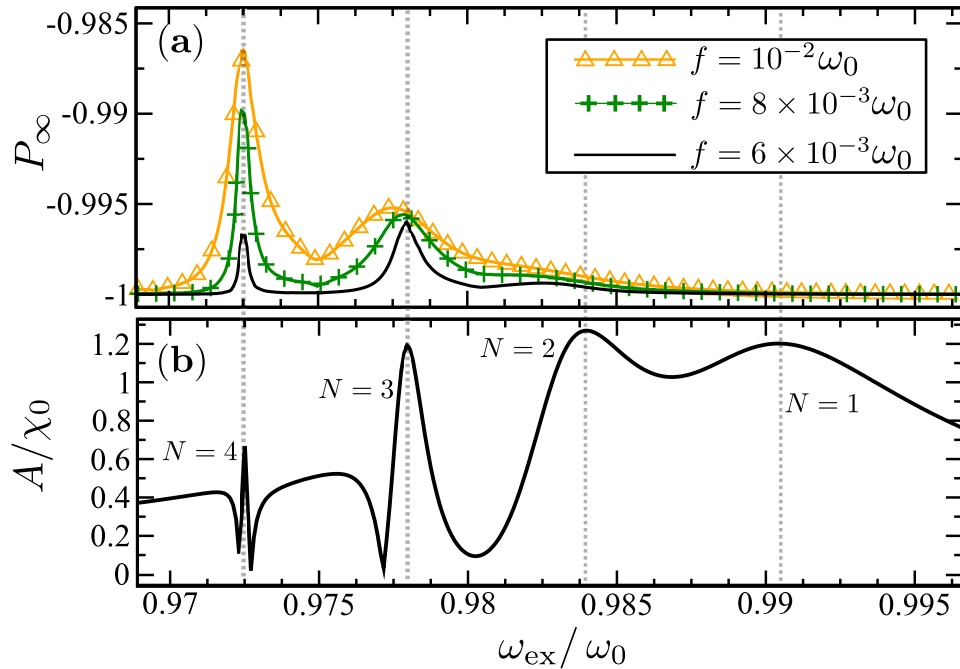


Figure 4.4: (Color online) (a) Asymptotic population difference P_∞ of the qubit states, and (b) the corresponding detector response A as a function of the external frequency ω_{ex} for the same parameters as in Fig. 4.2.

more pronounced for larger photon numbers N and larger driving f . The reason is that, for increasing driving, a larger Rabi frequency for the corresponding transition results [cf. Eq. (3.9)]. From Fig. 3.4, it follows that when the qubit is prepared in its ground state $|\uparrow\rangle$ (we consider $\epsilon \gg \Delta$) the back action is very small. The impact is less than 2% for the considered realistic parameters, yielding to a readout contrast of more than 98%. This has to be compared with presently achievable readout contrasts of less than 90%, [79] which results from an architecture with a classical Josephson bifurcation amplifier. In passing, we note that the detector response can also be calculated from the stationary solution of the master equation (2.52), but for the parameters considered here (in particular because of the large qubit bias), this coincides with the shifted one.

Moreover, we note that the components \mathcal{H}_1 and \mathcal{H}_2 can be tuned by ϵ and Δ . Therefore, $g \sin \theta$ can in principle be eliminated by setting $\Delta = 0$, which would imply that the measurement scheme keeps the state of the qubit without any relaxation but only pure dephasing (ideal quantum nondemolition measurement). However, turning off the splitting implies a major change in the experimental design of the sample, since this parameter is determined by the Josephson energy in the junctions of the superconducting flux qubit and, thus, may not be easy to be realized.

The back action of the detector on the qubit should be small not only when the qubit

is in its ground state but also when it is in its excited state. We therefore address next the relaxation rate of the qubit. Energy relaxation in the qubit induced by the measurement process will be proportional to the fluctuations of the square of the phase operator χ_+ induced by the detector's environment.[13, 76] This relaxation process is characterized by the transition rate [13, 76]

$$\Gamma \simeq \tilde{g}^2 \sin^2 \theta \mathcal{S}_{\chi_+^2}(-\omega_{\text{qb}}), \quad (4.15)$$

which has been computed perturbatively to lowest order in \tilde{g} . Here,

$$\mathcal{S}_{\chi_+^2}[\omega] = \frac{\omega_{\text{ex}}}{4\pi} \int_0^{2\pi/\omega_{\text{ex}}} dt \int_{-\infty}^{+\infty} d\tau e^{i\omega\tau} \langle \{\chi_+^2(\tau+t), \chi_+^2(t)\} \rangle \quad (4.16)$$

is the symmetrized power spectrum of χ_+^2 averaged over the period of the external driving [cf. Sec. 2.2], with $\{, \}$ indicating the anticommutator. The fact that information on the qubit state is acquired in the detector via the same channel by which dissipation is introduced is nicely reflected in the expression of the relaxation rate in Eq. (4.15). In Fig. 3.5(a), the relaxation rate Γ is shown for a large negative asymmetry in the qubit. The relaxation rate is strongly peaked around the multiphoton transitions. There, the noise from the detector absorbs more energy from the qubit around the multiphoton transition $(0, N)$ since the parametric component \mathcal{H}_1 of the coupling becomes negligible, leading to a dominant relaxation process induced by \mathcal{H}_2 .

We emphasize that although the relaxation is maximally enhanced at a multiphoton resonance, the absolute value of Γ is still very small in comparison to the damping constant, e.g., $\Gamma/\gamma \sim 10^{-6}$. Thus, we can infer the qubit state with sufficient precision by operating the detector in its steady state regime as it has been assumed in Section 4.5.1.

4.7 Efficiency of the measurement

The measurement of the qubit state requires a coupling to the outer world, which clearly introduces noise to the qubit. In turn, the noisy detector yields measurement results, which are statistically distributed. This implies that several measurements have to be performed to obtain a reliable statistics. Hence, the relaxation time of the qubit state should not only exceed the typical relaxation time of the detector but also the time it takes to acquire sufficient information to infer the qubit state (the measurement time T_{meas}). Hence, for a good measurement fidelity, T_{meas} should be smaller than the characteristic time Γ^{-1} given by Eq. (4.15), or, $\Gamma_{\text{meas}}/\Gamma \gg 1$.

The measurement time can be formalized [9, 13, 76] as the ratio of the symmetrized power spectrum \mathcal{S}_{χ_+} of the phase operator χ_+ (evaluated at zero frequency) and the square

of the difference between the two expectation values of χ_+ when the qubit is in the two opposite states, i.e., with Eq. (4.14),

$$T_{\text{meas}} = \frac{\mathcal{S}_{\chi_+}}{[D(\omega_{\text{ex}})]^2}. \quad (4.17)$$

The result for T_{meas} as a function of ω_{ex} is shown in Fig. 3.5 (b) for the parameter set used above, for which the discrimination power $D(\omega_{\text{ex}})$ around the 3-photon resonance has been maximized. In correspondence with this is the relative minimum of T_{meas} around the 3-photon resonance, see Fig. 3.5 (b). Interestingly enough, the time scale of the measurement time around this resonance is $T_{\text{meas}} \approx 10^{-2} \times 2\pi/\omega_0$. Considering realistic numbers of a typical experimental set-up [77], where ω_0 is in the regime of a few GHz, we obtain a time scale of $T_{\text{meas}} \approx 100$ ps for the nonlinear quantum detection scheme. This should be contrasted to the measurement time of $T_{\text{meas}} \approx 300$ ns obtained in Ref. 77. In between the multiphoton resonances, the dependence of T_{meas} on ω_{ex} shows a rich structure including several singularities, which are simply due to the several crossings of the two nonlinear response curves shown in Fig. 3.3 (a), where $D(\omega_{\text{ex}})$ becomes zero, implying insufficient discrimination of the two qubit states.

With this, we can evaluate the measurement efficiency, defined by the ratio $\Gamma_{\text{meas}}/\Gamma$, with $\Gamma_{\text{meas}} = T_{\text{meas}}^{-1}$. This quantity sets the probability to infer the qubit state, based on the nonlinear response of the detector. We show the result for the efficiency of the measurement in Fig. 3.5(c). Related to the multiphoton resonances in the detector, the efficiency also shows local maxima. For the discrimination power being optimized around the three-photon resonance, the measurement efficiency displays a clear local maximum [cf. Fig. 3.5(c)]. Due to the small size of the relaxation rate Γ of the detector, the overall measurement efficiency is rather large in comparison to the detection set-up with a linear resonator, [77] ensuring $\Gamma_{\text{meas}}/\Gamma \gg 1$.

4.8 Conclusions

To conclude, we have in this Chapter introduced a scheme for quantum state detection on the basis of a nonlinear detector which is operated in the regime of resonant few-photon transitions. Discrete multiphoton resonances in the detector can be used to infer the state of the parametrically coupled qubit via a state-dependent frequency shift of the detector's nonlinear response function. The multiphoton resonances are well separated in the spectrum and sharp enough to allow for a good resolution of the qubit state.

By analyzing key quantities of the detector, we have shown that the nonlinear few-photon detector can be operated efficiently, reliably, and with sufficiently weak back action.

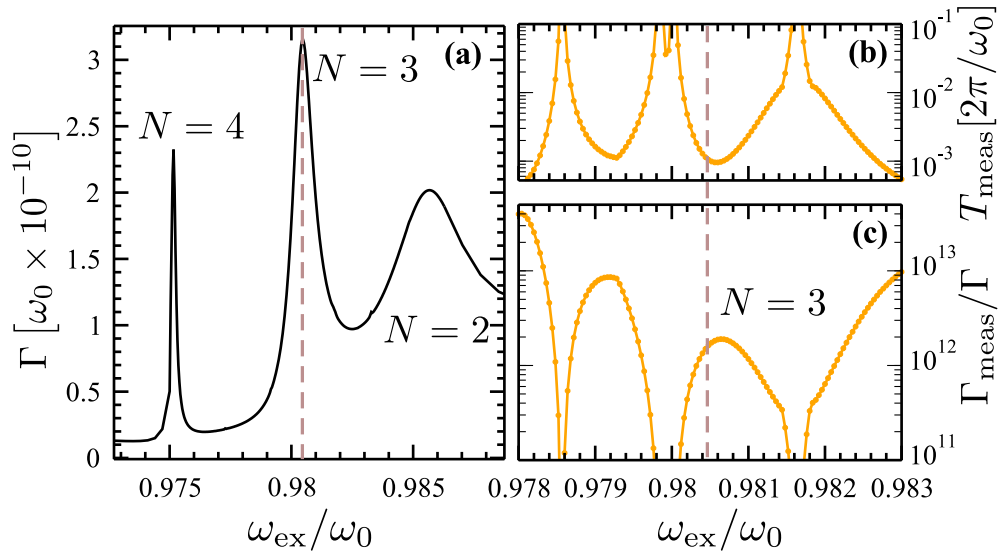


Figure 4.5: (Color online) (a) Relaxation rate Γ of the nonlinear quantum detector, (b) the measurement time T_{meas} , and (c) the measurement efficiency $\Gamma_{\text{meas}}/\Gamma$ as a function of the external frequency ω_{ex} . The parameters are the same as in Fig. 4.2.

In fact, it can be efficiently tuned by tuning the amplitude of the ac bias current of the SQUID. Furthermore, we have shown that the sharpness of the multiphoton resonances can be used to obtain an increased discrimination power as compared to the linear parametric detection scheme. Clearly, the relaxation rate at a multiphoton resonance for the qubit becomes maximal, but in general remains very small. The measurement time around a multiphoton resonance can be tuned such that it becomes minimal. For realistic experimental parameters, we find surprisingly small measurement times, allowing in principle for fast measurements. Moreover, the efficiency of the measurement, which takes the time to acquire enough information to infer the qubit state into account, also assumes large values, thus allowing for a reliable and highly efficient measurement of the qubit state.

We have chosen realistic values for the involved model parameters such that an experimental realization of this quantum measurement scheme should become possible in the near future. The nonlinear detection scheme in the deep few-photon quantum regime offers thus the advantage of an increased discrimination power of more than 98% (for our choice of realistic parameters), as compared to previous classical detection schemes based on the Josephson bifurcation amplifier.

A possible setup in order to realize the nonlinear few-photon detector could be the architecture used in a recent experiment.[82] The low-temperature regime, where quantum noise effects are important, has already been reached. In order to operate in the regime of only few photons in the resonator, the sensitivity and stability of the devices might have still to be further increased. However, no principle obstacles are apparent.

Nonequilibrium quantum transport in nanoscale systems

In Chapter 2 we introduced the model for the dissipation mechanism in the quantum regime. We reviewed the most successful model, the system-bath-model, where the system is bilinearly coupled to an environment composed of noninteracting harmonic oscillators (bosonic bath). In this chapter, we shall consider the interaction of two out-of equilibrium environments yielding a charge and thus a particle current. The nonequilibrium condition in this context refers to either a difference between the temperatures of both environments or a difference in their chemical potential. The former would produce a heat current whereas the latter induces a flow of electric charges. The flowing current is the manifestation of the total system reaching a nonthermal statistical state.

Besides currents between two environments, we are most often actually interested in the behaviour of technical components placed in between the environments, like transistors or molecular junctions. Thus, we name the two environments at different temperature/electrochemical potential in the following as leads and as central system we describe any possible component between them.

In this chapter we consider nonequilibrium quantum transport in nanoscale systems. We start with a brief introduction of single-electronic devices, followed by the discussion of dimensionality of the central system. We restrict ourselves to the cases of zero and one dimensional gases. Finally, we present a diagrammatic method for the solution of the master equation for the reduced density operator.

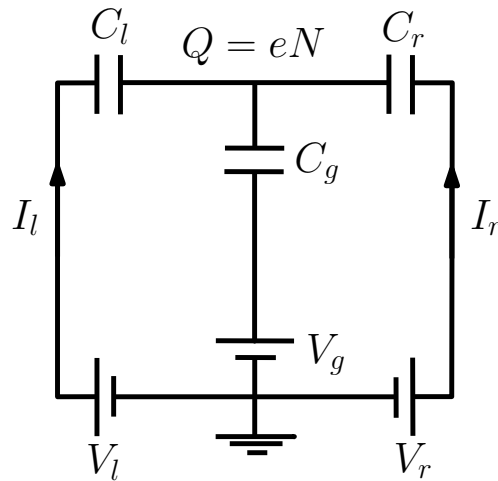


Figure 5.1: Equivalent circuit of a single-electron transistor, which can be controlled by a gate voltage V_G and a source-drain voltage (bias voltage) $V = V_l - V_r$. Due to the small capacitance of the dot, the electric charge is well defined.

5.1 Single-electron devices

A single electron device is a mesoscopic structure whose transport properties are dominated by single-electron tunneling. Owing to the similarity to real transistors, most of these devices are called *single-electron transistors*. The prototype device, an equivalent circuit is shown in Fig. 5.1, consist of a central island which is connected to two electrodes via tunnel junctions, and a plunger gate with voltage V_g . Each of the three components has a capacitance and a voltage which controls its electrochemical potential. The capacitance in mesoscopic structures can be sufficiently low, such that the energy to charge the device with one electron becomes the largest energy scale, nowadays of the order of or even larger than the room temperature. Consequently electronic transport becomes sequential, i.e. electron are transferred across the system one by one. This is the regime of single-electron tunneling, which is studied throughout this part of the thesis.

5.2 Electron gases in zero and one dimension

In this section we discuss possible experimental implementations of the aforementioned devices. We restrict ourselves to only a few possible realizations, where the carriers are confined in a potential such that their motion in two or three directions is restricted and thus is quantized, i.e., one (carbon nanotubes) or zero (quantum dots) dimensional confined electron gases.

Quantum dots are small islands where the energy of the capacitive electrons is quantized due to the small dimensions (compare to the Fermi wavelength), thus showing a discrete spectrum. Semiconducting systems show energy quantization already at system sizes of order 100 nm[89] which is quite large compared to metallic systems which much higher density of states. Due to the resemblance to atoms and molecules in the level structure quantum dots are often called artificial atoms. Just as real atoms, quantum dots can be brought together to form artificial molecules. Double quantum dots which are connected in series can form bonding and anti-bonding states. However, quantum dots can also be purely Coulomb-coupled,[90] without particle exchange, allowing new applications and interesting physics, such as charge measurements with single charge accuracy, which can be used as read-out devices for qubits.[10] Large molecules like C_{60} can be either used as a precursor in order to synthesize quantum dots on a ruthenium surface[91] or be placed in the gap between two electrodes, and thus play the role of quantum dots. The latter[92] can also be realized by contacting the molecule with a scanning tunneling microscope tip from above. A metallic layer below the substrate can act as a gate in the two electrode case, while the control knob for a scanning tunneling microscope setup can be realized by changing the tip-to-molecule distance, i.e., by the voltage applied to the tip's Piezo element. Contacting a molecule between two electrodes which are about 1 nm apart is extremely difficult. Today's standard approach is to form the electrode by a break-junction technique and to place the molecules by spilling a solution with the molecules over the junction. Despite the lack of accuracy concerning the number of molecule in the junction, the mere demonstration of feasibility can be considered a major achievement.

Single wall carbon nanotubes (SWNT) constitute molecular wires (quasi-one dimensional electron gas) with remarkable electronic properties and perhaps the best possibility for studying quantum electromechanical phenomena. A carbon nanotube can be viewed as a normal graphite sheet rolled up into a cylinder with a radius $R_0 < 5$ nm [93, 94] and a length L more than a thousand times R_0 . [see Fig. 5.2] Rigorously, a SWNT is an ideal one dimensional system since its Fermi wavelength λ_F is shorter than the longitudinal SWNT length L . The typical wavelength of electrons in the SWNT around the Fermi level, where the majority of the charge carriers is located, is about 0.8 nm.[95] In such low-dimensional systems, subtle and sophisticated features appear which are deeply rooted in quantum mechanics and tightly associated with many-body interactions.[96, 97]

5.3 Hamiltonian model

The single-electron transistor is modelled by the standard Hamiltonian $H(t) = H_0(t) + H_T$, in which $H_0(t)$ describes the decoupled system and H_T the tunneling between the leads and

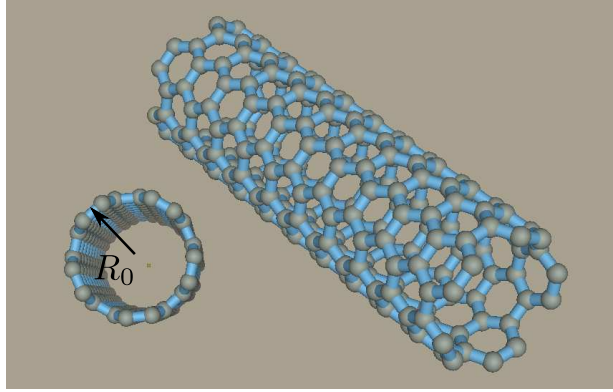


Figure 5.2: Single wall carbon nanotube of radius R_0 , and length $l \gg R_0$ (not shown in the sketch).

the island. The decoupled system consists of noninteracting electrons (fermion bath) in the left and right lead, and a system in the gap region between leads,

$$H_0(t) = H_c + H_l(t) + H_r(t), \quad (5.1)$$

where H_c describes the Hamiltonian for the central system, and $H_{l/r}(t)$ the Hamiltonian for the left/right (l/r) lead. In addition, we consider a time-dependent bias voltage $V(t)$ between leads yielding an accumulation or depletion of charge near the barriers. The unscreened Coulomb interaction between the net excess charge is quite strong, and hence the bias across a tunneling structure is caused by a relatively small excess charge in accumulation and depletion layers. The formation of these layers then causes a rigid shift of the bottom of the conduction band deeper in the leads, which is the origin of the rigid shift of energy levels.[98] Thus, the resulting electrostatic potential difference makes the single-particle energies in each lead time-dependent according to

$$\epsilon_{k,l/r} = \epsilon_{k,l/r}^0 - \mu_{l/r} \rightarrow \epsilon_{k,l/r}(t) = \epsilon_{k,l/r}^0 - \tilde{\mu}_{l/r}(t), \quad \text{with} \quad \tilde{\mu}_{l/r}(t) = \mu_{l/r} + eV_{l/r}(t), \quad (5.2)$$

where $\mu_{l/r}$ and $V_{l/r}(t)$ are a static electrochemical potential and the time-dependent bias voltage applied on the left/right lead, respectively. The bias voltages $V_{l,r}(t)$ follow the constraint $V_l(t) - V_r(t) = V(t)$, where $V(t)$ is the time-dependent drop across the central region. Despite the time-dependent modulation in the bias voltages, the occupation of each state k in the left/right lead remains unchanged. The occupation, for each contact, is determined by an equilibrium distribution function established in the distant past, without considering time dependent potentials or tunneling events between system and leads. Therefore, the lead Hamiltonian reads

$$H_p(t) = \sum_k [\epsilon_{k,p}^0 - \tilde{\mu}_p(t)] c_{k,p}^\dagger c_{k,p}, \quad \text{with} \quad p = l, r. \quad (5.3)$$

There $c_{k,l/r}^\dagger$ ($c_{k,l/r}$) creates (destroys) an electron in k -th state (including spin) in the left/right lead.

Next, we assume bilinear coupling between the leads and the central system describing the tunneling of one electron from the leads to central system and vice-versa. Thus, the tunneling part is given by

$$H_T = H_{T,l} + H_{T,r}, \text{ with } H_{T,l/r} = \sum_k T_{k,l/r} d c_{k,l/r}^\dagger + h.c. . \quad (5.4)$$

Here d^\dagger (d) creates (destroys) an electron in the central region, and $T_{k,l/r}$ denotes the tunneling matrix elements for the left/right lead.

The tunnel coupling leads to a finite lifetime τ of the states in the central system and therefore to an intrinsic level broadening $\Gamma = \hbar/\tau$. This broadening is related to the tunnel rates $2\gamma_{l/r}^\pm(\hbar\omega) = \Gamma_{l/r}(\hbar\omega)f_{l/r}^\pm(\hbar\omega)$ into/out-of (+/-) the central system through the left/right barrier, obtained from simple Golden-Rule arguments, by $\Gamma = \Gamma_l + \Gamma_r$ and $\Gamma_{l/r}(\hbar\omega) = (2\pi/\hbar) \sum_k |T_{k,l/r}|^2 \delta(\hbar\omega - \epsilon_{k,l/r})$. Hereafter $f_{l/r}^+(\hbar\omega) = (\exp[\beta(\hbar\omega - \mu_{l/r})] + 1)^{-1}$ denotes the Fermi distribution in the left/right lead with electrochemical potential $\mu_{l/r}$, whereas $f_{l/r}^-(\hbar\omega) = 1 - f_{l/r}^+(\hbar\omega)$.

Furthermore, we assume the standard wide-band limit approximation, where the tunneling matrix elements are independent on the energy of states, i.e., $T_{k,l/r} \rightarrow T_{l/r}$. This means that the density of states in the leads $\mathcal{D}(\epsilon_{l/r})$ is approximately constant around the respective lead Fermi energy and, therefore, the level broadening from each lead becomes constant $\Gamma_{l/r} = (2\pi/\hbar)|T_{l/r}|^2 \mathcal{D}(\epsilon_F)$.

For later purposes it is convenient to switch into a frame of reference where the tunneling is driven by the time-dependent bias voltage. To do this, we use the transformation

$$\mathcal{U}_V(t) = \exp \left[i(e/\hbar) \sum_k \phi_l(t) c_{k,l}^\dagger c_{k,l} + (l \rightarrow r) \right], \quad \text{with } \phi_{l/r}(t) = \int_{t_0}^t ds V_{l/r}(s). \quad (5.5)$$

In this frame of reference the transformed Hamiltonian reads as:

$$H_V(t) = \mathcal{U}_V^\dagger(t) H(t) \mathcal{U}_V(t) - i\hbar \mathcal{U}_V^\dagger(t) \dot{\mathcal{U}}_V(t).$$

Above, the first term rescales the creation and destruction operators in the leads, $c_{k,l/r} \rightarrow c_{k,l/r} \exp[-ie\phi_{l/r}(t)/\hbar]$, and the second term reproduces the time-dependent part of the leads Hamiltonian, $i\hbar \mathcal{U}_V^\dagger(t) \dot{\mathcal{U}}_V(t) = -(\sum_k \tilde{\mu}_l(t) c_{k,l}^\dagger c_{k,l} + (l \rightarrow r))$. Thus, the time dependence is translated to the tunneling term. There one can merge the rescaling factor of the creation and destruction operators, $\exp[\pm i(e/\hbar)\phi_{l/r}(t)]$ with the tunneling matrix elements $T_{l/r}$ into

$$\tilde{T}_{l/r}(t) = T_{l/r} \exp[-ie\phi_l(t)/\hbar], \quad (5.6)$$

yielding time dependent tunneling matrix elements.

5.4 Real-time transport theory

In this section we review a general transport theory based on a real-time diagrammatic approach. This theory [99, 100] is closely related to the path-integral method formulated in Chapter 2. Similarly, the basic idea is to integrate out all reservoir degrees of freedom and thus end up with a formally exact kinetic equation for the reduced density matrix of the central system.

In the following, we consider the system in a frame of reference transformed by $\mathcal{U}_V(t)$ [cf. Eq. (5.5)], i.e., where the leads and the central are static but the tunneling matrix elements. In analogy with the bosonic case, we assume that the initial density matrix for the total system (leads + central system) factorizes into parts for the central system (ρ) and the leads ($\rho_{l/r}$), i.e.,

$$W(t_0) = \rho(t_0) \otimes \rho_l \otimes \rho_r . \quad (5.7)$$

The leads are treated as large equilibrium reservoirs at temperature T with fixed electrochemical potentials $\mu_{l/r} = -eV_{l/r}$. The electron distribution is therefore given by Fermi functions $f_{l/r}^+(\omega)$ and the density operator reads

$$\rho_{l/r} = \frac{\exp[-\beta \sum_k (\epsilon_{k,l/r} - \mu_{l/r}) c_{k,l/r}^\dagger c_{k,l/r}]}{\text{Tr}[\exp[-\beta \sum_k (\epsilon_{k,l/r} - \mu_{l/r}) c_{k,l/r}^\dagger c_{k,l/r}]]} \quad \text{with} \quad \beta = 1/k_B T . \quad (5.8)$$

The time evolution of the density operator $W(t)$ in the interaction picture is given by

$$W^I(t) = \mathcal{U}^I(t, t_0) W(t_0) [\mathcal{U}^I(t, t_0)]^\dagger , \quad (5.9)$$

where $\mathcal{U}^I(t, t_0) = \mathcal{T} \exp[-i\Phi(t, t_0)]$, therein $\Phi(t, t_0) = \int_{t_0}^t ds H_T^I(s)/\hbar$ and \mathcal{T} is the time ordering operator. The superscript I denotes the interaction picture.

In the superoperator notation, Eq. (5.9) can be written as $W^I(t) = \mathcal{T} \exp[-i\Phi(t, t_0)] \cdot W(t_0)$, where $\Phi(t, t_0) \cdot W(t_0) = [\Phi(t, t_0), W(t_0)]$. Thus, the density operator at an arbitrary time $W^I(t)$ can be written as a deviation of the initial preparation in a transcendental equation, i.e. $W^I(t) = W(t_0) - i\Phi(t, t_0) \cdot W^I(t)$. This structure allows to expand the time evolution of the density operator W in orders in the tunneling coupling. Furthermore, we can write the reduced density operator, after tracing over the degrees of freedom of the leads, as

$$\rho^I(t) = \text{Tr}_{l,r}[W^I(t)] = \rho(t_0) + \frac{1}{i\hbar} \int_{t_0}^t dt_1 \text{Tr}_{l,r}[H_T^I(t_1), W^I(t_1)] , \quad (5.10)$$

where $\text{Tr}_{l,r}$ denotes the trace over the degrees of freedom of the right and left lead. Differentiating with respect to t , we obtain the master equation for the reduced density operator,

$$\frac{d}{dt} \rho^I(t) = -\frac{1}{\hbar^2} \int_{t_0}^t dt_1 \text{Tr}_{l,r} [[H_T^I(t), [H_T^I(t_1), W^I(t_1)]] ,] \quad (5.11)$$

where, for simplicity, we have eliminated the term $(1/i\hbar)\text{Tr}_{l,r}[[H_T^I(t), W^I(t_0)]]$ with the assumption $\text{Tr}_{l,r}[H_T^I(t)\rho_l \otimes \rho_r] = 0$. This is equivalent to consider $\rho_l \otimes \rho_r$ diagonal in energy basis, in other words, it is equivalent to the assumption that the leads are at their respective equilibrium.

We have stated that W^I factorizes at $t = t_0$. At later times correlations between leads and the central system may arise due to the tunneling term H_T . However, for a very weak coupling, at all times $W(t)$ should only show deviations of order H_T from an uncorrelated state. Thereby, taking into account that the leads are considered as very large whose state should be virtually unaffected, we can estimate the total state as

$$W^I(t) = \rho^I(t) \otimes \rho_l \otimes \rho_r + O(H_T) . \quad (5.12)$$

We now make our first major approximation, a *Born approximation* by neglecting terms higher than second order in H_T in (5.11). Thus, making an iterating procedure plugging Eqs. (5.10) and (5.12) into the equation of motion Eq. (5.11), we can determine the effects of the leads on the central system in many orders in the tunneling term $H_T^I(t)$. In doing so, we can write down the master equation as

$$\frac{d}{dt}\rho(t) = \frac{1}{i\hbar}[H_c, \rho(t)] + \int_{t_0}^t dt_1 \Sigma(t, t_1) \cdot \rho(t_1) . \quad (5.13)$$

In order to describe the coherent dynamics separately from the dissipative one we have switched to the Schödinger picture. Thus, the first term on the right hand side governs the dynamics of the close central system, whereas the second term encloses all the effects of the fermionic bath covered by $\Sigma(t, t_1)$, i.e., self-energies which are induced by the leads in arbitrary orders in the tunneling. In the diagrammatic expansion of Eq. (5.13), the self energy $\Sigma(t, t_1)$ encloses only irreducible terms.

The dissipative part of the master equation (5.13) depends on the evolution of $\rho(t)$ from the initial time t_0 to the evaluation time t , including memory effects in the dynamics. In the weak level broadening limit, we can invoke the Markovian approximation neglecting the memory effects (replacing $\rho(t_1)$ by $\rho(t)$ in the second term on the right hand side in Eq. (5.13)), yielding a deterministic equation of motion for $\rho(t)$, a *Markov* master equation, as

$$\frac{d}{dt}\rho(t) = \frac{1}{i\hbar}[H_c, \rho(t)] + \left(\int_{t_0}^t dt_1 \Sigma(t, t_1) \right) \cdot \rho(t) . \quad (5.14)$$

In order to calculate the self-energies $\Sigma(t, t_1)$, the trace over the degrees of freedom of the leads has to be performed. Here, the corresponding sum over the leads' states can be replaced by integrals over the energy spectrum using the density of states in the leads $\mathcal{D}(\epsilon)$ in the wide-band-limit, i.e., $\sum_k \rightarrow \int_{-\infty}^{+\infty} d\epsilon_{l/r} \mathcal{D}(\epsilon_{l/r}) \approx \mathcal{D}(\epsilon_F) \int_{-\infty}^{+\infty} d\epsilon_{l/r}$. For the calculation of the resulting integrals, introducing diagrams on the Keldysh contour simplifies the notation. We refer to Refs. 99 and 100 for a detailed description.

5.4.1 Calculation of the self energy Σ to first order in Γ

The lowest order term of the expansion in the self-energies corresponds to the first iteration of Eqs. (5.12), (5.10), and (5.11). The diagrams represent the evolution of the system in real time. The lowest order diagrams carry a factor $|T_{l/r}|^2$ due to the conservation of the number of particles. Since the integrations associated with a Feynman diagram run only over the loop energy, it is convenient to introduce a reduced diagram which represents precisely the loop integrations by removing all external lines. In addition, they are the smallest nontrivial Feynman diagrams which form the basic building blocks of all diagrams. To calculate these irreducible diagrams, it is convenient to split the tunneling term H_T into two parts, describing the creation (+) and destruction (−) of an electron in the central system,

$$H_T^I(t) = H_T^+(t) + H_T^-(t) \quad (5.15)$$

where $H_T^-(t) = [H_T^+(t)]^\dagger$, and

$$H_T^+(t) = H_{T,l}^+(t) + H_{T,r}^+(t), \quad \text{with} \quad H_{T,l}^+(t) = \sum_k \tilde{T}_{l/r}(t) d^\dagger(t) c_{k,l/r}(t). \quad (5.16)$$

In order to simplify the notation we omit the superscript for the interaction picture for creation and annihilation operators. It is implicitly assumed unless stated otherwise.

The lowest order of the expansion of Σ can be written as

$$\begin{aligned} \int_{t_0}^t dt_1 \Sigma(t, t_1) \cdot \rho(t) &= \Sigma(t) \cdot \rho(t) \\ &= -\frac{1}{\hbar^2} \mathcal{T}_K \int_K dt_1 \left(\langle H_T^+(t) H_T^-(t_1) \rho^I(t) \rangle_{lr} + \langle H_T^-(t) H_T^+(t_1) \rho^I(t) \rangle_{lr} \right. \\ &\quad + \langle \rho^I(t) H_T^+(t_1) H_T^-(t) \rangle_{lr} + \langle \rho^I(t) H_T^-(t_1) H_T^+(t) \rangle_{lr} \\ &\quad - \langle H_T^+(t) \rho^I(t) H_T^-(t_1) \rangle_{lr} + \langle H_T^-(t) \rho^I(t) H_T^+(t_1) \rangle_{lr} \\ &\quad \left. - \langle H_T^+(t_1) \rho^I(t) H_T^-(t) \rangle_{lr} + \langle H_T^-(t_1) \rho^I(t) H_T^+(t) \rangle_{lr} \right), \end{aligned} \quad (5.17)$$

where $\langle \dots \rangle_{lr} = \text{Tr}_{l,r}[(\dots)\rho_l \otimes \rho_r]$, K denotes the closed Keldysh contour which runs from t_0 to t on the real axis and then back again from t to t_0 , and \mathcal{T}_K the corresponding time ordering operator on the Keldysh contour.

In the next chapter we shall stick to the lowest order only. This gives insight into the sequential tunneling regime, when the time an electron spends on the central system is much larger than all coherence times.

5.4.2 Extension to the harmonically driven case

Since the influence of the driving field in the dynamics of the leads corresponds to a shift in their energy levels, i.e., $\epsilon_{k,l/r} \rightarrow \epsilon_{k,l/r} - eV_{l/r}(t)$, for a harmonic driving $V_{l/r}(t) = \pm V_0/2 \cos(\omega_{\text{ex}}t)$, the corresponding lead eigenstates evolve as[101–104]

$$\begin{aligned} |k_{l/r}(t)\rangle &= \exp\left[-\frac{i}{\hbar}\epsilon_{k,l/r}t + i\frac{eV_{l/r}}{\hbar\omega_{\text{ex}}}\sin(\omega_{\text{ex}}t)\right] |k_{l/r}\rangle \\ &= \sum_{m=-\infty}^{+\infty} J_m\left(\frac{eV_{l/r}}{\hbar\omega_{\text{ex}}}\right) \exp\left[-\frac{i}{\hbar}(\epsilon_{k,l/r} + m\hbar\omega_{\text{ex}})t\right] |k_{l/r}\rangle. \end{aligned} \quad (5.18)$$

Therefore, each state in the left/right lead contains sidebands whose energies are shifted by multiples of $\hbar\omega_{\text{ex}}$. Above, $V_{l/r} = V_{l/r}(t=0)$ and $J_m(x)$ are the ordinary Bessel functions of the first kind.

In the stationary case, the electron tunnels from the state $|k_{l/r}\rangle$ on left(right) lead into the state $|k_{r/l}\rangle$ on the right(left) one through the quantum dot. In the wide band limit, the tunneling matrix elements do not depend on the state of the leads. However, in the driven case, the sidebands of $|k_{l/r}(t)\rangle$ are involved in the tunneling process and sideband dependent tunneling matrix elements arise[101] according to

$$T_{l/r}^m(t) = T_{l/r} J_m\left(\frac{eV_{l/r}}{\hbar\omega_{\text{ex}}}\right) \exp[im\omega_{\text{ex}}t]. \quad (5.19)$$

This expression is directly derived from Eq. (5.6), where in the case of harmonic driving the accumulated phase by the driving field, $\phi_{l/r}(t) = \int_0^t ds V_{l/r}(s)$, can be expanded in terms of the Bessel functions. Thus, $\tilde{T}_{l/r}(t) = \sum_m T_{l/r}^m(t)$. We have assumed without loss of generality $t_0 = 0$ in the calculation of the accumulated phase $\phi_{l/r}(t)$.

Therefore, taking into account the contribution of the sidebands in the tunneling process, the first integral on the right hand side in Eq. (5.17),

$$\begin{aligned} -\frac{1}{\hbar^2} \mathcal{T}_K \int_K dt_1 \langle H_{T,l/r}^+(t) H_{T,l/r}^-(t_1) \rho^I(t) \rangle_{lr} &= -\frac{1}{\hbar^2} \mathcal{T}_K \int_K dt_1 \sum_{kk'} T_{l/r}^k(t) [T_{l/r}^k(t_1)]^* \\ &\quad \times d^\dagger(t) d(t_1) \langle c_{k,l/r}^\dagger(t) c_{k,l/r}(t_1) \rangle_{l/r} \rho^I(t) \end{aligned} \quad (5.20)$$

projected onto the eigenstates of the system Hamiltonian $|\chi\rangle$, $H_c|\chi\rangle = \epsilon_\chi|\chi\rangle$ (ϵ_χ is the corresponding eigenenergy), yields

$$\begin{aligned}
\chi_2^{\chi_1} [\Sigma_{l/r}^{(1)}(t)]_{\chi_2^{\chi_1}'} &= \sum_{m=-\infty}^{+\infty} \chi_2^{\chi_1} [\Sigma_{l/r,m}^{(1)}(\omega_{\text{ex}})]_{\chi_2^{\chi_1}'}^{\chi_1} e^{i m \omega_{\text{ex}} t}, \quad \text{with} \\
\chi_2^{\chi_1} [\Sigma_{l/r,m}^{(1)}(\omega_{\text{ex}})]_{\chi_2^{\chi_1}'} &= \frac{\hbar \Gamma_{l/r}}{2\pi} \sum_{k=-\infty}^{+\infty} \chi_2^{\chi_1} [\gamma_{l/r,k,m}^{(1)}(\omega_{\text{ex}})]_{\chi_2^{\chi_1}'}^{\chi_1}, \\
\chi_2^{\chi_1} [\gamma_{l/r,k,m}^{(1)}(\omega_{\text{ex}})]_{\chi_2^{\chi_1}'} &= \sum_{\chi'} \chi_1^{\chi_1} [\mathcal{T}_k^m(\omega_{\text{ex}})]_{\chi'}^{\chi_1'} \delta_{\chi_2 \chi_2'} \lim_{\eta \rightarrow 0^+} \int d\epsilon \frac{f_{l/r}^-(\epsilon)}{i(\epsilon_{\chi'} - \epsilon_{\chi_2}) + i(\epsilon - k \omega_{\text{ex}}) + \eta},
\end{aligned} \tag{5.21}$$

and $\chi_2^{\chi_1} [\mathcal{T}_k^m(\omega_{\text{ex}})]_{\chi_2^{\chi_1}'}^{\chi_1} = J_{k+m}(eV_{l/r}/\hbar\omega_{\text{ex}}) J_k(eV_{l/r}/\hbar\omega_{\text{ex}}) \langle \chi_1' | d | \chi_1 \rangle \langle \chi_2 | d^\dagger | \chi_2' \rangle$. The states in the tunneling tensor $\chi_2^{\chi_1} [\mathcal{T}_k^m(\omega_{\text{ex}})]_{\chi_2^{\chi_1}'}^{\chi_1}$ are linked by a forward propagation $\chi_1 \rightarrow \chi_1'$ and backward propagation $\chi_2 \leftarrow \chi_2'$ on the Keldysh contour. The superscript in (5.21) stands for the ordering in the diagrams, it is not related with the order of the perturbation theory.

For periodic voltages it is more convenient to study the kinetic equation and the tunneling current in Fourier-Laplace space. Therefore, in the following, we shall set up the diagrammatic rules to calculate directly the Fourier-Laplace transformation of the rates. The Fourier-Laplace transformation for Eq. (5.21) is given by

$$\begin{aligned}
\chi_2^{\chi_1} [\Sigma_{l/r,m}^{(1)}(z)]_{\chi_2^{\chi_1}'}^{\chi_1} &= \frac{\omega_{\text{ex}}}{2\pi} \int_0^{2\pi/\omega_{\text{ex}}} dt \int_0^\infty d\tau e^{-im\omega_{\text{ex}}t} e^{iz\tau} \chi_2^{\chi_1} [\Sigma_{l/r}^{(1)}(t, t - \tau)]_{\chi_2^{\chi_1}'}^{\chi_1} \\
&= \frac{\hbar \Gamma_{l/r}}{2\pi} \sum_{k=-\infty}^{+\infty} \chi_2^{\chi_1} [\gamma_{l/r,k,m}^{(1)}(z)]_{\chi_2^{\chi_1}'}^{\chi_1}, \quad \text{with} \\
\chi_2^{\chi_1} [\gamma_{l/r,k,m}^{(1)}(z)]_{\chi_2^{\chi_1}'}^{\chi_1} &= \sum_{\chi'} \chi_1^{\chi_1} [\mathcal{T}_k^m(\omega_{\text{ex}})]_{\chi'}^{\chi_1'} \delta_{\chi_2 \chi_2'} \int d\epsilon \frac{f_{l/r}^-(\epsilon)}{i(\epsilon_{\chi'} - \epsilon_{\chi_2}) + i(\epsilon + z - k \omega_{\text{ex}})}.
\end{aligned} \tag{5.22}$$

The relevant rules[99, 100] in energy space for the auxiliary rates $\gamma_{l/r,k,m}$ are:

- ① Draw all topologically different diagrams with fixed ordering of the vertices along real axis, i.e., irrespective on which branch they are in the Keldysh contour. The vertices are connected by tunneling lines. Assign a lead index (l/r) and the mode of the corresponding sideband to each tunneling line. The external vertices are connected by virtual lines with energies $m\omega_{\text{ex}}$.
- ② For each vertical cut between vertex $i - 1$ and vertex i we obtain a resolvent $1/(x_i + l_i\omega_{\text{ex}} + z)$, wherein x_i is the difference of the leftgoing minus the rightgoing energies (including the energies of sidebands) of the left/right lead, and dot lines), and l_i is the sum over all Fourier indices of left/right lead lines which are cut by the vertical line or lie right of it.

$$\chi_2^1 [\Sigma_{l/r,m}^{(1)}(z = i0^+)]_{\chi_2'}^{\chi_1'} = \frac{\hbar\Gamma_{l/r}}{2\pi} \sum_{k=-\infty}^{\infty} \begin{array}{c} \circ (k)_{l/r} \\ \chi_1 \xrightarrow{\quad} \chi_1' \\ \quad \quad \quad \nearrow \\ \quad \quad \quad (k+m)_{l/r} \\ \chi_2 \xleftarrow{\quad} \chi_2' \end{array}$$

Figure 5.3: First order diagram for tunneling between the central system and driven leads. The subscript 1 (2) in the states χ denotes the upper (lower) branch of the contour. At the reservoir line we have indicated which sideband of the reservoir state is involved. In the tunneling event holes are symbolized by open circles and electrons/particles by full circles.

- ③ Each vertex containing a central system operator O gives rise to matrix elements $\langle \phi_k | O | \phi_s \rangle$, where $|\phi_{k/s}\rangle$ is the state of the central system leaving/entering the vertex on the Keldysh contour.
- ④ Each directed tunneling line from the left/right lead gives rise to a factor

$$(-1)^v \gamma_{l/r}^{\pm,m}(\omega_{\text{ex}}) J_{k+m} (eV_{l/r}/\hbar\omega_{\text{ex}}) J_k (eV_{l/r}/\hbar\omega_{\text{ex}}),$$

if it is going forward/backward (+/−) with respect to the closed time path. Here v is the number of electron operators (due to external vertices) on the part of the Keldysh contour from t' to t . The function $\gamma_{l/r}^{\pm,m}(\omega_{\text{ex}})$ is given by

$$\gamma_{l/r}^{\pm,m}(\omega_{\text{ex}}) = f_{l/r}^{\pm}(E + m\hbar\omega_{\text{ex}}) \Gamma_{l/r}/2\pi$$

- ⑤ Each diagram carries a prefactor $(-i)^n (-1)^c$, wherein n is the total number of internal vertices and c the number of crossings of tunneling lines. There may be another minus sign appearing due to the order of fermionic operators in $\langle \phi_k | O | \phi_s \rangle$.
- ⑥ Integrate over the energies of the tunneling lines and sum over the leads state and spin indices (if relevant).

In the sequential tunneling regime, where the time an electron spends on the central system is much larger than all coherence times, and under the resonance condition $|\omega_0 - \omega_{\text{ex}}| \ll \omega_0$, the transport effects are relevant only on a time scale much larger than the period of the driving, i.e., $\Gamma < \hbar\omega_{\text{ex}}$. Therefore, we can invoke the high frequency approximation, as in Sec. 2.1.4.3, averaging over one period of the driving. Up to the first Fourier component in Eq. (5.21) this yields

$$\begin{aligned} \chi_2^1 [\Sigma_{l/r}^{(1)}(t)]_{\chi_2'}^{\chi_1'} &\approx \frac{\hbar\Gamma_l}{2\pi} \sum_{k=-\infty}^{+\infty} \chi_2^1 [\gamma_{l/r,k,0}^{(1)}(z = i0^+)]_{\chi_2'}^{\chi_1'}, \quad \text{with} \\ \chi_2^1 [\gamma_{l/r,k,0}^{(1)}(z = i0^+)]_{\chi_2'}^{\chi_1'} &= \sum_{\chi'} \chi_1^1 [T_k^0(\omega_{\text{ex}})]_{\chi'}^{\chi_1'} \delta_{\chi_2\chi_2'}(-i) \mathcal{I}_{+,l/r}^-(\epsilon_{\chi_2} - \epsilon_{\chi'}), \end{aligned} \quad (5.23)$$

where

$$\begin{aligned} \mathcal{I}_{\sigma,l/r}^{\pm}(\epsilon) &= -\pi i \sigma f_{l/r}^{\pm}(\epsilon) \mp \frac{1}{2} \left[\psi \left(\frac{1}{2} + \frac{i\beta}{2\pi}(\epsilon - \mu_{l/r}) \right) + \psi \left(\frac{1}{2} - \frac{i\beta}{2\pi}(\epsilon - \mu_{l/r}) \right) \right] \pm \\ &\quad \ln \left[\frac{\beta \omega_c}{2\pi} \right] \quad \text{with } \sigma = +, - . \end{aligned} \quad (5.24)$$

Above, the cut-off frequency ω_c is considered very large compared to the characteristic frequency of the system. The details of the relationship between the integral in Eq. (5.21) and the digamma function $\psi(x)$ are presented in App. D together with the results for the other self-energies in a diagrammatic representation. In Fig. 5.3 we show the diagrammatic representation of the rate $\frac{\chi_1}{\chi_2} [\Sigma_{l/r}^{(1)}(z = i0^-)]_{\chi_2'}^{X_1'}$ in the energy space, following the aforementioned rules.

We can see that, under the high frequency approximation, the dynamics of the reduced density operator is determined by time-independent rates, since one time can be fixed at zero and the Laplace transformation becomes $\gamma_{l/r,k,m} = \lim_{\eta \rightarrow 0} \int_{-\infty}^0 dt' \gamma_{l/r,k,m}(i\eta, t')$. Thus, we can replace the kernel by the self-energy calculated in energy space. In order to solve the Markov master equation we are left with the eigenvalue problem

$$\mathcal{L} \cdot \rho(t) \equiv \left[\mathbf{H}_c / i\hbar + \lim_{\eta \rightarrow 0} \Sigma(z = i\eta) \right] \cdot \rho(t) = \dot{\rho}(t) , \quad \text{with } \mathbf{H}_c \cdot \rho(t) = [H_c, \rho(t)] , \quad (5.25)$$

where

$$\rho(t) = e^{\mathcal{L}t} \rho(0) = \sum_k \text{Tr}[\rho_k^\dagger \cdot \rho(0)] e^{\Gamma_k t} \rho^k , \quad (5.26)$$

with $\mathcal{L} \cdot \rho^k = \Gamma_k \rho^k$, and $\rho_k \cdot \mathcal{L} = \Gamma_k \rho_k$. Therein, ρ^k (ρ_k) are the right (left) eigenoperators of \mathcal{L} with eigenvalue Γ_k . They have been introduced in Chapter 2. The time derivative in Eq. (5.26) vanishes when the steady state is reached and the state is determined by the right eigenoperator $\rho^{k'} \equiv \rho^\infty$ with the eigenvalue $\Gamma_{k'} = 0$.

5.4.3 Current

We now use this description to derive an expression for the current flowing out of the right/left lead. By definition, the current is given by the time derivative of the particle number $N_{l/r} = \sum_k c_{k,l/r}^\dagger c_{k,l/r}$, i.e., by

$$\begin{aligned} I_{l/r}(t) &= -e \frac{d}{dt} \langle N_{l/r}(t) \rangle = -i \frac{e}{\hbar} \langle [H(t), N_{l/r}(t)] \rangle \\ &= -i \frac{e}{\hbar} \left(\langle H_{T,l/r}^+(t) \rangle - \langle H_{T,l/r}^-(t) \rangle \right) . \end{aligned} \quad (5.27)$$

$$\begin{aligned}
(a) \quad I_{l/r,0} &= -i(e/\hbar) \sum_{\chi} \sum_{k=-\infty}^{\infty} \left(\begin{array}{c} \circ (k)_{l/r} \qquad \bullet (k)_{l/r} \\ \left(\begin{array}{c} \xrightarrow{\hspace{1.5cm}} \\ \xrightarrow{(k)_{l/r}} \bullet \chi \\ \xleftarrow{\hspace{1.5cm}} \\ \xleftarrow{(k)_{l/r}} \bullet \chi \end{array} \right) \end{array} \right) \\
(b) \quad I_{l/r,\pm 1} &= -i(e/\hbar) \sum_{\chi} \sum_{k=-\infty}^{\infty} \left(\begin{array}{c} \circ (k)_{l/r} \qquad \bullet (k \pm 1)_{l/r} \\ \left(\begin{array}{c} \xrightarrow{\hspace{1.5cm}} \\ \xrightarrow{(k \pm 1)_{l/r}} \bullet \chi \\ \xleftarrow{\hspace{1.5cm}} \\ \xleftarrow{(k)_{l/r}} \bullet \chi \end{array} \right) \end{array} \right)
\end{aligned}$$

Figure 5.4: Diagrams describing (a) the components of the stationary current $I_{l/r,0}$, and (b) the components of the alternating current $I_{l/r,\pm 1}$. The internal vertices are not shown.

In leading order of Γ , the current is determined by the components of the self energy, $\Sigma_{l/r}^{(5\dots 8)}$, which describe tunneling processes between leads [cf. App. D] as

$$\begin{aligned}
I_{l/r}(t) &= \sum_m I_{l/r,m} e^{im\omega_{\text{ex}}t} \quad \text{with} \quad (5.28) \\
I_{l/r,m} &= -i\frac{e}{\hbar} \left\langle \Sigma_{l/r,m}^{(5)}(\omega_{\text{ex}}) + \Sigma_{l/r,m}^{(8)}(\omega_{\text{ex}}) - \Sigma_{l/r,m}^{(6)}(\omega_{\text{ex}}) - \Sigma_{l/r,m}^{(7)}(\omega_{\text{ex}}) \right\rangle.
\end{aligned}$$

We symmetrize with respect to the leads, such that we compute the current $I(t) = I_l(t) - I_r(t)$. Note however that we are mainly interested in the stationary and the alternating current, $I_{st} = I_{l,0} - I_{r,0}$ and $I_{ac}(t) = \sum_{m=\pm 1} (I_{l,m} - I_{r,m}) e^{im\omega_{\text{ex}}t}$ respectively, with

$$I_{l/r,m} = -i\frac{e}{\hbar} \left\langle \Sigma_{l/r,m}^{(5)}(z = i0^-) + \Sigma_{l/r,m}^{(8)}(z = i0^+) - \Sigma_{l/r,m}^{(6)}(z = i0^+) - \Sigma_{l/r,m}^{(7)}(z = i0^-) \right\rangle_{\infty},$$

where $\langle \dots \rangle_{\infty} = \text{Tr}[\dots \rho^{\infty}]$.

The stationary and alternating currents describe different tunneling processes, which are explained as follows. We denote by $P_{nn'}$ the process of tunneling of an electron from the n -th sideband on the lead into the system, accompanied by the corresponding tunneling of a hole from the system into the n' -th sideband on the lead. The current $I_{l/r}$ describing the transport of an electron from the lead into the system, subtracting the transport of the corresponding hole which is created in the lead, without asking whether the electron has started and the hole has finished (n/n' -th sideband respectively), is given by the sum over all the currents corresponding to each process $P_{nn'}$, $\{n, n'\} \in \mathbb{Z}$. The current corresponding to all $P_{nn'}$ such that $n - n' = m$ is fixed, defines the harmonic component $I_{l/r,m}$. The stationary current is the special case $n = n'$. This component describes the creation of a particle (filled circle in Fig. 5.4(a)) in the central system and a hole (open circle in Fig. 5.4(a)) in the left/right lead conserving the sideband energy. On the other hand,

this conservation is not fulfilled for the alternating current ($n \neq n'$). The diagrams which represent the alternating current for the combination $n - n' = \pm 1$ are shown in Fig. 5.4(b).

5.5 Driven transport through a single level quantum dot

As an example, we consider the special case of a quantum dot with one single-particle state coupled to conducting leads. The Hamiltonian is given by

$$H(t) = E_d d^\dagger d + H_T + H_l(t) + H_r(t), \quad (5.29)$$

where E_d is the energy of the single level in the quantum dot, with d^\dagger and d as the creation and annihilation operator for electrons on the dot. H_T describes the standard bilinear coupling between the leads and the quantum dot given by Eq. (5.4), and $H_{l/r}(t)$ is the Hamiltonian of the leads driven by an ac-voltage [cf. Eq. (5.3)]. Under the transformation (5.5), the system is described by static leads and tunneling matrix elements involving the phase accumulated by the time-dependent bias voltage $\phi_{l/r}(t) = \int_{t_0}^t ds V_{l/r}(s)$ [cf. Eq. (5.6)].

The nonequilibrium problem treated in this section has been solved exactly by many authors using the Landauer-Büttiker formalism,[105–107] Keldysh formalism,[108–111] equation of motion methods,[112] and Golden-Rule approach with Lorentzian broadening of the energy conservation.[113] Here, we shall rederive the solution by solving the rate equation (5.26).

We denote the empty and singly occupied state by $|0\rangle$ and $|1\rangle$, respectively. The tunneling tensor is given by $\chi_2^1 T_{\chi_2'}^{\chi_1'} = \langle \chi_1' | d | \chi_1 \rangle \langle \chi_2 | d^\dagger | \chi_2' \rangle = \delta_{\chi_1,1} \delta_{\chi_2,1} \delta_{\chi_1',0} \delta_{\chi_2',0}$ and, therefore, the nonvanishing tensor elements of the rates are

$${}_1^1 \left[\Sigma_{l/r,0}^{(5)} \right]_0^0 = i \frac{\hbar \Gamma_{l/r}}{2\pi} \sum_{m=-\infty}^{+\infty} J_m \left(\frac{eV_{l/r}}{\hbar \omega_{\text{ex}}} \right)^2 \mathcal{I}_{+,l/r}^-(E_d + m\hbar \omega_{\text{ex}}) \quad (5.30)$$

$${}_0^0 \left[\Sigma_{l/r,0}^{(6)} \right]_1^1 = -i \frac{\hbar \Gamma_{l/r}}{2\pi} \sum_{m=-\infty}^{+\infty} J_m \left(\frac{eV_{l/r}}{\hbar \omega_{\text{ex}}} \right)^2 \mathcal{I}_{-,l/r}^+(E_d - m\hbar \omega_{\text{ex}}) \quad (5.31)$$

$${}_0^0 \left[\Sigma_{l/r,0}^{(7)} \right]_1^1 = i \frac{\hbar \Gamma_{l/r}}{2\pi} \sum_{m=-\infty}^{+\infty} J_m \left(\frac{eV_{l/r}}{\hbar \omega_{\text{ex}}} \right)^2 \mathcal{I}_{+,l/r}^+(E_d - m\hbar \omega_{\text{ex}}) \quad (5.32)$$

$${}_1^1 \left[\Sigma_{l/r,0}^{(8)} \right]_0^0 = -i \frac{\hbar \Gamma_{l/r}}{2\pi} \sum_{m=-\infty}^{+\infty} J_m \left(\frac{eV_{l/r}}{\hbar \omega_{\text{ex}}} \right)^2 \mathcal{I}_{-,l/r}^-(E_d + m\hbar \omega_{\text{ex}}) \quad (5.33)$$

Plugging these rates into Eq. (5.28), and taking into account that $\langle \chi_1 | \rho_\infty | \chi_2 \rangle = \delta_{\chi_1 \chi_2} / 2$,

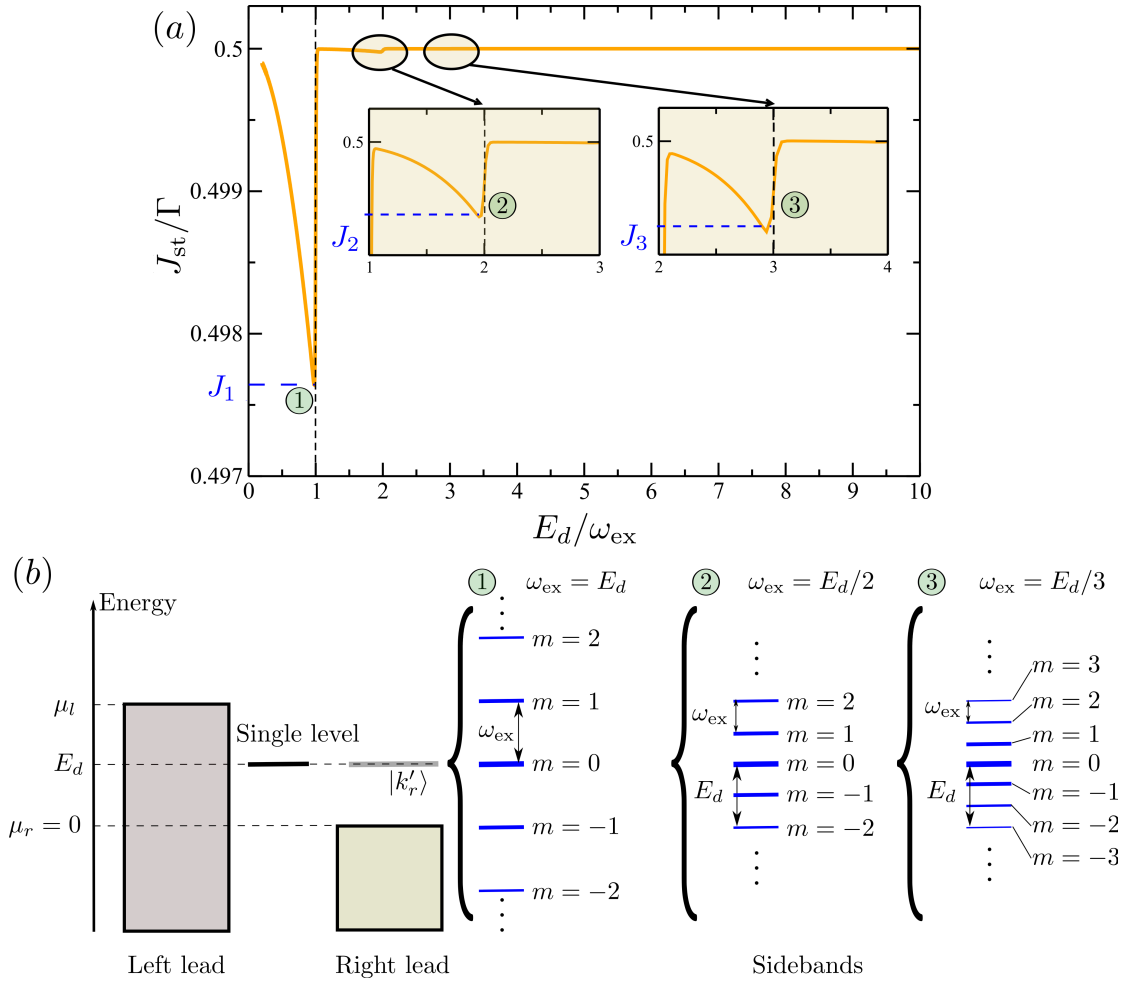


Figure 5.5: (a) Stationary current as a function of the inverse external frequency, with two zooms to the dips in the current for $\omega_{ex} = E_d/2$ and $E_d/3$. Here the energy is measured from the right lead electrochemical potential μ_r and \hbar and e are set to 1. The parameters used in this simulation are: $V_l = V_r = V_0/2 = 0.2E_d$, $\mu_l = 10E_d$, $k_B T = 5 \times 10^{-3}E_d$, and $\Gamma_l = \Gamma_r = \Gamma = 5 \times 10^{-2}E_d$. The insets depict the value for the current J_N [Eq. (5.35)], blue dashed line. It is in good agreement with numerical result for the stationary current at $\omega_{ex} = E_d$. In panel (b), we depict a sketch of the system, a quantum dot coupled to conducting leads, and the sidebands of $|k'_r\rangle$ including the state at resonance with the single level in the quantum dot. The widths of the sketched sidebands indicate their weights given by the m -th Bessel function.

we get to a simple expression for the stationary current

$$I_{\text{st}} = I_l - I_r, \quad \text{with} \quad I_{l/r} = e \frac{\Gamma_{l/r}}{2} \sum_{m=-\infty}^{+\infty} J_m \left(\frac{eV_{l/r}}{\hbar\omega_{\text{ex}}} \right)^2 f_{l/r}^{\pm}(E_d + m\hbar\omega_{\text{ex}}). \quad (5.34)$$

We see that the quantum transport mechanism for nonequilibrium states in the leads involves all the sidebands of the state $|k'_{l/r}\rangle$ at resonance with the single level in the quantum dot. Setting up $\mu_l > E_d > \mu_r$, and considering a weak modulation in the bias voltage $eV_0 \ll \hbar\omega_0$, the current flowing out of the left lead is mainly described by the first sideband, i.e. $I_l \approx \Gamma_l J_0(eV_l/\hbar\omega_{\text{ex}})^2/2 \sim \Gamma_l/2$ [$m = 0$ term in Eq. (5.34)]. For the current from the right lead, only sidebands with energies below the Fermi level play a role in the transport, i.e. the sidebands with modes m where $f_r(E_d - m\hbar\omega_{\text{ex}}) \neq 0$. When the external frequency matches the resonance condition $\omega_{\text{ex}} = (E_d - \mu_r)/N\hbar \equiv \omega_N$, $N = 1, 2, 3, \dots$, the energy of the N -th sideband is on the top of the Fermi sea of the right lead and the current is mainly generated by the sideband and $I_r = \Gamma_r J_{-N}(eV_r/\hbar\omega_N)^2/4$ [see the sketch in Fig. 5.5(b)]. Thus, we can estimate the stationary current at $\omega_{\text{ex}} = \omega_N$ as

$$I_{\text{st}} \approx e \frac{\Gamma_l}{2} - e \frac{\Gamma_r}{4} J_{-N} \left(\frac{eV_0}{2\hbar\omega_{\text{ex}}} \right)^2 \equiv I_N. \quad (5.35)$$

Out of resonance, only higher orders in the sidebands' distribution of the state $|k'_r(t)\rangle$ are relevant in the tunneling process of electrons from/into the right lead, thus producing a significant decrease in the current I_r . In Fig. 5.5(a) we show the current as a function of the inverse of the external frequency. We observe dips in the current corresponding to the process described above.

Chapter 6

Signatures of nonlinearity in driven nanomechanical quantum transport

Fascinating progress has been achieved in downsizing artificially made condensed-matter devices and micromechanical systems are today evolving into nanoelectromechanical systems (NEMS).[5–8] Thereby, the fundamental physical limits set by the laws of quantum mechanics are rapidly approached. The ultimate potential for nanoelectromechanical devices is governed by the ability to detect NEMS motional response to various external stimuli. To realize them in form of transversely vibrating beams, lithographically patterned doubly clamped suspended beams [24, 25, 114–122] are also designed. Also suspended doubly clamped carbon nanotubes display mechanical vibrations [123, 124]. Beyond applications as electrometers,[114, 115, 117] for detecting ultrasensitive forces and displacements,[24, 25] radio-frequency signal processing,[116] as chemical sensors,[125, 126] as ultrasensitive devices used for signal amplification,[127, 128] or for spin detection purpose, [129] the nanomechanical devices also allow to investigate fundamental physical phenomena, see, for instance, Refs. 96 and 97.

In particular, due to their small size, the crossover from the classical to the quantum regime is of interest, where quantum fluctuations in the transverse direction may drastically influence the dynamics.[130–132] The quantum behaviour arises due to a macroscopic number of particles whose coherence is disturbed by the interaction with the environment causing damping and decoherence. Important key experiments on the way to this goal have already been reported in literature.[7, 8, 24–27, 97, 114–124, 133–135]

Most techniques to reveal the quantum behaviour so far address the linear response in form of the amplitude of the transverse vibrations of the nanobeam around its eigenfrequency. The goal is to excite only a few energy quanta in a resonator held at low temperature. To measure the response, the ultimate goal of the experiments is to increase

the resolution of the position measurement to the quantum limit.[24–27] As the response of a damped linear quantum oscillator has the same simple Lorentzian shape as its classical counterpart,[28] a unique identification of the “quantumness” of a nanoresonator in the linear regime can sometimes be difficult.

As transport setups in experimental physics have the advantage that the current-voltage characteristics is rather easily accessible, it is an interesting question to search for nonlinear molecular features here. An important aspect of quantum transport through *molecules* concerns vibrational effects,[136–140] e.g., phonon-assisted transport or nonlinear vibrations. Several works on this topic have appeared in literature. For a comprehensive review of vibrational effects in molecular transport, see Ref. 139. Cizek, Thoss, and Domcke [141] treat the inelastic regime by an electron-molecule scattering theory. Vibrational effects in molecular transistors have also been investigated in a series of papers by the group of Flensberg,[142–145] primarily within the sequential tunneling picture. In Ref. 142, a vibrational mode has been investigated under the assumption of a strong electron-phonon coupling, and rather strong tunneling broadening of the vibrational sidebands has been found. Subsequent work [143] included additional damping of the vibrational mode. The vibrational mode associated with the center-of-mass motion of the molecule was found to couple strongly to the environment and is thus exposed to an effective damping mechanism. In Ref. 144, electrostatic aspects were clarified. Finally, in Ref. 145, the Josephson current through a single level between two superconducting leads with a bosonic environment has been calculated for very weak transmission. A suppression of the supercurrent due to the combined effects of the Coulomb interaction and the environmental fluctuations was reported.

Current-induced nonequilibrium vibrations in single-molecule devices have been investigated in Ref. 146, again in the incoherent regime. The role of light-induced effects on electronic transport has been studied by Hänggi and coworkers.[101] Based on an extension to nonequilibrium situations, semiclassical expansions about the mean-field solutions for the equilibrium case have been used to study transport through a resonant level strongly coupled to a local phonon under nonequilibrium conditions (nonequilibrium local polaron problem).[147] Recently, normal [148] and superconducting [149] transport through a vibrating molecule have already been studied by Keldysh Green’s function schemes perturbative in the electron-phonon coupling. Nonequilibrium phonon dynamics in nanobeams and the related phonon-assisted losses have been investigated in Ref. 150.

In this Chapter we address the problem of detecting quantum coherent multiphonon transitions through current characteristics. We consider a nanobeam in its nonlinear regime clamped to two conducting leads [cf. Fig. 6.1]. For an ac bias voltage applied in the leads, the current mimics a harmonic driving in the nonlinear deflection of the nanobeam, in-

ducing coherent multiphonon transitions. Besides, the electronic states in the leads are split into sidebands defining several tunneling paths for an electron from the left(right) to the right(left) lead. The alternating current requires a difference between the mode of the sidebands involved in the tunneling processes of an electron from/into the left(right) lead. Therefore, the excitation of the mechanical motion of the nanobeam, due to this tunneling process, suppresses the alternating current. Thus, the current exhibits antiresonance behaviour as a consequence of multiphonon transitions in the nanobeam.

6.1 Hamiltonian model

We consider a free hanging nanobeam of length l doubly clamped to two externally driven metallic leads. The leads are at different electrochemical potentials inducing a charge current through the nanobeam. In order to couple the mechanical motion with the electronic transport, a magnetic as well as an electric field are applied. In addition, we allow for a mechanical force $F > 0$ to compress the beam in longitudinal direction [see Fig. 6.1(a)]. Here, for simplicity we assume a sufficiently strong magnetic field in order to consider spinless dynamics only.

The Hamiltonian model is given by

$$H(t) = H_e + H_m + H_l(t) + H_r(t) + H_T, \quad (6.1)$$

where H_e is the Hamiltonian of the electron dynamics in the beam, and H_m describes the mechanical part, $H_{l/r}$ is the Hamiltonian of the left/right lead [see Eq. (5.3)], and $H_T = H_{T,l} + H_{T,r}$ describes the electron tunneling between the leads and the beam from/into the left ($H_{T,l}$) and right ($H_{T,r}$) lead [see Eq. (5.4)]. The electromechanical coupling is not written explicitly in Eq. (6.1). Below, in the description of the electronic dynamics, we shall present this coupling in detail. In the coordinate system introduced in Fig. 6.1 the equilibrium position of the nanobeam is along the x -axis. The external longitudinal compression force F induces a deflection $u(x)$ in direction of the y -axis from the nanobeam's equilibrium position. Because of the external magnetic field and the strong confinement to the beam's reference frame, the kinetic momentum $\mathbf{P}(\mathbf{r}) = -e\mathbf{A}(\mathbf{r})/c$ is evaluated only on the position of the beam $\mathbf{r}_u = (x, u(x), 0)$, $\mathbf{P}(\mathbf{r}) \rightarrow \mathbf{P}(\mathbf{r}_u)$. In the kinetic momentum, e is the electronic charge, c the speed of light, and \mathbf{A} the vector potential, $\mathbf{B} = \nabla \times \mathbf{A}$. Thereby, the electronic part of the Hamiltonian beam reads in second quantization form

$$H_e = \int d^3\mathbf{r} \left[\frac{1}{2m} \psi^\dagger(\mathbf{r}) \left(\frac{\hbar}{i} \nabla_{\mathbf{r}} + \mathbf{P}(\mathbf{r}_u) \right)^2 \psi(\mathbf{r}) \right]. \quad (6.2)$$

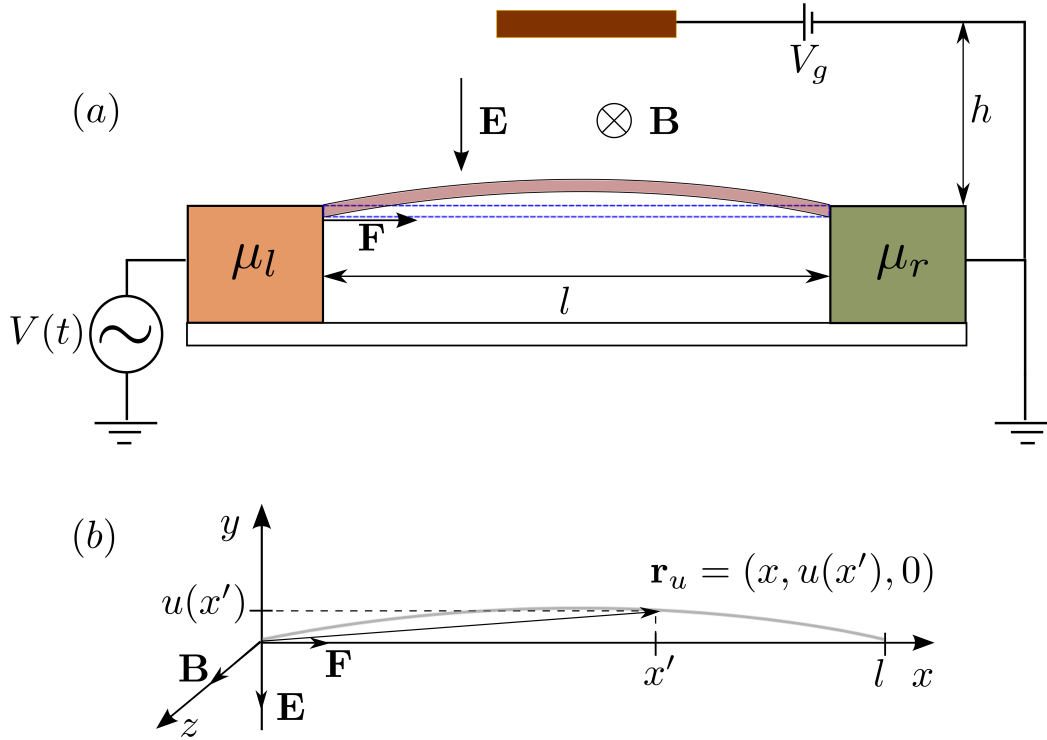


Figure 6.1: (a) Sketch of a free hanging nanobeam of length l clamped to two metallic leads. (b) Description of the beam in point dynamics.

The field operators $\psi^\dagger(\mathbf{r})$, $\psi(\mathbf{r})$ create or annihilate an electron at $\mathbf{r} = (x, y, z)$, respectively, and follow the anti-commutation relation $\{\psi^\dagger(\mathbf{r}), \psi(\mathbf{r}')\} = \delta(\mathbf{r} - \mathbf{r}')$. For simplicity, we assume a magnetic field aligned with the z -axis, yielding the Landau gauge $\mathbf{A}(\mathbf{r}) = -Bye_x$, with $|\mathbf{B}| = B$ and $e_x = (1, 0, 0)$.

The mechanical part of the Hamiltonian model describes bending and compression modelled by [132, 151]

$$H_m = \int_0^l dx \left[\frac{1}{2\rho_b} \pi^2(x) + \frac{EI}{2} u''(x)^2 - \frac{F}{2} \cdot \left(\sqrt{1 - u'(x)^2} - 1 \right) \right], \quad (6.3)$$

where $\pi(x)$ is the momentum density operator, the conjugate generalized coordinate of the deflection $u(x)$. By the correspondence principle $\pi(x)$ and $u(x)$ turn into field operators following the commutation rule $[u(x), \pi(x')] = i\hbar\delta(x - x')$. In Eq. (6.3) ρ_b is the linear mass density of the beam, I the area momentum of inertia, and E the Young's modulus.

We consider the modulation V_0 to be sufficiently strong such that it induces weakly nonlinear deflections in the nanobeam. Thus, the mechanical part of the nanobeam is well

described by an expansion up to the fourth order in $u'(x)$ in the third term on the right hand side in Eq. (6.3), i.e. $\sqrt{1 - u'(x)^2} \approx 1 + u'(x)^2 + u'(x)^4/4$. Moreover, we consider the mechanical dynamics close to the Euler instability, setting $F \rightarrow F_c = EI(\pi/l)^2$, and model the vibrational motion by a single nonlinear mode.

6.1.1 Magneto-elastic coupling

The nanobeam, called the resonator hereafter, induces electronic transport between the conducting leads. Due to the the strong confinement potential, any perturbation in the dynamics of the electrons involved in this process affects directly the mechanical motion (deflections) of the resonator. The introduction of a magnetic and/or electric field therefore leads to electron-phonon interactions. We start in this section by introducing the effects on the dynamics caused by an external magnetic field. We treat the implications related to the electric field in the next section.[96]

In the presence of a magnetic field, and for a finite potential difference between the leads, i.e. leads at different electrochemical potential, the electrons are subject to a Lorentz force which depends on the induced deflection $u(x)$ [see Eq. (6.2)], due to the strong confinement potential. In order to describe explicitly the induced *electron-phonon* coupling by the external magnetic field, the so called magneto-elastic interaction, we resort to the following unitary transformation[96]

$$\mathcal{U}_b(\mathbf{r}) = \exp \left[i \frac{eB}{\hbar c} \left(\int_0^x ds u(s) \right) \psi^\dagger(\mathbf{r}) \psi(\mathbf{r}) \right], \quad (6.4)$$

which changes the frame of reference of the electronic degrees of freedom incorporating the effect of mechanical deflections. The aim is to get a model that describes electron propagation through a double barrier system coupled to conducting leads, where the influence of mechanical deflections is governed by the tunneling Hamiltonian. The transformed Hamiltonian $H'(t) \equiv \mathcal{U}_b(\mathbf{r}) H(t) \mathcal{U}_b^\dagger(\mathbf{r}) = H'_e + H'_m + H'_{T,l/r} + H_l(t) + H_r(t)$ is given by

$$H'_e = -\frac{\hbar^2}{2m} \int d\mathbf{r} \psi^\dagger(\mathbf{r}) \nabla_{\mathbf{r}}^2 \psi(\mathbf{r}), \quad (6.5)$$

$$H'_m = \int_0^l dx \left[\frac{1}{2\rho_b} \left(\pi(x) - \frac{eB}{c} \Theta(x) \psi^\dagger(\mathbf{r}) \psi(\mathbf{r}) \right)^2 + \frac{EI}{2} u''(x) - \frac{F}{2} (u'(x)^2 + u'(x)^4/4) \right], \quad (6.6)$$

$$H'_{T,l/r} = \exp \left[i \frac{eB}{\hbar c} \int_0^l ds u(s) \right] \sum_k \int d^3\mathbf{r} T_{l/r} \psi(\mathbf{r}) c_{k,l/r}^\dagger + h.c., \quad (6.7)$$

with $\Theta(x)$ being the Heaviside function.

In order to keep the model simple, we make some approximations. First, we consider the limit of weak coupling to the leads, where the spacing of energies associated with the motion of electrons along the beam $\delta\epsilon \simeq \pi\hbar v_F/2l$ (v_F being the electrons' Fermi velocity), is much larger than the level broadening due to the coupling to the conducting leads. In addition, in this limit only the first longitudinal state E_d is relevant, yielding the single level Hamiltonian,

$$H'_e \simeq E_d d^\dagger d \quad (6.8)$$

for the electronic part of the beam. Above, d^\dagger (d) creates (destroys) an electron in the resonator.

Further simplifications arise if one restricts the mechanical dynamics to the fundamental bending mode, which expresses the deflection field operator as

$$u(x) = Y_0 u_0(x/l)(b^\dagger + b)/\sqrt{2}, \quad (6.9)$$

where $u_0(x)$ is the normalized profile of the fundamental mode bending mode, $Y_0 = (3\hbar^2 l^2 F_c / ((F_c - F)\rho_b EI))^{1/4} / 2\pi$ is the amplitude of zero point fluctuation in the fundamental mode, and b^\dagger , b are the creation and annihilation boson operators, respectively. Thus, the mechanical part of the Hamiltonian is given by a quantum harmonic oscillator model with a Kerr nonlinearity

$$H'_m = \hbar\omega_0 b^\dagger b + \hbar^2\nu(b^\dagger + b)^4/12. \quad (6.10)$$

In addition to this term, there are constant contributions from the electronic occupation of the leads and the single electronic level of the resonator, which can be systematically rescaled and therefore excluded in the final result [96, 152]. In Eq. (6.10)

$$\omega_0 = 4 \left(\frac{\pi}{l}\right)^2 \left[\frac{EI}{3\rho_b} \cdot \frac{F_c - F}{F_c} \right]^{1/2} \quad \text{and} \quad \nu = \frac{4F_c - F}{lEI\rho_b} \cdot \frac{F_c}{F_c - F} \quad (6.11)$$

are the fundamental frequency of the bending mode and the Kerr nonlinearity, respectively.

The tunneling terms [Eq. (6.7)], which includes the magnetic-elastic coupling, read

$$H'_{T,l/r} = \exp[i\lambda_{\text{mag}}(b^\dagger + b)] \sum_k T_{l/r} d c_{k,l/r}^\dagger + h.c., \quad \text{with} \quad \lambda_{\text{mag}} = \frac{eB Y_0 l}{\hbar c \sqrt{2}} \int_0^1 ds u_0(s). \quad (6.12)$$

6.1.2 Polaron coupling

So far, we have treated the nanobeam in presence of an external magnetic field transversally applied to its plane of vibration. In this section we introduce the implications of the external

electric field in the mechanical dynamics of the resonator. We consider an electric field in the same direction of the nanobeam deflections, i.e., in the direction of y -axis in Fig. 6.1. In the following we consider the derivation presented in Ref. 152.

For the creation of an external electric field, we consider an antenna with a gate voltage V_g , placed at a certain distance h from the nanobeam. The electric field can therefore be tuned by h and V_g . The electric field causes negative charges to collect on the nanobeam and positive charges on the antenna forming a capacitor of capacitance C_g (gate capacitance).

When the nanobeam is deflected from its equilibrium position by the external force F , the geometry of the capacitor changes, thus inducing a variation in the capacitance $C_g = C_g[u(x)]$. That is why the storage energy in the capacitor depends on the mechanical dynamics. This effect is described quantitatively by the electrostatic Hamiltonian[153]

$$H_{\text{elec}} = \frac{e^2 N^2}{2C_g[u(x)]} - eV_g N, \quad (6.13)$$

where N is the operator for the total number of electrons in the beam. Since we assume that only a single electronic level contributes to transport, it is possible to write $N = N_0 + d^\dagger d$, where $N_0 \approx C_g V_g / e$ is the number of the excess electrons in the filled levels and $d^\dagger d$ the number of electrons in the relevant level.

For small deflections of the beam we can express $C_g[u(x)]$ in terms of $(b^\dagger + b)$ as

$$C_g[u(x)] \approx C_g[0] (1 - a_0(b^\dagger + b)), \quad (6.14)$$

where

$$a_0 = \frac{Y_0}{l\sqrt{2}} \int_0^l ds \frac{1}{C_g[0]} \frac{\partial C_g}{\partial u}[0] u_0(s/l). \quad (6.15)$$

Plugging Eq. (6.14) into Eq. (6.13) one obtains

$$H_{\text{elec}} = \frac{U_\infty}{2} a_0 (b^\dagger + b) + (\tilde{\epsilon} - eV_g) d^\dagger d + H_{\text{pol}}, \quad (6.16)$$

where $U_\infty = e^2 / C_g[0]$, $\tilde{\epsilon} = U_\infty (N_0 + 1/2)$, and

$$H_{\text{pol}} = \lambda_{\text{elec}} (b^\dagger + b) d^\dagger d, \quad \text{with} \quad \lambda_{\text{elec}} = a_0 \tilde{\epsilon}. \quad (6.17)$$

The first term in Eq. (6.16) gives a shift in the equilibrium position of the resonator and can be discarded. Furthermore, we assume U_∞ to be the largest energy scale of the system, allowing to neglect the contribution of the double occupancy state. The second term can be included in the definition of E_d leading to a renormalization of the level energy. The last term, defined in Eq. (6.17), is a polaron-like coupling, which models the interaction between the oscillations and the charge fluctuations in the dot.

The expression for the polaronic coupling constant λ_{elec} can be calculated by using a model of distributed capacitance[153, 154]

$$C_g[u(s)] = \int_0^l ds \frac{2\pi\epsilon_0}{\cosh^{-1}([h - u(s)]/R_0)}, \quad (6.18)$$

where h is the distance of the nanobeam from the antenna, R_0 is the nanobeam radius, and ϵ_0 is the vacuum permittivity. Plugging Eq. (6.18) in the definition of the coupling strength λ_{elec} [see Eq. (6.17)] one obtains, for $R_0 \ll h$,

$$\lambda_{elec} \approx \frac{eC_g[0]|V_g|Y_0}{\sqrt{2}2\pi\epsilon_0 h l^3} \int_0^1 ds u_0(s), \text{ for } C_g[0]V_g \gg e. \quad (6.19)$$

Thus, the total Hamiltonian including the electrostatic contribution, reads

$$H'(t) + H_{elec} \approx E_d d^\dagger d + H'_m + H_{pol} + H_l(t) + H_r(t) + H'_T, \quad \text{with } E_d = \epsilon + \tilde{\epsilon} - eV_g. \quad (6.20)$$

In the absence of magneto-elastic coupling, the Hamiltonian (6.20) was introduced in Refs. 155 and 156 to describe transport through a quantum dot in the presence of a local electron-phonon coupling and later studied by several authors.[143, 157–161]

In the linear case, $\nu = 0$ in Eq. (6.10), the Hamiltonian is diagonalized by the polaron transformation $\mathcal{U}_{pol} = \exp[\lambda_{elec}(b^\dagger - b) d^\dagger d / \omega_0]$. By using the transformation \mathcal{U}_{pol} we shift the bosonic fields b and b^\dagger by $-\lambda_{elec}/\omega_0$, i.e. $\mathcal{U}_{pol} b \mathcal{U}_{pol} = b - \lambda_{elec}/2\omega_0$. In the regime of very weak nonlinearity and weak polaronic coupling, $\{\nu/\omega_0, \lambda_{elec}\} \ll 1$, the transformed mechanical part of the Hamiltonian (6.20), $\mathcal{U}_{pol} H'_m \mathcal{U}_{pol}^\dagger$, can be approximated by

$$H''_m = \mathcal{U}_{pol} H'_m \mathcal{U}_{pol}^\dagger \approx \hbar\omega_0 b^\dagger b + \hbar^2\nu(b^\dagger + b)^4/12 - \lambda_{elec}(b^\dagger + b) d^\dagger d \quad (6.21)$$

The third term on the right hand side in Eq. (6.21) vanishes with the polaronic coupling H_{pol} term of the Hamiltonian (6.20). In addition, as a consequence of the transformation \mathcal{U}_{pol} , the single level energy on the dot is modified by $E'_d = E_d - \lambda_{elec}^2\omega_0$, the charging energy by $U'_\infty = U_\infty - 2\lambda_{elec}\omega_0$, and the fermion operators by $d \rightarrow d \exp[\lambda_{elec}(b - b^\dagger)]$. The \mathcal{U}_{pol} transformation translates the polaronic coupling to the tunneling term in the Hamiltonian. In this way one can combine the electrostatic and magnetic effects in the the electron-phonon dynamics in the tunneling term. Using the Baker-Hausdorff formula, the transformed tunneling part of the Hamiltonian reads

$$H''_{T,l/r} \equiv \mathcal{U}_{pol} H'_{T,l/r} \mathcal{U}_{pol}^\dagger = \exp[\alpha b - \alpha^* b^\dagger] \sum_k T'_{l/r} d c_{k,l/r}^\dagger + h.c., \quad (6.22)$$

where $T'_{l/r} = T_{l/r} \exp[-i\lambda_{elec}\lambda_{mag}]$ are the normalized tunneling matrix elements, and $\alpha = \lambda_{elec} + i\lambda_{mag}$ is the complex electron-phonon coupling.

Finally, one gets the following Hamiltonian model

$$H''(t) = E'_d d^\dagger d + H'_m + H_l(t) + H_r(t) + H''_T, \quad (6.23)$$

where the electron-phonon interaction, induced by external magnetic and electric fields, is enclosed in the tunneling term H''_T [Eq. (6.22)]. The Hamiltonian (6.23) is limited to the special case where the polaron coupling defines a time regime larger than the decay time of the electrons in the single level, i.e., $1/\omega_0 \lambda_{elec} \gg 1/\hbar\Gamma$. This is a significant restriction for the size of the external electric field. In order to keep the system as simple as possible and to give a straightforward interpretation of the results, we shall consider only a magneto-elastic coupling between the electron and phonons.

6.2 Current driving the mechanical motion

In this section we consider a time-periodic bias voltage in the leads at frequency ω_{ex} with amplitude $V_{l/r} = \pm V_0/2$. In analogy with Sec. 5.4.2, it is more convenient to change to the reference frame of time independent bias voltages by using the transformation [cf. (5.5)]

$$\mathcal{U}_V(t) = \exp [i \phi_l(t) + (l \rightarrow r)], \quad \text{with} \quad \phi_{l/r}(t) = \frac{eV_l}{\hbar\omega_{ex}} \sum_k \sin(\omega_{ex}t) c_{k,l}^\dagger c_{k,l}. \quad (6.24)$$

In doing so, the tunneling matrix elements $T_{l/r}$ in the tunneling term become time-dependent involving the phase accumulated by the modulation $\phi_{l/r}(t)$, i.e., $T'_{l/r}(t) = T_{l/r} \exp[i\phi_{l/r}(t)]$. This yields the tunneling Hamiltonian

$$H_{T,l/r}(t) = \exp [i\lambda(b^\dagger + b)] \sum_k T'_{l/r}(t) d c_{k,l/r}^\dagger + h.c. . \quad (6.25)$$

The Hamiltonian of the leads thereby becomes time-independent, i.e., $H_{l/r}(t) \rightarrow H_{l/r}$. In Eq. (6.25), we drop out the primes symbols and redefine the magneto-elastic coupling as $\lambda \equiv \lambda_{mag}$ in order to simplify the notation. The other elements in (6.23), $E'_d d^\dagger d$ and H'_m , are invariant under $\mathcal{U}_V(t)$.

We are interested in studying coherent few-phonon transitions in the nanobeam when the external frequency is close to the fundamental frequency $\omega_{ex} \sim \omega_0$. Furthermore, we focus on the regime of weak nonlinearity and weak driving, characterized by $\{\hbar^2\nu/\omega_0, eV_0/\omega_0, \lambda\} \ll 1$. In this limit, it is more convenient to switch to the rotating frame $R(t) = \exp[-i\hbar\omega_{ex}(b^\dagger b + d^\dagger d)t]$, and eliminate the fast oscillating terms in a rotating wave approximation. Thus we get to the following tunneling term

$$\mathcal{H}_{T,l/r} = e^{\lambda^2/2} T_{l/r} \sum_k \sum_{m=-\infty}^{\infty} B_m J_{1-m} \left(\frac{eV_{l/r}}{\hbar\omega_{ex}} \right) d c_{k,l/r}^\dagger + h.c. , \quad (6.26)$$

where B_m is a Franck-Condon operator defined by [157, 162]

$$\begin{aligned} B_m|n\rangle &= \sum_{k=|m|\Theta[-m]}^{\infty} \frac{(i\lambda)^{m+2k}}{(k+m)!k!} (b^\dagger)^{k+m} b^k |n\rangle \\ &= (i\lambda)^{|m|} \sqrt{\frac{(n-|m|\Theta[-m])!}{(n+|m|\Theta[m])!}} L_m^{n+|m|\Theta[-m]}(\lambda^2) |n+m\rangle, \end{aligned} \quad (6.27)$$

where $b^\dagger b|n\rangle = n|n\rangle$, $\Theta(x)$ is the Heaviside function, and $L_m^n(x)$ are the generalized Laguerre polynomials. The Bessel functions in (6.27) provide extra driving-induced weights in the expansion, making the first terms $m = 0, 1$ in Eq. (6.26) dominant. To proof this, we consider the upper limit of $\langle n+m|B_m(\lambda^2)J_{m-1}(V_{l/r}/\hbar\omega_{\text{ex}})|n\rangle \equiv \mathcal{A}_{n+m,n}$ in order to compare the different matrix elements of $\mathcal{H}_{T,l/r}$, and then determine the dominant elements in Eq. (6.26). For $V_{l/r} \ll \omega_0$ this is given by [163]

$$|\mathcal{A}_{n+m,n}| \leq \lambda^{|m|} \sqrt{\frac{(n-|m|\Theta[-m])! \Gamma[n+m(1+\Theta[-m])]}{(n+|m|\Theta[m])! m! \Gamma[n+m\Theta[-m]]}} \frac{e^{\lambda^2/2} (\lambda/2)^{m-1}}{\Gamma[m]}, \quad (6.28)$$

where, $\Gamma(x)$ is the Gamma function. Even for $\lambda = 0.1$, [152] $|\mathcal{A}_{n+m,n}|/|\mathcal{A}_{n+1,n}| \ll 1$ for $m \neq \{0, 1\}$. The relative contribution of the m -th ($m \neq 0, 1$) term in (6.26) in the energy in perturbation theory is even smaller, meaning that the tunneling can safely be approximated by

$$\mathcal{H}_{T,l/r} \cong \sum_k \left(\frac{eV_{l/r}}{2\hbar\omega_{\text{ex}}} + i\lambda b^\dagger \right) d c_{k,l/r}^\dagger + h.c., \quad (6.29)$$

using the approximations $J_0(x) \approx 1$, $J_1(x) \approx x/2$ for $x \ll 1$, and $B_0 \approx \mathbb{I}$, $B_1 = i\lambda b^\dagger$ for $\lambda \ll 1$. Under these approximations, the resulting RWA Hamiltonian reads

$$\mathcal{H} = \mathcal{H}_M + \mathcal{H}_E \quad (6.30)$$

where

$$\mathcal{H}_M = \hbar\delta\omega b^\dagger b + \frac{\hbar^2\nu}{2}(b^\dagger b + 1)b^\dagger b + i\lambda \left[\left(b^\dagger \sum_k T_l d c_{k,l}^\dagger - h.c. \right) + (l \rightarrow r) \right], \quad (6.31)$$

and

$$\mathcal{H}_E = \delta\epsilon d^\dagger d + H_l + H_r + \left[\sum_k \left(\frac{eV_l}{2\hbar\omega_{\text{ex}}} T_l d c_{k,l}^\dagger + h.c. \right) + (l \rightarrow r) \right], \quad (6.32)$$

with $\hbar\delta\omega = \hbar(\omega_0 - \omega_{\text{ex}})$ and $\delta\epsilon = E'_d - \omega_{\text{ex}}$ being the characteristic energy of the mechanical and electronic dynamics detuned by the external driving, respectively. As in Chapters 3 and 4 the external modulation, in this case the operator $i\lambda T_l d c_{k,l/r}^\dagger$, lifts the degeneracies at $\delta\omega = \delta\omega_N = \nu(N+1)/2$, $N \in \mathbb{Z}$, inducing coherent multiphonon transitions between states $|n\rangle$ and $|N-n\rangle$ in the resonator.

6.2.1 Nonlinear signatures in the current characteristics

The nonequidistant structure of the energy spectrum of the nonlinear resonator defines several resonant frequencies. Its energy levels E_n with $n \leq N$ are pairwise resonant for the same driving frequency ω_{ex} , $E_{N-n} - E_n = (N - 2n)\hbar\omega_{\text{ex}}$. After preparing the resonator in its n -th excited state $n \leq N$, it displays periodic quantum oscillations between the n -th and the N -th excited states. These oscillations may be referred to as multiphonon Rabi oscillations.

Close to the resonance $\delta\omega = \delta\omega_N$, the relevant states in the dynamics of the resonator are those involved in the multiphonon transitions, $|n\rangle$ and $|N - n\rangle$. The matrix representation of the Hamiltonian can be written in terms of 2×2 blocks corresponding to the subspaces formed by $|n\rangle$ and $|N - n\rangle$, $0 < n < N/2$. In the $(n + 1)$ -th block, $0 < n < N/2$, corresponding to the $N - n$ multiphonon transition, the degeneracy is lifted at order $N - 2n$ in perturbation theory in $\lambda T_{l/r}/\nu$. Therefore the diagrammatic expansion in leading order of Γ , developed in Chap. 5 for driven systems, is sufficient to describe only one phonon transitions, i.e. for $N - 2n = 1$, which implies only transitions for odd N .

In Fig. 6.2(a), the amplitude of the nonlinear response exhibits anti-resonances at $\delta\omega = \delta\omega_N$ for odd N , indicating single phonon transitions. In contrast, the amplitude of the alternating current, Fig. 6.2(b) exhibits anti-resonance behaviour at $\delta\omega_N$ for every N . Since the amplitude of the alternating current vanishes when the nonlinear oscillator gets excited, the backaction on the nanobeam leads to a decrease in the nonlinear response [see the zoom for the 3-phonon resonance in the upper panel of Fig. 6.2(c)].

The nonequilibrium behaviour of the nonlinear resonator is best described by the amplitude of the alternating current. The current calculated using the Hamiltonian in the RWA [Eq. (6.30)] is composed of a direct current and an alternating current. We can identify a part of the direct component from the electronic part of the Hamiltonian, Eq. (6.32), which is just the current from the first sideband flowing through the quantum dot. From Eq. (5.34) we can estimate this part as $I_{dc} \approx \Gamma_l J_1 (eV_l/\hbar\omega_{\text{ex}})^2/2$. In Fig. (6.2)(b) we have subtracted this dc component from the total current calculated using (6.30). The remaining part corresponds entirely to the dynamics of the coupled system. In doing so, we can estimate the current around the N -th multiphonon resonance. Taking into account only the relevant states $|n\rangle$ and $|N - n\rangle$, $0 < n < N/2$, and the renormalization of the tunneling matrix elements, see Eq. (6.32), yielding $\Gamma_{l/r} \rightarrow \Gamma_{l/r} (eV_0/4\hbar\omega_{\text{ex}})^2$, we calculate the self energies $[\Sigma_{l/r}^{(5/6)} + \Sigma_{l/r}^{(8/7)}]$, and therefore the current around the N -th multiphonon resonance [using Eq. (5.29)] and find

$$I_{ac}^N \approx e\Gamma \left(\frac{eV_0}{4\hbar\omega_{\text{ex}}} \right)^2 \sum_{n=0}^{\lfloor N/2 \rfloor} \sum_{s=0,1} (\rho_{ns,ns}^\infty - 1/2N^*), \quad \Gamma_{l/r} = \Gamma, \quad (6.33)$$

where $\rho_{ns,ns}^\infty$ are the diagonal elements of the reduced density operator in the steady state regime. In this regime n refers to the mechanical state, s to the electronic state, and N^* is the number of effective states considered in the simulations, which corresponds to the number of states enclosed in the difference of the electrochemical potentials in the leads, i.e., $N^* = \lfloor |\mu_l - \mu_r| / \hbar\omega_{\text{ex}} \rfloor$. Additionally, we have used $\rho_{(N-n)s,(N-n)s}^\infty = \rho_{ns,ns}^\infty$. In the lower panel of Fig. 6.2(c) we show the approximation (6.33) by the black solid line and the current calculated using the full numerical method (red solid line). A good agreement is found.

6.3 Conclusions

To conclude, we have investigated nonlinear mechanical features in the current characteristics of a doubly-clamped nanobeam in its nonlinear regime connected to fermionic reservoirs. We have considered the special case of a nanobeam in the presence of an external magnetic field. In leading order of the magneto-elastic coupling, the current flowing through the nanobeam mimics a harmonic driving in its nonlinear deflections. In the regime of resonant few-phonon transitions (deep quantum regime), discrete multiphonon resonances in the resonator can be identified as anti-resonances in the alternating current amplitude.

The nonlinear response calculated by means of second order in the tunneling coupling in the diagrammatic expansion, only describes single-phonon transitions. In order to connect the nonlinear response to multiphonon transition, we have to consider higher terms in the diagrammatic expansion. On the other hand, in the alternating current amplitude the second order in diagrammatic expansion in the tunneling coupling is sufficient to describe all the multiphonon transitions and the antiresonant lineshape is a clear signature of the nonlinearity in the nanobeam.

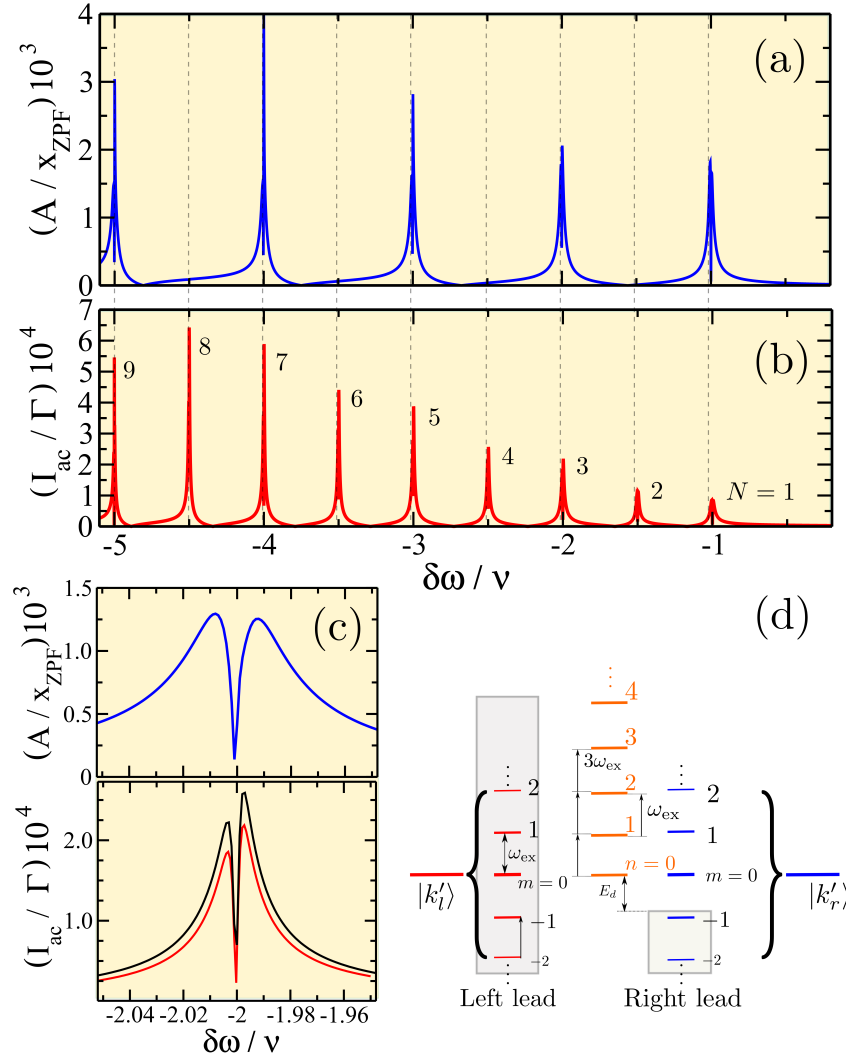


Figure 6.2: (a) Amplitude of the nonlinear response of the vibrational mode to the external current (driving) as a function of the external frequency. (b) Alternating current as a function of the external frequency. (c) Zoom of the nonlinear response (upper plot), and the amplitude of the alternating current (lower plot) at the 3-phonon transition. (d) Sketch of the energy spectrum of the system and the sidebands of $|k'_{l/r}\rangle$ on the left/right lead, for $\delta\omega = \delta\omega_3$. There, we compare the approximation described in Eq. (6.33) (black solid line) with the full numerical result (red solid line). The parameters used are: $\lambda = 10^{-3}$, $\nu = 10^{-2}\omega_0$, $\Gamma_l = \Gamma_r = \Gamma = 5 \times 10^{-2}\omega_0$, $V_0 = 4 \times 10^{-1}\omega_0$, $E_d = 3\omega_0/2$, $k_B T = 5 \times 10^{-3}\omega_0$, $\mu_l = 10\omega_0$, and $\mu_r = 0$.

Summary

In this thesis the quantum noise properties of the driven nonlinear oscillators under nonequilibrium conditions is studied in different physical situations.

We first consider a Duffing oscillator in the deep quantum regime being a monostable anharmonic oscillator which has a Kerr nonlinearity. In this system, we analyse the power spectrum of the photon number fluctuations induced by the coupling of the system to a dissipative environment. In the weak coupling regime of the environment, a weak Kerr nonlinearity, a weak amplitude modulation, and close to resonance we resort to the rotating wave approximation to solve the dissipative dynamics by solving the Lindblad quantum master equation and thereafter calculating the noise by means of the regression theorem. Both analytical and numerical calculations are presented, revealing a rich phenomenology. Most interestingly, we find that the dynamics of the photon number fluctuations is characterized by multiphoton oscillations which manifest themselves as peaks in the noise spectrum $S(\omega)$ of photon number. The peak intensity is proportional to the stationary occupation probability of the initial quasienergy state. Therefore, the noise spectrum offers a convenient way to directly probe the stationary distribution over all the quasienergy states. Exactly at a multiphoton resonance, the noise spectrum consists in a collection of pairs of related resonances which are located at opposite frequencies and which are equal in height. Each pair is associated to a multiphoton doublet. In spite of large fluctuations over the oscillator quasienergy, no quasielastic peak occurs at zero frequency. Finally, for a weakly detuned modulation or a stronger driving, the spectrum becomes asymmetric. Besides, an additional quasielastic peak appears at zero frequency which represents incoherent relaxation of the fluctuations towards the stationary state. The two inelastic peaks are symmetrically located at finite frequencies and their width determines the inverse of the dephasing time. In addition, the quasielastic peak at zero frequency represents incoherent relaxation with the inverse relaxation time given by its width. In the driven system, the appearance of a

quasielastic peak depends on the intriguing interplay between the nonlinearity, the driving strength and the dissipation strength characterizing a full nonequilibrium situation.

In the aforementioned regime, we use the Duffing oscillator as amplifier of the quantum state of a qubit. There, we exploit sharp multiphoton resonances in the nonlinear oscillator in the detection/amplification of the states of the qubit. This concept is an extension of the case of a linear resonator. We find that the sharp resonant lines offer the advantage that only a few measurement cycles are necessary to ensure a large discrimination power of the measurement. Moreover, we calculate the relaxation rate of the qubit due to the coupling with the Duffing oscillator around a multiphoton resonance. Notably, the back-action of the resonator on the qubit is sufficiently weak, yielding to a good qubit-state measurement fidelity.

Finally, in the pursuit of a detection scheme for the multiphoton(phonon) transitions in the Duffing oscillator, we study the electric charge current flowing through a nanobeam, in its nonlinear regime, clamped to conducting leads. We start with the calculation of the electron-phonon interaction, considering the general case of a nanobeam in presence of an electric and magnetic field. For the sake of simplicity, we consider the magnetic field case, taking into account that the contribution from the electric field is just an imaginary part in the coupling constant. We find that in the driven case, for ac bias voltages in the leads, and in leading order in the coupling constant, the current drives directly the deflection of the nanobeam. In order to compute observables of interest we apply a real-time diagrammatic expansion in the tunneling coupling, leading to master equation for the reduced density matrix. In the high frequency approximation, and combining this with the rotating wave approximation, we calculate the current flowing through the nanobeam. The ac part shows characteristic antiresonant behaviour as a consequence of the multiphonon transition transition in the nanobeam.

Second-order coherence function

Intensity-correlation experiments have provided powerful tools especially in astronomy, since they allow the determination of the angular diameter of distant stars.[164, 165] The first experiment was conducted by Hanbury-Brown and Twiss.[166] The measured quantity is the joint probability of counting a photon at time t and another at $t + \tau$. This probability is, according to Glauber,[167] proportional to the normal-ordered correlation function

$$G^{(2)}(\tau, t) = \langle : \hat{n}(t)\hat{n}(t + \tau) : \rangle, \quad (\text{A.1})$$

where $n(t) = a^\dagger(t)a(t)$ is the number operator at time t , and the double dots describe normal ordering in the ladder operators $a(t)$ and $a^\dagger(t)$. In a stationary situation, the $G^{(2)}$ function depends only on the delay time τ . On the other hand, for nonequilibrium states, since the lack of the translational time invariance in the dynamics the $G^{(2)}$ function, therefore, depends on the initial time t . [51] In the steady state regime, for long times, the state of the system does not depend on its initial preparation, and so $G^{(2)}(\tau, t \rightarrow \infty) = G^{(2)}(\tau)$. In the following we consider this regime.

The second order of coherence function is defined as[2]

$$g^{(2)}(\tau) = G^{(2)}(\tau) / \langle \hat{n} \rangle_\infty^2. \quad (\text{A.2})$$

This quantity describes whether the photons in the beam tend to group together or stay apart. If $g^{(2)}(\tau) = 1$, the probability of joint detection coincides with the probability of independent detection. This should be the case when $\tau \rightarrow \infty$, since then the memory of the first photodetection dies out. If $g^{(2)}(\tau) > g^{(2)}(0)$, the probability of detecting the second photon increases with the time delay, which is characteristic of antibunching.

For a single-mode photon field, one has

$$g^{(2)}(0) = \langle a^\dagger a^\dagger a a \rangle_\infty / \langle a^\dagger a \rangle_\infty^2. \quad (\text{A.3})$$

If the mode is in a coherent state, we have $g^{(2)}(0) = 1$. On the other hand, for a Fock state $|n\rangle$, in which $a^\dagger a|n\rangle = n|n\rangle$, one has

$$g^{(2)}(0) = 1 - 1/n, \quad (\text{A.4})$$

while for $n = 0$ or $n = 1$, one finds trivially that $g^{(2)}(0) = 0$.

For classical light fields, applying the Schwarz inequality in the classical correlation function corresponding to Eq. (A.2) shows that one should always have $g^{(2)}(\tau) \leq g^{(2)}(0)$. Additionally for these fields we have $g^{(2)}(0) \geq 1$, so that classical fields are never antibunched. Therefore, the two properties $g^{(2)} < 1$ and $g^{(2)}(\tau) > g^{(2)}(0)$ are characteristic of nonclassical light [an example of the first property is provided by Eq. (A.4)]. Since $g^{(2)}(\tau) \rightarrow 1$ when $\tau \rightarrow \infty$, the property $g^{(2)}(0) < 1$ always implies that there is antibunching for some range of values of τ ; unless $g^{(2)}(\tau)$ is independent of τ .

The relation between antibunching and sub-Poissonian statistics is a subtle one [168, 169] In fact, from Eq. (A.3), one can show the following relation between the second order of coherence and the photon number variance:

$$g^{(2)}(0) = 1 + \frac{\langle \Delta \hat{n} \rangle_\infty - \langle \hat{n} \rangle_\infty}{\langle \hat{n} \rangle_\infty^2}. \quad (\text{A.5})$$

Therefore, in this case sub-Poissonian statistics implies $g^{(2)}(0) < 1$, which, unless $g^{(2)}(\tau)$ does not depend on τ , implies antibunching for some range of τ . On the other hand, one cannot state in general that antibunching leads to sub-Poissonian statistics, since $g^{(2)}(\tau) > g^{(2)}(0)$ does not necessarily imply $g^{(2)}(0) < 1$. [170] In fact, for a stationary field the variance of the number of photons measured can be expressed in terms of $g^{(2)}(\tau)$ in the following way [169, 170]

$$\langle \Delta \hat{n}^2 \rangle_\infty - \langle \hat{n} \rangle_\infty = \frac{\langle \hat{n} \rangle_\infty}{T} \int_{-T}^{+T} d\tau (T - |\tau|) [g^{(2)}(\tau) - 1]. \quad (\text{A.6})$$

If $g^{(2)}(\tau) < 1$ for all τ , the field will exhibit sub-Poissonian statistics. One could have, however, $g^{(2)}(\tau) > g^{(2)}(0)$, while still having super-Poissonian statistics for some time interval. Furthermore, for a single monochromatic mode, $g^{(2)}(\tau)$ does not depend on τ , and coincides with the value for $\tau = 0$. In this case, $g^{(2)}(0) < 1$ does not imply antibunching for any counting interval, since neither short or long time intervals between photons are favoured. [170]

Density matrix of the steady state around resonance

In this appendix we compute the stationary solution of the quantum master equation (2.50) following Ref. 47. Using the balance equation (3.12), and the general order solution for the quasienergies states given in (3.15). The expressions for the rates read

$$\begin{aligned}
 W_{0,1} &= W_{0,N-1} = \frac{\gamma}{2} \cos^2 \frac{\theta}{2} \\
 W_{N,1} &= W_{N,N-1} = \frac{\gamma}{2} \sin^2 \frac{\theta}{2} \\
 W_{1,0} &= W_{N-1,0} = \frac{\gamma}{2} N \sin^2 \frac{\theta}{2} \\
 W_{1,N} &= W_{N-1,N} = \frac{\gamma}{2} N \cos^2 \frac{\theta}{2}.
 \end{aligned} \tag{B.1}$$

with $\theta = \tan^{-1}[\Omega_{0,N}/N(\delta\omega - \delta\omega_N)]$. With these elements, the master equation becomes

$$\begin{aligned}
 0 &= -N \sin^2 \frac{\theta}{2} \rho_{00}^\infty + \cos^2 \frac{\theta}{2} \rho_{11}^\infty \\
 0 &= -N \cos^2 \frac{\theta}{2} \rho_{NN}^\infty + \sin^2 \frac{\theta}{2} \rho_{11}^\infty.
 \end{aligned} \tag{B.2}$$

Thereby, the stationary solution reads

$$\begin{aligned}
 \rho_{NN}^\infty &= \rho_{00}^\infty \tan^4 \frac{\theta}{2} \\
 \rho_{11}^\infty &= \rho_{00}^\infty N \tan^2 \frac{\theta}{2}.
 \end{aligned}$$

With these matrix elements one can calculate ρ_{nn}^∞ for $1 \leq n < N/2$. Plugging the quasienergies states (3.8) into the expression for the transition rates in Eq. (3.13), one finds that

most of the transition rates between two different states belonging to two different resonant pairs are zero, except for

$$\begin{aligned} W_{n,n+1} &= W_{n,N-n} = W_{N-n,n+1} = W_{N-n,N-n-1} = \frac{\gamma}{4}(n+1) \\ W_{n+1,n} &= W_{n+1,N-n} = W_{N-n-1,n} = W_{N-n-1,N-n} = \frac{\gamma}{4}(N-n) . \end{aligned} \quad (\text{B.3})$$

The driving field excites the transition from $|0\rangle$ to $|N\rangle$ while the bath generates transitions between the Fock states towards lower energies according to $|N\rangle \rightarrow |N-1\rangle \rightarrow \dots \rightarrow |0\rangle$ when only spontaneous emission is considered. Thereby, the ration of the occupation numbers of two states belonging to two neighbouring resonant pairs is simply given by the ration of the corresponding transition rates according to

$$\begin{aligned} \rho_{nn}^\infty &= \rho_{N-n,N-n}^\infty \\ \frac{\rho_{nn}^\infty}{\rho_{n+1,n+1}^\infty} &= \frac{W_{n,n+1}}{W_{n+1,n}} = \frac{n+1}{N-n} , \quad \text{for } 1 \leq n < N/2 , \end{aligned} \quad (\text{B.4})$$

with this one can calculate all the matrix elements of ρ^∞ , starting with ρ_{11}^∞ and ρ_{NN}^∞ , in terms of ρ_{00}^∞ .

Semiclassical approximation in the Duffing oscillator dynamics

The Hamiltonian of the Duffing oscillator in the rotating wave approximation is given by

$$\mathcal{H} = \delta\omega\hat{n} + \frac{\nu}{2}\hat{n}(\hat{n} + 1) + \frac{f}{2}(a + a^\dagger). \quad (\text{C.1})$$

There, $\delta\omega$ describes the frequency detuned by the external driving, ν the nonlinearity parameter, f the driving strength, a and a^\dagger the ladder operators with $\hat{n} = a^\dagger a$.

In order to obtain a semiclassical treatment following Ref. 75, we introduce the rescaled coordinate and momentum of the oscillator in the rotating frame (quadratures in the static frame) as

$$\mathcal{X} = \sqrt{\frac{\lambda}{2}}(a^\dagger + a), \quad \mathcal{P} = i\sqrt{\frac{\lambda}{2}}(a^\dagger - a), \quad (\text{C.2})$$

with the commutator $[\mathcal{X}, \mathcal{P}] = -i\lambda$, with $\lambda = \nu/2\delta\omega$ being an effective Planck constant. By substituting Eq. (C.2) into the Hamiltonian Eq. (C.1) one obtains

$$\mathcal{H} = \left(\frac{2\delta\omega^2}{\nu}\right) \left(Q(\mathcal{X}, \mathcal{P}) - \frac{1}{4} - \frac{\nu}{8}\right) \quad (\text{C.3})$$

with

$$Q(\mathcal{X}, \mathcal{P}) = \frac{1}{4}(\mathcal{X}^2 + \mathcal{P}^2 - 1)^2 + \beta\mathcal{X} \quad (\text{C.4})$$

as the quasienergy surface, which depends only on the parameter $\beta = f^2\nu/4\delta\omega^3$. The quasienergy surface has the shape of a tilted Mexican hat [cf. Fig. C.1]. Next, we look for the stationary points which obey the conditions,

$$\left.\frac{\partial Q}{\partial \mathcal{X}}\right|_{\mathcal{X}_e, \mathcal{P}_e} = \mathcal{X}_e(\mathcal{X}_e^2 + \mathcal{P}_e^2 - 1) + \beta^{1/2} = 0, \quad (\text{C.5})$$

$$\left.\frac{\partial Q}{\partial \mathcal{P}}\right|_{\mathcal{X}_e, \mathcal{P}_e} = \mathcal{P}_e(\mathcal{X}_e^2 + \mathcal{P}_e^2 - 1) = 0, \quad (\text{C.6})$$

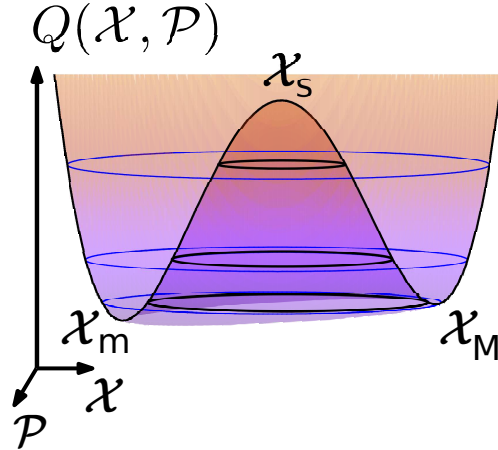


Figure C.1: Quasienergy potential for the driven nonlinear oscillator corresponding to $\nu = 10^{-3}\omega_0$, $f = \nu/10$, and $\delta\omega = -2\nu$. The surface is divided into an internal and an external dome.

corresponding to $\mathcal{P}_e = 0$ and $\mathcal{X}_e^3 - \mathcal{X}_e + \beta^{1/2} = 0$. For $0 < \beta < 4/27$, this equation has three solutions associated to a minimum ($e = m$), a maximum ($e = M$), and a saddle point ($e = s$). They are given by $\mathcal{X}_m = -\cos\theta/\sqrt{3} - \sin\theta$, $\mathcal{X}_M = -\cos\theta/\sqrt{3} + \sin\theta$ and $\mathcal{X}_s = 2\cos\theta/\sqrt{3}$ with $\theta = (\pi - \arctan\sqrt{4/27\beta - 1}/3)$. In this interval, $0 < \beta < 4/27$, the Hamiltonian is bistable, i.e., in a certain range of quasienergies there are two trajectories corresponding to the same quasienergy, one on the internal part of the surface and the other on the external part. When the motion is quantized, the quasiclassical trajectories are associated to quantum levels. In order to compute the energies, and the squeezing factors of the solutions close to the extremal points ($e = m, M$), we apply a harmonic expansion of the quasienergy surface around these points as

$$Q(\tilde{\mathcal{X}} + \mathcal{X}_{m/M}, \mathcal{P}) \simeq Q(\mathcal{X}_{m/M}, 0) \pm \frac{1}{2}m_{m/M}\omega_e^2\tilde{\mathcal{X}}^2 \pm \frac{1}{2m_{m/M}}\mathcal{P}^2, \quad (\text{C.7})$$

with $\tilde{\mathcal{X}} = \mathcal{X} - \mathcal{X}_{m/M}$. The frequency $\omega_{m/M}$ and the mass term $m_{m/M}$ are related to curvature of the surface, $\partial^2 Q/\partial \mathcal{P}^2 = m_{m/M}\omega_{m/M}^2$ and $|\partial^2 Q/\partial \mathcal{X}^2| = 1/m_{m/M}$. Thereby, $\omega_{m/M} = \sqrt{3\mathcal{X}_e^4 - 4\mathcal{X}_{m/M}^2 + 1}$ and $m_{m/M} = 1/|\mathcal{X}_{m/M}^2 - 1|$. The corresponding energies are

$$E_{m/M} = \frac{2\delta\omega^2}{\nu} \left(Q(\mathcal{X}_{m/M}, 0) \pm \frac{\lambda}{2}\omega_{m/M} \right) + \frac{\delta\omega}{2} - \frac{\nu}{8}. \quad (\text{C.8})$$

For the squeezing factor r^* , [2] we use the definition $\exp[2r] = \Delta\mathcal{P}/\Delta\tilde{\mathcal{X}}$. With this

$$r_{m/M}^* = \frac{1}{2} \ln[m_{m/M}\omega_{m/M}] = \frac{1}{4} \ln \frac{3\mathcal{X}_{m/M}^2 - 1}{\mathcal{X}_{m/M}^2 - 1}. \quad (\text{C.9})$$

Thus, the ladder operators a and a^\dagger can be described in terms of the ladder operators b and b^\dagger of the effective auxiliary oscillator (characterized by the mass $m_{m/M}$ and frequency $\omega_{m/M}$) as

$$a = a_{m/M} + b \cosh r_{m/M}^* - b^\dagger \sinh r_{m/M}^* , \quad (\text{C.10})$$

where $a_{m/M} = \mathcal{X}_{m/M}/\sqrt{2\lambda}$ and $b = i(\mathcal{P} - im_{m/M}\omega_{m/M}\tilde{\mathcal{X}})/\sqrt{2\lambda m_{m/M}\omega_{m/M}}$.

Lowest-order expansion in self energies

To facilitate the understanding and to simplify the notation of the rates

$$\chi_2^1 [\gamma_{l/r,k,m}^{(1)}(z)]_{\chi_2'}^{\chi_1'} = \sum_{\chi'} \chi_1^1 [T_k^m(\omega_{\text{ex}})]_{\chi'}^{\chi_1'} \delta_{\chi_2 \chi_2'} \int d\epsilon \frac{f_{l/r}^-(\epsilon)}{i(\epsilon_{\chi'} - \epsilon_{\chi_2}) + i(\epsilon + z - k\omega_{\text{ex}})}, \quad (\text{D.1})$$

$$\chi_2^1 [\gamma_{l/r,k,m}^{(2)}(z)]_{\chi_2'}^{\chi_1'} = \sum_{\chi'} \chi_2^1 [T_k^m(\omega_{\text{ex}})]_{\chi'}^{\chi_1'} \delta_{\chi_1 \chi_1'} \int d\epsilon \frac{f_{l/r}^-(\epsilon)}{i(\epsilon_{\chi_1} - \epsilon_{\chi'}) - i(\epsilon - z + k\omega_{\text{ex}})}, \quad (\text{D.2})$$

$$\chi_2^1 [\gamma_{l/r,k,m}^{(3)}(z)]_{\chi_2'}^{\chi_1'} = \sum_{\chi'} \chi_1^1 [T_k^m(\omega_{\text{ex}})]_{\chi_2'}^{\chi_2'} \delta_{\chi_1 \chi_1'} \int d\epsilon \frac{f_{l/r}^+(\epsilon)}{i(\epsilon_{\chi_1} - \epsilon_{\chi'}) + i(\epsilon + z - k\omega_{\text{ex}})}, \quad (\text{D.3})$$

$$\chi_2^1 [\gamma_{l/r,k,m}^{(4)}(z)]_{\chi_2'}^{\chi_1'} = \sum_{\chi'} \chi_1^1 [T_k^m(\omega_{\text{ex}})]_{\chi_1'}^{\chi_1'} \delta_{\chi_2 \chi_2'} \int d\epsilon \frac{f_{l/r}^+(\epsilon)}{i(\epsilon_{\chi'} - \epsilon_{\chi_2}) - i(\epsilon - z + k\omega_{\text{ex}})}, \quad (\text{D.4})$$

$$\chi_2^1 [\gamma_{l/r,k,m}^{(5)}(z)]_{\chi_2'}^{\chi_1'} = -\chi_2^1 [T_k^m(\omega_{\text{ex}})]_{\chi_1'}^{\chi_2'} \int d\epsilon \frac{f_{l/r}^-(\epsilon)}{i(\epsilon_{\chi_1'} - \epsilon_{\chi_2}) + i(\epsilon + z - k\omega_{\text{ex}})}, \quad (\text{D.5})$$

$$\chi_2^1 [\gamma_{l/r,k,m}^{(6)}(z)]_{\chi_2'}^{\chi_1'} = -\chi_2^1 [T_k^m(\omega_{\text{ex}})]_{\chi_2'}^{\chi_1'} \int d\epsilon \frac{f_{l/r}^+(\epsilon)}{i(\epsilon_{\chi_1'} - \epsilon_{\chi_2}) - i(\epsilon - z + k\omega_{\text{ex}})}, \quad (\text{D.6})$$

$$\chi_2^1 [\gamma_{l/r,k,m}^{(7)}(z)]_{\chi_2'}^{\chi_1'} = -\chi_2^1 [T_k^m(\omega_{\text{ex}})]_{\chi_2'}^{\chi_1'} \int d\epsilon \frac{f_{l/r}^+(\epsilon)}{i(\epsilon_{\chi_1} - \epsilon_{\chi_2'}) + i(\epsilon + z - k\omega_{\text{ex}})}, \quad (\text{D.7})$$

$$\chi_2^1 [\gamma_{l/r,k,m}^{(8)}(z)]_{\chi_2'}^{\chi_1'} = -\chi_2^1 [T_k^m(\omega_{\text{ex}})]_{\chi_1'}^{\chi_2'} \int d\epsilon \frac{f_{l/r}^-(\epsilon)}{i(\epsilon_{\chi_1} - \epsilon_{\chi_2'}) - i(\epsilon - z + k\omega_{\text{ex}})}, \quad (\text{D.8})$$

we introduce diagrams on the Keldysh contour. Each auxiliary rate stems from each term on the right hand side in Eq. (5.17). We refer to the rules in Sec. 5.4.2 to draw the

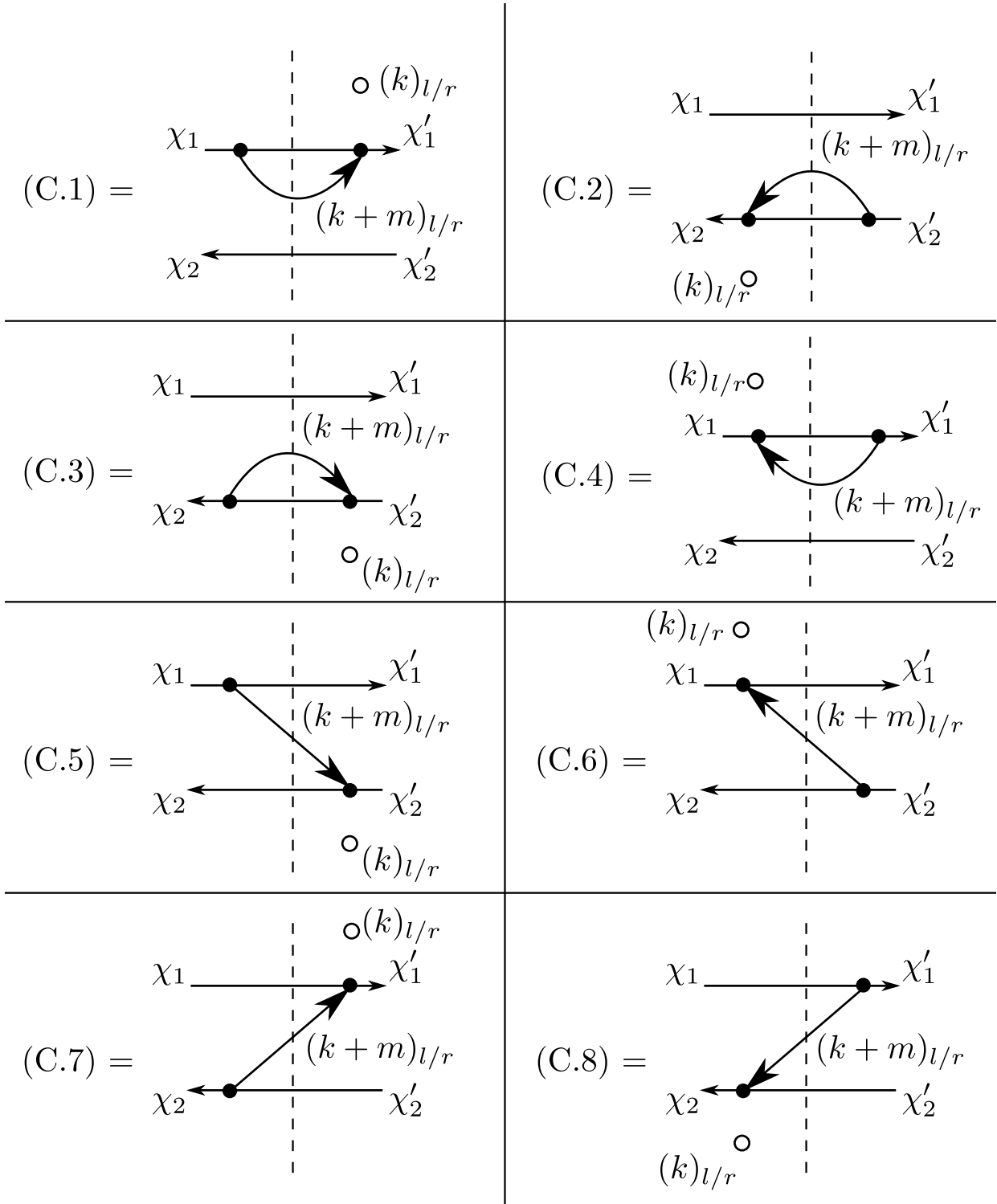


Figure D.1: Feynman for the transition rates in first order in Γ .

corresponding diagrams, see Fig. D.1.

D.1 Explicit calculation of the rates

The calculation of the rates (D.1)–(D.8) in the high frequency approximation involves mainly the calculation of energy integrals of the type

$$\mathcal{I}_{\sigma,l/r}^{\pm}(\epsilon) = \lim_{\eta \rightarrow 0} \int dE \frac{f_{l/r}^{\pm}(E)}{\epsilon - E + i\sigma\eta}, \quad \text{with } \sigma = +, - . \quad (\text{D.9})$$

The above infinite integral denotes an integral over the whole spectrum, i.e., $\int_{-\infty}^{+\infty} dE$. In order to ensure the convergence of the above integral, one can introduce a Lorentzian cut-off weight function $D_{l/r}(E) = E_c^2 / [(E - \mu_{l/r})^2 + E_c^2]$, i.e., $\int dE \rightarrow \int dE D_{l/r}(E)$ where E_c is the cut-off energy.

The integral (D.9) can be solved by means of residues of a contour integration along a path describing a half circle with radius $R \rightarrow \infty$ either in the lower or upper complex plane [cf. Fig. D.2]. To this end, we have to find the poles in the complex plane of the function in the integral (D.9) (including the weight function), i.e., the poles of $f(z) = D_{l/r}(z)f_{l/r}^{\pm}(z)/(\epsilon - z + i\sigma\eta)$, $z \in \mathbb{C}$. The cut-off weight function $D_{l/r}(z)$ contributes with poles at $z_{\pm} = \mu_{l/r} \pm iE_c$, the Fermi function $f_{l/r}^{\pm}(z)$ with poles at $z_m = i\pi(2m+1)/\beta + \mu_{l/r}$, $m \in \mathbb{N}$, and the denominator with the pole $z_0 = \epsilon + i\sigma\eta$. Now, we average over the upper and lower contour, over C_1 and C_2 respectively,

$$\begin{aligned} \mathcal{I}_{\sigma,l/r}^{\pm}(\epsilon) &= \lim_{R \rightarrow \infty} \frac{1}{2} \left(\int_{C_1} f(z) dz + \int_{C_2} f(z) dz \right) \\ &= \pi i \left(\sum_k \text{Re}_{z=z_k} f(z) - \sum_{k'} \text{Re}_{z=z_{k'}} f(z) \right). \end{aligned} \quad (\text{D.10})$$

Above, z_k and $z_{k'}$ are the poles enclosed by the path C_1 and C_2 , respectively. With this, the integral (D.9) reads

$$\begin{aligned} \mathcal{I}_{\sigma,l/r}^{\pm}(\epsilon) &= \pi i D_{l/r}(\epsilon) \left(-\sigma f_{l/r}^{\pm}(\epsilon) + \frac{\epsilon - \mu_{l/r}}{2iE_c} \mp \frac{1}{2} \tanh[i\beta E_c/2] \right) \\ &\mp \pi i D_{l/r}(\epsilon) \beta^{-1} \sum_{m=0}^{\infty} \left(\frac{1}{\epsilon - z_m} - \frac{1}{\epsilon - \mu_{l/r} + z_m} \right) \\ &\mp \pi i D_{l/r}(\epsilon) \beta^{-1} \sum_{m=0}^{\infty} \left(\frac{1}{z_m - \mu_{l/r} - iE_c} - \frac{1}{z_m - \mu_{l/r} + iE_c} \right). \end{aligned} \quad (\text{D.11})$$

For a very large cut-of energy E_c , $D_{l/r}(\epsilon) \sim 1$ and using the property of the digamma functions $\psi(z_1) - \psi(z_2) = \sum_{m=0}^{\infty} [1/(m+z_2) - 1/(m+z_1)]$, the Eq. (D.11) might be written

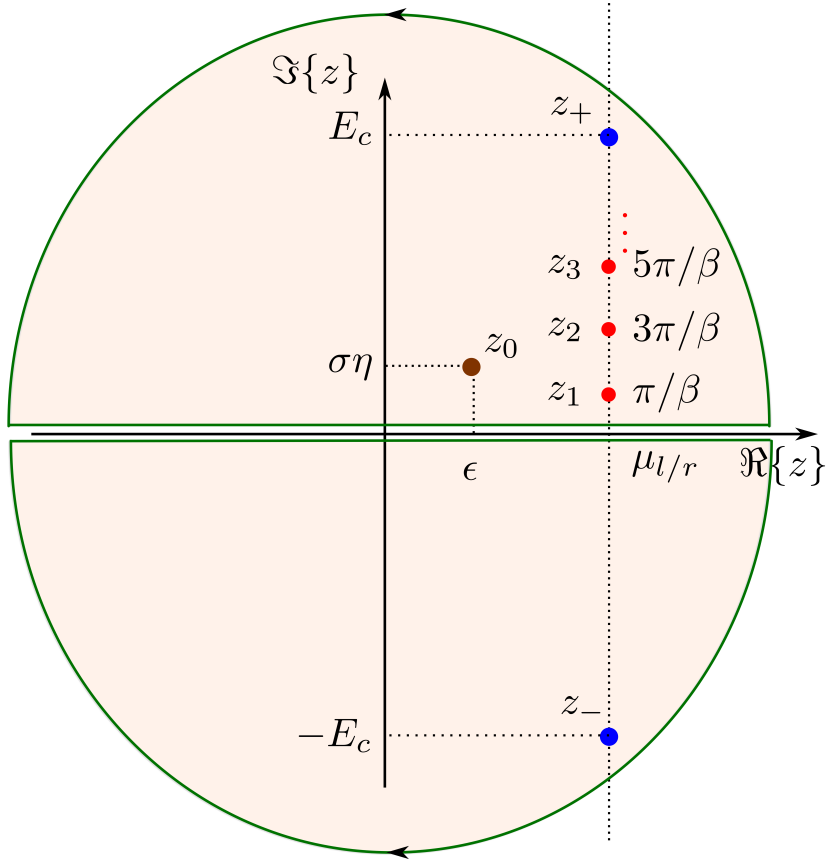


Figure D.2: Integration contour in the complex plane.

as

$$\mathcal{I}_{\sigma, l/r}^{\pm}(\epsilon) \approx -\pi i \sigma f_{l/r}^{\pm}(\epsilon) \mp \frac{1}{2} \left[\psi \left(\frac{1}{2} + \frac{i\beta}{2\pi}(\epsilon - \mu_{l/r}) \right) + \psi \left(\frac{1}{2} - \frac{i\beta}{2\pi}(\epsilon - \mu_{l/r}) \right) \right] \pm \ln \left[\frac{\beta E_c}{2\pi} \right]. \quad (\text{D.12})$$

With this result, the calculation of the rates (D.1)-(D.8) and their numerical implementation is straightforward.

Bibliography

- [1] T. W. Hänsch and H. Walther, *Rev. Mod. Phys.* **71**, S242 (1999).
- [2] G. J. Walls and D. F. Milburn, *Quantum Optics* (Springer, 2008).
- [3] C. E. Wieman, D. E. Pritchard, and D. J. Wineland, *Rev. Mod. Phys.* **71**, S253 (1999).
- [4] D. Leibfried, R. Blatt, C. Monroe, and D. Wineland, *Rev. Mod. Phys.* **75**, 281 (2003).
- [5] M. L. Roukes, *Physics World* **15**, 25 (2001).
- [6] H. G. Craighead, *Foundations of Nanomechanics* (Springer, 2003).
- [7] R. H. Blick and M. Grifoni, *New J. Phys.* **7** (2005).
- [8] M. Aspelmeyer and K. Schwab, *New J. Phys.* **10** (2008).
- [9] Y. Makhlin, G. Schön, and A. Shnirman, *Rev. Mod. Phys.* **73**, 357 (2001).
- [10] Y. Makhlin, G. Schön, and A. Shnirman, *Josephson-junction qubits and the readout process by single-electron transistor* (Nova Science Publishers, 2000).
- [11] M. A. Nielsen and I. L. Chuang, *Quantum computation and quantum information* (Cambridge University Press, 2000).
- [12] C. Gardiner and P. Zoller, *Quantum Noise: A Handbook of Markovian and Non-Markovian Quantum Stochastic Methods with Applications to Quantum Optics* (Springer, 2004).
- [13] A. A. Clerk, M. H. Devoret, S. M. Girvin, F. Marquardt, and R. J. Schoelkopf, *Rev. Mod. Phys.* **82**, 1155 (2010).

-
- [14] M. Campisi, P. Hänggi, and P. Talkner, *Rev. Mod. Phys.* **83**, 771 (2011).
- [15] F. Marquardt, J. P. Chen, A. A. Clerk, and S. M. Girvin, *Phys. Rev. Lett.* **99**, 093902 (2007).
- [16] C. H. Henry and R. F. Kazarinov, *Rev. Mod. Phys.* **68**, 801 (1996).
- [17] R. Vijay, M. H. Devoret, and I. Siddiqi, *Rev. Sci. Instrum.* **80**, 111101 (2009).
- [18] I. Siddiqi, R. Vijay, F. Pierre, C. M. Wilson, M. Metcalfe, C. Rigetti, L. Frunzio, and M. H. Devoret, *Phys. Rev. Lett.* **93**, 207002 (2004).
- [19] I. Siddiqi, R. Vijay, F. Pierre, C. M. Wilson, M. Metcalfe, C. Rigetti, R. J. Schoelkopf, M. H. Devoret, D. Vion, and D. Esteve, *Phys. Rev. Lett.* **94**, 027005 (2005).
- [20] A. Lupascu, S. Saito, T. Picot, P. C. de Groot, C. J. P. M. Harmans, and J. E. Mooij, *Nature Phys.* **3**, 119 (2007).
- [21] I. Siddiqi, R. Vijay, M. Metcalfe, E. Boaknin, L. Frunzio, R. J. Schoelkopf, and M. H. Devoret, *Phys. Rev. B* **73**, 054510 (2010).
- [22] F. R. Ong, M. Boissonneault, F. Mallet, A. Palacios-Laloy, A. Dewes, A. C. Doherty, A. Blais, P. Bertet, D. Vion, and D. Esteve, *Phys. Rev. Lett.* **106**, 167002 (2011).
- [23] M. Metcalfe, E. Boaknin, V. Manucharyan, R. Vijay, I. Siddiqi, C. Rigetti, L. Frunzio, R. J. Schoelkopf, and M. H. Devoret, *Phys. Rev. B* **76**, 174516 (2007).
- [24] F. W. Beil, L. Pescini, E. Höhberger, A. Kraus, A. Erbe, and R. H. Blick, *Nanotechnology* **14**, 799 (2003).
- [25] M. D. LaHaye, O. Buu, B. Camarota, and K. Schwab, *Science* **304**, 74 (2004).
- [26] A. Gaidarzhy, G. Zolfagharkhani, R. L. Badzey, and P. Mohanty, *Phys. Rev. Lett.* **94**, 030402 (2005).
- [27] K. C. Schwab, M. P. Blencowe, M. L. Roukes, A. N. Cleland, S. M. Girvin, G. J. Milburn, and K. L. Ekinci, *Phys. Rev. Lett.* **95**, 248901 (2005).
- [28] U. Weiss, *Quantum Dissipative Systems* (World Scientific, 1993).
- [29] F. Reif, *Fundamentals of Statistical and Thermal Physics* (McGraw Hill, 1965).
- [30] A. Einstein, *Ann. Phys. Berlin* **322**, 549 (1905).

-
- [31] S. Chandrasekhar, *Rev. Mod. Phys.* **15**, 1 (1943).
- [32] V. Magalinskii, *Sov. Phys. JETP* **9**, 1381 (1959).
- [33] I. R. Senitzky, *Phys. Rev.* **119**, 670 (1960).
- [34] I. R. Senitzky, *Phys. Rev.* **124**, 642 (1961).
- [35] G. W. Ford, M. Kac, and P. Mazur, *J. Math. Phys.* **6**, 504 (1965).
- [36] R. Zwanzig, *J. Stat. Phys.* **9**, 215 (1973).
- [37] A. O. Caldeira and A. J. Leggett, *Annals of Physics* **149**, 374 (1983).
- [38] H. Carmichael, *An Open Systems Approach to Quantum Optics* (Springer, 1991).
- [39] R. P. Feynman and F. L. V. Jr, *Annals of Physics* **24**, 118 (1963).
- [40] S. Kholer, T. Dittrich, and P. Hänggi, *Phys. Rev. E* **55**, 300 (1995).
- [41] T. Dittrich, P. Hänggi, G.-L. Ingold, B. Krammer, G. Schön, and W. Zwerger, *Quantum Transport and Dissipation* (Wiley-VCH, 1998).
- [42] J. H. Shirley, *Phys. Rev.* **138**, B979 (1965).
- [43] Y. B. Zeldovitch, *Sov. Phys. JETP* **24**, 1006 (1967).
- [44] V. I. Ritus, *Sov. Phys. JETP* **24**, 1041 (1967).
- [45] H. Sambe, *Phys. Rev. A* **7**, 2203 (1973).
- [46] S. Kohler, T. Dittrich, and P. Hänggi, *Phys. Rev. E* **55**, 300 (1997).
- [47] V. Peano and M. Thorwart, *New J. Phys.* **8**, 21 (2006).
- [48] V. Peano and M. Thorwart, *Chem. Phys.* **322**, 135 (2006).
- [49] H.-J. Briegel and B.-G. Englert, *Phys. Rev. A* **47**, 3311 (1993).
- [50] M. Lax, *Rev. Mod. Phys.* **32**, 25 (1960).
- [51] M. Lax, *Rev. Phys.* **129**, 2342 (1963).
- [52] M. Watanabe, K. Inomata, T. Yamamoto, and J.-S. Tsai, *Phys. Rev. B* **80**, 174502 (2009).

-
- [53] F. Mallet, F. R. Ong, A. Palacios-Laloy, F. Nguyen, P. Bertet, D. Vion, and D. Esteve, *Nature Phys.* **5**, 791 (2009).
- [54] C. M. Wilson, T. Duty, M. S. F. Person, V. Shumeiko, and P. Delsing, *Phys. Rev. Lett.* **105**, 233907 (2009).
- [55] J. D. Teufel, M. S. Allman, K. Cicak, A. J. Sirois, J. D. Whittaker, and R. W. Simmonds, *Nature* **471**, 204 (2011).
- [56] R. Riviere, S. Deleglise, S. Weis, E. Gavartin, O. Arcizet, A. Schliesser, and T. J. Kippenberg, *Phys. Rev. A* **83**, 063835 (2011).
- [57] A. H. Safavi-Naeini, J. Chan, J. T. Hill, T. P. M. Alegre, A. Krause, and O. Painter, *Phys. Rev. Lett.* **108**, 033602 (2012).
- [58] M. Poot, S. Etaki, I. Mahbood, K. Onomitsu, H. Yamaguchi, Y. M. Blanter, and H. S. J. Zant, *Phys. Rev. Lett.* **105**, 207203 (2011).
- [59] M. Poot and H. S. J. Zant, *Phys. Rep.* **511**, 273 (2012).
- [60] V. Peano and M. Thorwart, *Phys. Rev. B* **82**, 155129 (2010).
- [61] V. Peano and M. Thorwart, *Europhys. Lett.* **89**, 17008 (2010).
- [62] M. I. Dykman, M. Marthaler, and V. Peano, *Phys. Rev. A* **83**, 052115 (2011).
- [63] M. I. Dykman and V. N. Smelyansky, *Sov. Phys. JETP* **67**, 1769 (1988).
- [64] I. Serban, M. I. Dykman, and F. K. Wilhelm, *Phys. Rev. A* **81**, 022305 (2010).
- [65] P. D. Drummond and D. F. Walls, *J. Phys. A* **13**, 725 (1980).
- [66] P. D. Drummond and D. F. Walls, *Phys. Rev. A* **23**, 2563 (1981).
- [67] M. I. Dykman, *Fluctuating Nonlinear Oscillators. From nanomechanics to quantum superconducting circuits* (Oxford University Press, 2012).
- [68] S. André, L. Guo, V. Peano, M. Marthaler, and G. Schön, *Phys. Rev. A* **85**, 053825 (2012).
- [69] V. Leyton, M. Thorwart, and V. Peano, *Phys. Rev. B*, 134501(2011).
- [70] V. Leyton, V. Peano, and M. Thorwart, *New J. Phys.* **14**, 093024 (2012).
- [71] V. Peano and M. Thorwart, *Phys. Rev. B* **70**, 235401 (2004).

-
- [72] L. S. Bishop, J. M. Chow, J. Koch, A. A. Houck, M. H. Devoret, E. Thuneberg, S. M. Girvin, and R. J. Schoelkopf, *Nature* **5**, 105 (2009).
- [73] M. I. Dykman, R. Mannella, P. V. E. McClintock, F. Moss, and S. M. Soskin, *Phys. Rev. A* **37**, 1303 (1988).
- [74] A. P. Dmitriev and M. I. D'yakonov, *Sov. Phys. JETP* **63**, 838 (1986).
- [75] M. I. Dykman and M. V. Fistul, *Phys. Rev. B* **71**, 140508 (2005).
- [76] A. Lupaşcu, C. J. M. Verwijs, R. N. Schouten, C. J. P. M. Harmans, and J. E. Mooij, *Phys. Rev. Lett.* **93**, 177006 (2004).
- [77] A. Lupaşcu, C. J. P. M. Harmans, and J. E. Mooij, *Phys. Rev. B* **71**, 184506 (2005).
- [78] A. H. Nayfeh and D. T. Mook, *Nonlinear Oscillations* (Wiley, 1979).
- [79] A. Lupaşcu, E. F. C. Driessen, L. Roschier, C. J. P. M. Harmans, and J. E. Mooij, *Phys. Rev. Lett.* **96**, 127003 (28 Mar. 2006).
- [80] M. I. Dykman and M. A. Krivoglaz, *Sov. Phys. JETP* **50**, 30 (1979).
- [81] M. I. Dykman and V. N. Smelyansky, *Phys. Rev. A* **41**, 3090 (1990).
- [82] K. W. Murch, R. Vijay, I. Barth, O. Naaman, J. Aumentado, L. Friedland, and I. Siddiqi, *Nature Phys.* **7**, 105 (2010).
- [83] O. Naaman, J. Aumentado, L. Friedland, J. S. Wurtele, and I. Siddiqi, *Phys. Rev. Lett.* **101**, 117005 (2008).
- [84] J. E. Mooij, T. P. Orlando, L. Levitov, L. Tian, and C. H. van der Wal, *Science* **285**, 1036 (1999).
- [85] O. H. Soerensen, *J. Appl. Phys.* **47**, 5030 (1976).
- [86] C. D. Tesche and J. Clarke, *J. Low Temp. Phys.* **29**, 301 (1977).
- [87] P. Bertet, I. Chiorescu, G. Burkard, K. Semba, C. J. P. M. Harmans, D. P. DiVincenzo, and J. E. Mooij, *Phys. Rev. Lett.* **25**, 257002 (2005).
- [88] M. Thorwart, E. Paladino, and M. Grifoni, *Chem. Phys.* **296**, 333 (2004).
- [89] K. Flensberg and H. Bruus, *Many-Body Quantum Theory in Condensed Matter Physics* (Oxford University Press, 2004).

-
- [90] W. G. van der Wiel, S. De Franceschi, J. M. Elzerman, T. Fujisawa, S. Tarucha, and L. P. Kouwenhoven, *Rev. Mod. Phys.* **75**, 1 (2002).
- [91] J. Lu, P. S. E. Yeo, C. K. Gan, P. Wu, and K. P. Loh, *Nature Nanotech.* **6**, 247 (2011).
- [92] D. R. Strachan, D. E. Smith, D. E. Johnston, T.-H. Park, M. J. Therien, D. A. Bonnell, and A. T. Johnson, *App. Phys. Lett.* **86**, 043109 (2005).
- [93] S. J. Tans, M. H. Devoret, H. Dai, A. Thess, R. E. Smalley, L. J. Geerligs, and C. Dekker, *Nature* **386**, 474 (1997).
- [94] J. W. G. Wilder, L. C. Venema, A. G. Rinzler, R. E. Smalley, and C. Dekker, *Nature* **391**, 59 (1998).
- [95] N. Y. Kim, *Handbook of Nanophysics: Nanotubes and Nanowires* (CRC Press, 2011).
- [96] R. Shekhter, L. Gorelik, L. I. Glazman, and M. Jonson, *Phys. Rev. Lett.* **97**, 156801 (2006).
- [97] C. A. Regal, J. D. Teufel, and K. W. Lehnert, *Nature Phys.* **4**, 555 (2008).
- [98] A.-P. Jauho, N. S. Wingreen, and Y. Meir, *Phys. Rev. B* **50**, 5528 (1994).
- [99] J. König, J. Schmid, H. Schoeller, and G. Schön, *Phys. Rev. B* **54**, 16820 (1996).
- [100] J. König, H. Schoeller, and G. Schön, *Phys. Rev. Lett.* **76**, 1715 (1996).
- [101] S. Kohler, J. Lehmann, and P. Hänggi, *Phys. Rep.* **406**, 379 (2005).
- [102] P. K. Tien and J. R. Gordon, *Phys. Rev.* **129**, 647 (1963).
- [103] L. P. Kouwenhoven, C. M. Marcus, P. L. Mceuen, S. Tarucha, R. M. Westervelt, and N. S. Wingreen, *Mesoscopic electron transport: Electron transport in quantum dots* (Springer, 1997).
- [104] L. P. Kouwenhoven, S. Jauhar, K. McCormick, D. Dixon, P. L. McEuen, Y. V. Nazarov, N. C. van der Vaart, and C. T. Foxon, *Phys. Rev. B* **50**, 2019 (1994).
- [105] R. Landauer, *IBM J. Res. Dev.* **1**, 233 (1957).
- [106] M. Büttiker, *Phys. Rev. Lett.* **57**, 1761 (1986).
- [107] M. Büttiker, *Phys. Rev. B* **46**, 12485 (1992).

-
- [108] C. Caroli, R. Combescot, P. Nozières, and D. Saint-James, *J. Phys. C* **4**, 916 (1971).
- [109] C. Caroli, R. Combescot, P. Nozières, and D. Saint-James, *J. Phys. C* **5**, 21 (1972).
- [110] N. S. Wingreen, A. P. Jauho, and Y. Meir, *Phys. Rev. B* **48**, 8487 (1993).
- [111] C. Stafford, *Phys. Rev. Lett.* **77**, 2770 (1996).
- [112] Y. Meir, N. S. Wingreen, and P. Lee, *Phys. Rev. Lett.* **66**, 3048 (1991).
- [113] C. Bruder and H. Schoeller, *Phys. Rev. Lett.* **72**, 1076 (1994).
- [114] A. N. Cleland and M. L. Roukes, *Appl. Phys. Lett.* **69**, 2653 (1996).
- [115] A. N. Cleland and M. L. Roukes, *Nature* **392**, 161 (1998).
- [116] C. T.-C. Nguyen, A.-C. Wong, and H. Ding, *Dig. Tech. Pap.-IEEE Int. Solid-State Circuits Conf.* **448**, 78 (1999).
- [117] H. Krömmner, A. Erbe, A. Tilke, S. Manus, and R. H. Blick, *Europhys. Lett.* **50**, 101 (2000).
- [118] A. Erbe, H. Krömmner, A. Kraus, R. H. Blick, G. Corso, and K. Richter, *Europhys. Lett.* **77**, 3102 (2000).
- [119] A. N. Cleland, M. Pophristic, and I. Ferguson, *Appl. Phys. Lett.* **79**, 2070 (2001).
- [120] X. M. H. Huang, C. A. Zorman, M. Mehregany, and M. Roukes, *Nature* **421**, 496 (2003).
- [121] R. G. Knobel and A. N. Cleland, *Nature* **2003**, 291 (424).
- [122] A. Husain, J. Hone, H. W. C. Postma, X. M. H. Huang, T. Drake, M. Barbic, A. Scherer, and M. L. Roukes, *Appl. Phys. Lett.* **83**, 1240 (2003).
- [123] B. Babic, J. Furer, S. Sahoo, S. Farhangfar, and C. Schönenberger, *Nano Lett.* **3**, 1577 (2003).
- [124] C. Li and T.-W. Chou, *Appl. Phys. Lett.* **84**, 121 (2004).
- [125] X. Wang, K. A. G. Y. Chen, S. Erramilli, and P. Mohanty, *Appl. Phys. Lett.* **92**, 013903 (2008).
- [126] J. Dornignac, A. Kalinowski, S. Erramilli, and P. Mohanty, *Phys. Rev. Lett.* **96**, 186105 (2006).

- [127] Y. Chen, X. Wang, M. K. Hong, S. Erramilli, P. Mohanty, and C. Rosenberg, *Appl. Phys. Lett.* **91**, 243511 (2007).
- [128] R. L. Badzey and P. Mohanty, *Nature* **437**, 995 (2005).
- [129] P. Mohanty, G. Zolfagharkhani, S. Kettemann, and P. Fulde, *Phys. Rev. B* **70**, 195301 (2004).
- [130] S. M. Carr, W. E. Lawrence, and M. N. Wybourne, *Phys. Rev. B* **64**, 220101 (2001).
- [131] S. M. Carr, W. E. Lawrence, and M. N. Wybourne, *Physica B* **316**, 464 (2002).
- [132] P. Werner and W. Zwerger, *Europhys. Lett.* **65**, 158 (2004).
- [133] E. Buks and M. L. Roukes, *Europhys. Lett.* **54**, 220 (2001).
- [134] J. S. Aldridge and A. N. Cleland, *Phys. Rev. Lett.* **94**, 156403 (2005).
- [135] T. Ono and M. Esashi, *Appl. Phys. Lett.* **87**, 044105 (2005).
- [136] A. Nitzan, *Annu. Rev. Phys. Chem.* **52**, 681 (2001).
- [137] A. Nitzan and M. Ratner, *Science* **300**, 1384 (2003).
- [138] *Lecture Notes in Physics: Introducing Molecular Electronics*, edited by G. Cuniberti, G. Fagas, and K. Richter (Springer, 2005).
- [139] M. Galperin, M. Ratner, and A. Nitzan, *J. Phys. Cond. Matt.* **19**, 103201 (2007).
- [140] V. May and O. Kühn, *Charge and Energy Transfer Dynamics in Molecular Systems* (Wiley-VCH, 2004).
- [141] M. Cizek, M. Thoss, and W. Domcke, *Phys. Rev. B* **70**, 125406 (2004).
- [142] K. Flensberg, *Phys. Rev. B* **68**, 205323 (2003).
- [143] S. Braig and K. Flensberg, *Phys. Rev. B* **68**, 205324 (2003).
- [144] S. Braig and K. Flensberg, *Phys. Rev. B* **70**, 085317 (2004).
- [145] T. Novotny, A. Rossini, and K. Flensberg, *Phys. Rev. B* **72**, 224502 (2005).
- [146] J. Koch, M. Semmelhack, F. von Oppen, and A. Nitzan, *Phys. Rev. B* **73**, 155306 (2006).
- [147] A. Mitra, I. Aleiner, and A. Millis, *Phys. Rev. Lett.* **94**, 076404 (2005).

-
- [148] R. Egger and A. Gogolin, Phys. Rev. B **77**, 113405 (2007).
- [149] L. Dell'Anna, A. Zazunov, R. Egger, and T. Martin, Phys. Rev. B **75**, 085305 (2007).
- [150] A. A. Kiselev and G. J. Iafrate, Phys. Rev. B **77**, 205436 (2008).
- [151] L. D. Landau and E. M. Lifshitz, *Theory of elasticity* (Pergamon Press, 1973).
- [152] G. Rastelli, M. Houzet, L. Glazman, and F. Pistolesi, C. R. Physique **13**, 410 (2012).
- [153] S. Sapmaz, Y. M. Blanter, L. Gurevich, and H. S. J. van der Zant, Phys. Rev. B **67**, 235414 (2003).
- [154] K. Flensberg, New J. Phys. **8**, 5 (2006).
- [155] L. I. Glazman and R. I. Shekhter, Sov. Phys. JETP **67**, 163 (1988).
- [156] N. S. Wingreen, K. W. Jacobsen, and J. W. Wilkins, Phys. Rev. B **40**, 11834 (1989).
- [157] A. Mitra, I. Aleiner, and A. J. Millis, Phys. Rev. B **69**, 245302 (2004).
- [158] J. Koch and F. von Oppen, Phys. Rev. Lett. **94**, 206804 (2005).
- [159] J. Koch, F. von Oppen, and A. V. Andreev, Phys. Rev. B **74**, 205438 (2006).
- [160] A. Zazunov and T. Martin, Phys. Rev. B **76**, 033417 (2007).
- [161] L. Mühlbacher and E. Rabani, Phys. Rev. Lett. **100**, 176403 (2008).
- [162] J. Koch, F. von Oppen, Y. Oreg, and E. Sela, Phys. Rev. B **70**, 195107 (2004).
- [163] *Handbook of Mathematical Functions*, edited by M. Abramowitz and I. A. Stegun (Dover, 1965).
- [164] L. Mandel and E. Wolf, Rev. Mod. Phys. **37**, 231 (1965).
- [165] H. M. Nussenzveig, *Introduction to Quantum Optics* (Gordon and Breach, 1974).
- [166] R. Hanbury-Brown and R. W. Twiss, Nature **177**, 27 (1956).
- [167] R. J. Glauber, Phys. Rev. **130**, 2529 (1963).
- [168] L. Mandel, Phys. Scr. T **12**, 34 (1986).
- [169] X. T. Zou and L. Mandel, Phys. Rev. A **41**, 475 (1990).
- [170] L. Davidovich, Rev. Mod. Phys. **68**, 127 (1996).

Acknowledgements

No one ever achieved much without the contribution of others, and making my doctorate studies was not the exception. From the time I arrived in the group of Prof. Thorwart, through the process of this Ph D, and finally during the process of writing this Thesis, I have been fortunate with the encouragement and assistance of wonderful and talented people, from the professional and personal side.

I owe a special debt of gratitude to my supervisor Prof. Michael Thorwart, in first place for giving me the great opportunity of working in his group, living in a beautiful and fancy city as Hamburg, and to take part in the open and multicultural German society.

The learning process during the last years would have been more difficult and even unmanageable, without the discussions, not only on academic topics, I held with my fellows Peter, Vittorio, Stephan, and Jochen. I am sincerely grateful for their patience and readiness. A special acknowledgement, also, for careful proofreading and helpful suggestions to improve this manuscript.

On the personal side, I am indebted to my family & friends for their constant support from far away. Especially to my wife, for her penelopesque patience.

Last but not least important, I wish to thank the DAAD for financial support of my position and for providing full assistance during my stay in Germany.

Curriculum Vitae

Vicente Ancelmo Leyton Ortega

Personal Details

Date of birth: August 20, 1984 in Cali Colombia

Education

Universität Hamburg (June 2010 to present)

Ph.D. Student

First part (April 2009 – June 2010) at the **Albert-Ludwigs-Universität**, Freiburg

Universidad del Valle, Cali Colombia

M.Sc. Physics (April 2009)

B.S. Physics (April 2007)

Internship

Henrich-Heine-Universität Düsseldorf (March to September 2008)

Meetings and conferences

- DPG Spring Meeting of the Condensed Matter Section (SKM), Berlin Germany, March 25-30 (2012).
- Nanooptomechanical systems approaching the quantum regime, Trieste Italy, September 6-10 (2010).
- DPG Spring Meeting of the Condensed Matter Section (SKM), Regensburg Germany, March 21–26 (2010).
- Quantum Efficiency: From Biology to Material Science, Black Forest Focus 2, Titisee Germany, October 22–24 (2009).

List of Publications

- V. Leyton, V. Peano, and M. Thorwart, *Quantum noise properties of multiphoton transitions in driven nonlinear resonators*, New J. Phys. **14**, 093024 (2012).
- V. Leyton, M. Thorwart, and V. Peano, *Qubit state detection using the quantum Duffing oscillator*, Phys. Rev. B **84**, 134501 (2011).
- Manuscript in preparation: V. Leyton, S. Weiss, and M. Thorwart, *Signatures of nonlinearity in driven nanomechanical quantum transport*.

Erklärung

Die hier vorgelegte Dissertation habe ich eigenständig und ohne unerlaubte Hilfe angefertigt. Die Dissertation wurde in der vorgelegten oder in ähnlicher Form noch bei keiner anderen Institution eingereicht. Ich habe bisher keine erfolglosen Promotionversuche unternommen.

Vicente Ancelmo Leyton Ortega
Hamburg, den 21.11.2012